ABSTRACT

Design, Analysis and Simulation of a New Current Controller
for Wind Power Generation System using Proportional plus Resonance Control

Bochuan Liu, M.S.E.C.E

Advisor: Byeong-Mun (Ben) Song, Ph.D.

This thesis presents design, analysis and simulation of a new current control scheme for wind power generation system (WPGS). Proportional plus resonance (PR) controller is proposed to improve the accuracy of the control loop. Adding a current sensor at the capacitor filter instead of the damping resistor, the proposed two-current loop controller overcomes the instability of the system caused by the LCL filter and minimizes the power loss on the damping resistor (usually 0.8% of rated power). When the impedance of the grid is changing, the proposed current controller still keeps system stable with phase margins more than 45 degree. Moreover, using the proposed current controller, voltage transient characteristics of WPGS are analyzed and a control scheme is introduced to meet the low-voltage ride-through standard. All analysis and evaluation have been conducted for a 250kW WPGS with 208V grid voltage.

Design, Analysis and Simulation of a New Current Controller for Wind Power Generation System using Proportional plus Resonance Control

by

Bochuan Liu, B.S.

A Thesis

Approved by the Department of Electrical and Computer Engineering

_____
Kwang Y. Lee, Ph. D., Chairperson

Submitted to the Graduate Faculty of
Baylor University in Partial Fulfillment of the
Requirements for the Degree
of
Master of Science in Electrical and Computer Engineering

Approved by the Thesis Committee

_____
Byeong-Mun (Ben) Song, Ph. D., Chairperson

_____
Kwang Y. Lee, Ph. D.

_____
Paul Grabow, Ph.D.

Accepted by the Graduate School
August 2011

_____
J. Larry Lyon, Ph.D., Dean

Page bearing signatures is kept on file in the Graduate School.

TABLE OF CONTENTS

LIST OF FIGURES

ACRONYMS

WPGS – Wind Power Generation System

MPPT – Maximum Power Point Tracking

SPWM – Sine Pulse Width Modulation

PR – Proportional Resonance

PI – Proportional Integral

GM – Gain Margin

PM – Phase Margin

LVRT – Low Voltage Ride Through

ACKNOWLEDGMENTS

I would like to thank Dr. Ben Song for introducing me to the research area of wind power and for his patient guidance and encouragement throughout my thesis work. I would also like to thank Dr. Kwang Y. Lee for reviewing my thesis and giving valuable advice. I would also like to thank Dr. Paul Grabow for reviewing my thesis and giving valuable advice.

I would like to thank Dr. Mike Thompson for helping me complete my Master's program at Baylor University. And I would also like to thank Baylor University School of Engineering and Computer Science for giving me an opportunity to study.

Finally, I would like to thank my parents and friends for their support and help.

CHAPTER ONE

Introduction

Energy is the foundation of the development of the human society. In the past 200 years, the energy based on coal, petroleum, natural gas has improved the development of human society significantly. But as a result, the pollution issue of the environment has become more and more critical. With the increasing demand of energy globally, more attention is being paid to renewable source energy generation such as wind power, solar power, tidal power and so on, among them wind power is the most promising renewable power source [1-4].

There are all kinds of wind power systems, some of which are connected to power system grid and some independent of the power grid. Many wind power sources are installed in isolated islands and remote villages. However, since these wind power systems are highly dependent on the wind, it is necessary to link them with the power grid so that they can be used in continuously providing electric power to customers.

Early wind power plant was connected to distribution networks, but, in recent years, more and larger wind farms have been connected to transmission networks. Every network level has specific requirements when it is connected to wind power generation system. The connection issues for the network are related to utility stability. Grid operators develop rules for connecting generators. Their grid codes have been complemented by specific codes for wind power plants, and the wind turbine manufacturers have responded to these requirements by design measures, mainly in the

area of wind turbine control and electrical system design. During the last few years, there has been a special interest on the grid integration of wind turbines. This has lead to a re-definitions of the grid connection conditions by the system operator (SO) in different countries. The aim of the requirements is to ensure that wind farms do not adversely affect the power system operation with respect to security of supply, reliability and power quality. Essential grid code requirements are related to frequency, voltage and wind turbine behavior in case of grid faults. The most common requirements are as follows [5-7]:

(1) Active power control: Active control of the wind farm output power in order to participate in the energy dispatch as conventional power plants and to prevent overloading of lines.

(2) Frequency control: Wind turbines participate in the frequency control as conventional power plants; the frequency is kept within acceptable limits to ensure the security of supply, prevent the overloading of electric equipment and fulfill the power quality standards.

(3) Voltage control: Wind turbines perform the voltage control as conventional power plants; this is performed by controlling the reactive power.

(4) Fault ride-through capability: Wind Turbines remain connected and, in some cases, to support the power system by injecting sufficient reactive power in order to ensure the system stability.

Power quality is a concept used to characterize an essential set of parameters that determine the impact of wind turbines on the voltage quality of an electric power network. It applies in principle both to transmission and distribution networks, but is far more

essential for the medium voltage networks. The relevant parameters are active and reactive power, including maximum value, voltage fluctuations, number of switching operations (and resulting voltage variations), harmonic currents and related quantities [8-10].

A particular concern is the ability of generators to remain stable and connected to the grid when voltage faults occur on the transmission network. This is known as fault ride-through capability or low-voltage-ride-through capability. The capability of wind farms to support the grid in case of voltage dips in the system is an area that is still under development [11-13].

With recent improvements in power conversion technologies, the wind power resources can easily be connected to the power grid. In order to effectively transfer the acquired electric power to the grid from wind turbine and to minimize the risk associated with electric power system operation and management, the quality of the wind power system must be maintained by the control of the voltage, frequency, reliability, power factor, etc. In the conventional wind power generation system, the direct-quadrant proportional-integral (PI) [14-17] controller is used to reduce the harmonic distortion. And in recent years, a hybrid fuzzy PI controller for current loop has been introduced to improve the dynamics of the system such as reducing the overshoot and settling time which influence the grid stability.

However, the PI controller exhibits two well known drawbacks: inability of the PI controller to track a sinusoidal reference without steady-state error and poor disturbance rejection capability. This is due to the poor performance of the integral action. In order to eliminate these problems, a proportional plus resonance (PR) controller can be used.

The PR controller is a double integrator that has an infinite gain at a certain frequency (resonance frequency) and almost no attenuation outside this frequency. Therefore, the PR controller can be used as a notch filter to compensate the harmonics in a very selective way.

When connecting the inverter to utility grids, a pure inductor or an LCL filter can be used as the inverter output stage [18-20]. An LCL filter can provide higher high-frequency harmonics attenuation and also allow the inverter to operate in both standalone and grid-connected modes. Main factors that were used in LCL design considerations include reactive power consumption in capacitor and current ripple magnitude, the range of LCL resonant frequency, and the total inductance value of LCL filter. To have a stable system, a damping resistor is usually added in series with the capacitor filter, but this damping resistor will cause additional power loss (about 0.8% of rated power). When the power goes high, the power loss of the damping resistor becomes considerably large. To minimize the power loss, a two current-loop feedback control strategy is proposed. In this strategy, the damping resistor is eliminated but one more capacitor current sensor is needed. Using the capacitor current as an inner loop feedback, the overall current loop controller can achieve a stable system without additional power loss [21].

The purpose of this research is to present the modeling and analysis of a three-phase grid-connected wind energy conversion system using MATLAB, and to use the generator speed control to extract the maximum power from the wind. An inverter control algorithm for effective power control is also proposed and evaluated to make the system stable. The design procedure of the LCL filter for switching frequency ripple minimization will also be discussed and simulated in MATLAB to verify the filter's

usefulness in the system. Based on the overall system, voltage transient analysis is presented and a control scheme is introduced to achieve the low-voltage ride-through.

In the rest of the thesis, Chapter Two will give a general introduction to the wind power generation system. Chapter Three will introduce a new current controller using PR based on the LCL filter. Chapter Four will show the system simulation results using the new current controller, and discuss about the low-voltage ride-through ability. Chapter Five will draw some conclusions.

CHAPTER TWO

Overview of Wind Power Generation System

This chapter is a general introduction to the wind power generation system (WPGS). The basic components and their detailed functions will be introduced and discussed. The wind turbines and synchronous generators extract active power from the wind and a well developed Maximum Power Point Tracking method is used to control the rotor speed. A DC/DC boost converter increases the generator-side voltage to a higher level to interface with the grid. In the rest of the thesis, all the improvements and simulations are based on the configuration introduced in this chapter.

Wind Turbines

Wind turbines produce electricity by using the power of the wind to drive an electrical generator. Wind passes through the blades and produces a turning force. A wind turbine extracts kinetic energy from the swept area of the blades (Fig. 1). The power in the airflow is given by [22]:

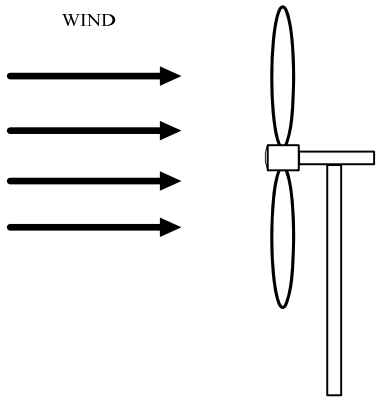

Figure 1: Horizontal axis wind turbine.

$$P_{air} = \frac{1}{2}\rho A v^3 \quad (1)$$

where

ρ = air density (approximately 1.225 kg m^{-3})

A = sweep area of rotor, m^2

v = wind speed, m $s^{-1.}$

Although Eq. (1) gives the power available in the wind, the power transferred to the wind turbine rotor is reduced by the power coefficient, C_p:

$$C_p = \frac{P_{wind-turbine}}{P_{air}} \quad (2)$$

$$P_{wind-turbine} = C_p P_{air} = C_p \times \frac{1}{2}\rho A v^3 \quad (3)$$

A maximum value of C_p is defined by the Betz limit, which states that a turbine can never extract more than 59.3% of the power from an air stream. In reality wind turbine rotors have maximum C_p values in the range of 25-45%. C_p is calculated as [23]:

$$C_p = 0.73\left(\frac{151}{\lambda_1} - 0.58\theta - 0.002\theta^{2.14} - 13.2\right)e^{\frac{-18.4}{\lambda_1}} \quad (4)$$

$$\lambda_1 = 1/\left(\frac{1}{\lambda - 0.02\theta} - \frac{0.003}{\theta^3 + 1}\right) \quad (5)$$

where

θ = pitch angle, degrees

λ = tip speed ratio

It is also conventional to define λ as

$$\lambda = \frac{\omega R}{v} \quad (6)$$

where

ω = rotational speed of the rotor, rad/s

R = radius to tip of rotor, m

v = upwind free wind speed, m s^{-1}

The tip-speed ratio is proportional to the turbine rotor speed and inversely proportional to the wind speed. Fig. 2 shows that the maximum power coefficient is only achieved at a single tip-speed ratio, and for a fixed rotational speed of the wind turbine this only occurs at a single wind speed. Hence, the wind power system can be operated at maximum C_p by adjusting the wind turbine at variable rotational speed [24].

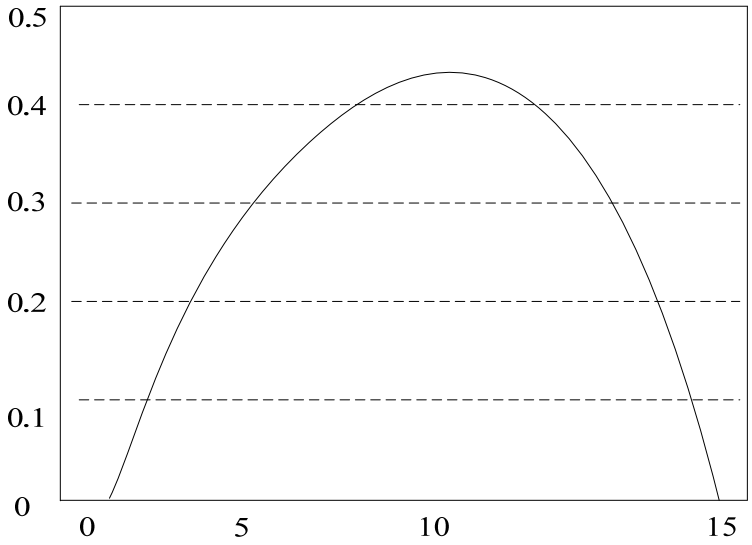

Figure 2: Power coefficient and tip-speed ratio curve.

When the pitch angel and wind speed is fixed, from the analysis above, the relationship between rotational speed of the rotor and output power of the wind turbine can be derived. Fig. 3 is the plot of wind turbine output power curve at different wind speeds (v_1, v_2, v_3 are wind speed and $v_1 < v_2 < v_3$). Points A, B, C are the maximum power output

points at different wind speeds. P_{mopt} is the maximum power curve which is extracted from the variable wind turbine speeds. At different wind speeds, the output power of a wind turbine has a unique maximum point, and the corresponding tip-speed ratio is the optimum tip-speed ratio, and the corresponding wind rotor speed is the optimum rotor speed $\omega_{m.}$ When the wind turbine is operated at the P_{mopt} curve, the corresponding maximum output power is P_{max} which can be calculated as follows [24]:

$$P_{\max} = k\omega_m^{\ 3} \tag{7}$$

$$k = 0.5C_{p\max}\rho A(\frac{R}{\lambda_m})^3 \tag{8}$$

where C_{pmax} is the optimum power coefficient corresponding to P_{mopt} curve and λ_m is the optimum tip-speed ratio corresponding to $C_{pmax.}$

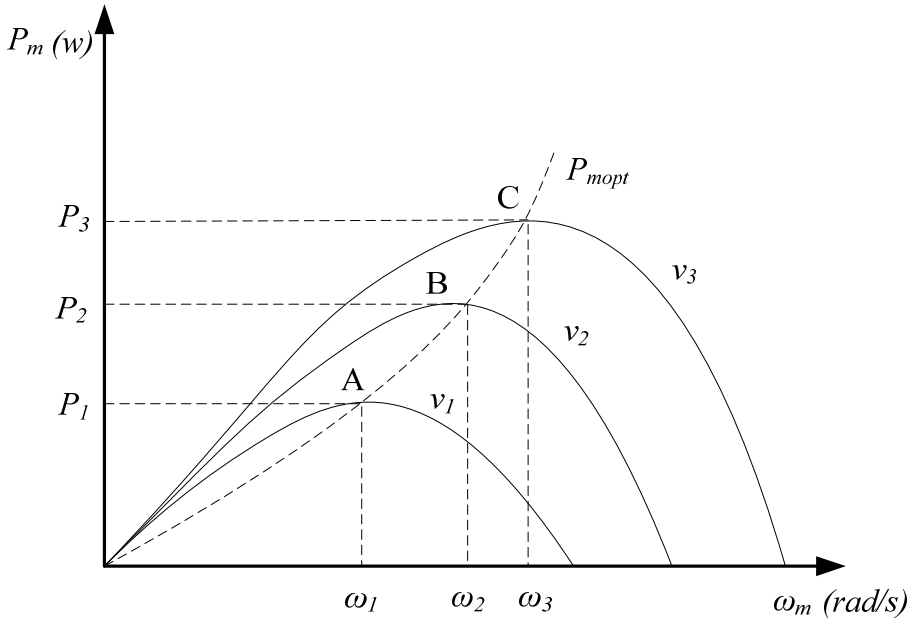

Figure 3: Wind turbine output power curve.

When the pitch angel and wind speed are fixed, and the rotor speed of the wind turbine is running at an optimum speed, the output power of the wind turbine achieves the maximum power. By adjusting the rotor speed of the wind turbine to the optimum speed, the output power of the wind turbine can get its maximum value. However, the speed of the wind is variable and if we want to get the maximum value of C_p, we should control the rotor speed of the wind turbine according to the speed of wind and make the tip-speed ratio to its optimum value.

The power output of a wind turbine at various wind speeds is described by its power curve. The power curve shows the electrical power output as a function of the wind speed and is generally measured using 10 min average data. The power cure is given in Fig. 4. The output power is as follows [24]:

$$P_{wind-turbine} = \begin{cases} \frac{1}{2} C_p \rho \pi R^2 V^3 & V_{in} < V < V_e \\ P_e & V_e < V < V_{out} \\ 0 & V > V_{out} \end{cases} \quad (9)$$

where V_{in} is Cut-in wind speed (the minimum wind speed at which the machine will deliver useful power), V_e is rated wind speed (the speed at which rated power is obtained). V_{out} is cut-out wind speed (the maximum wind speed at which the turbine is allowed to deliver power).

Below the cut-in speed, the wind turbine remains shut down as the speed of the wind is too low for useful energy production. Then, once in operation, the power output increases following a broadly cubic relationship with wind speed until the rated wind speed is reached. Above the rated wind speed the aerodynamic rotor is constructed to limit the mechanical power extracted from the wind, so as to reduce the mechanical loads

on the drive train. Then at very high wind speeds the turbine is shut down. The choice of cut-in and cut-out wind speed is made by the wind turbine designer [25-26].

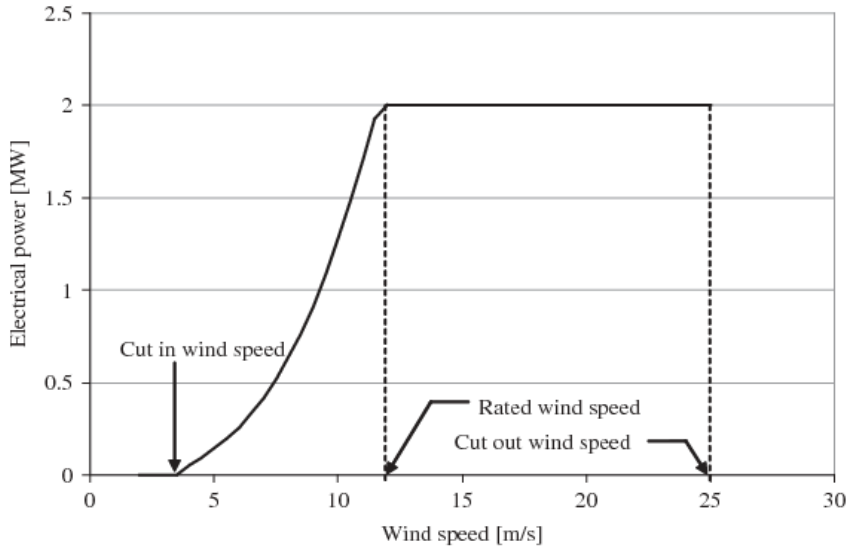

Figure 4: Example of power curve for a 2MW wind turbine.

Maximum Power Point Tracking (MPPT)

For a wind power system, how the rotor speed of a wind turbine is controlled according to a change of the wind speed greatly affects the overall efficiency of the system. For a specific wind turbine, the maximum power curve is recorded in the data sheet of the manufacturer. The maximum power point tracking (MPPT) algorithm used in this paper is shown in Fig. 5.

If the wind speed is ω_1, the system is operating at point *A* and the wind speed changes to v_2; then the system operates at point E and power output is P_1*. The control system uses a look-up table to find that the power output P_1* on P_{mopt} is *F* and the corresponding rotor speed is ω_1*, then the rotor speed command is changed to ω_1*. After the actual rotor speed achieve ω_1*, the system operates at point *G*. Using the same method described above, the rotor speed command will change to *B* after a few iterations.

If the speed changes from v_3 to v_2, the progress is similar. Fig. 6 is the MPPT control system. The input of the speed control system is the power output of the overall system. The speed reference is obtained after MPPT algorithm. The difference between reference speed and actual speed passes through the speed regulator and current regulator, and finally changes the rotor speed.

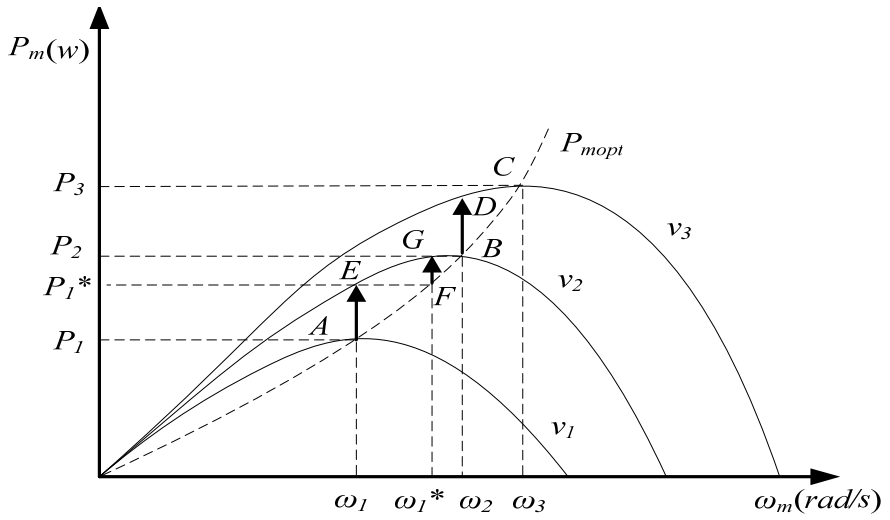

Figure 5: Maximum power point tracking.

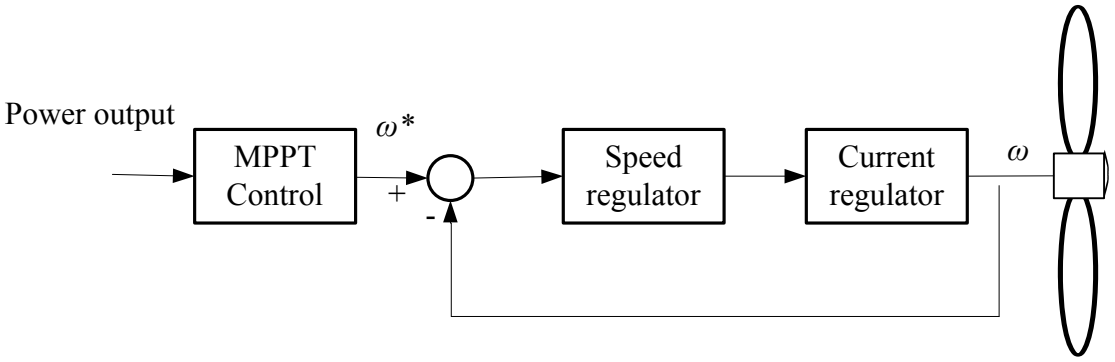

Figure 6: MPPT control system for wind power generation.

This section has mainly introduced the basic elements of a wind turbine and has discussed the relationship between power and the wind. The maximum power curve was

introduced and a maximum power tracking algorithm was explained. In the next section, a more detailed control method for a generator-side converter will be developed.

Overall System Description

The overall topology of the wind power system is shown in Fig. 7. The system consists of a wind turbine and synchronous generator (SG), an AC/DC converter, a DC/DC boost converter, a DC-link, a DC/AC inverter, LCL filter, a transformer and the grid.

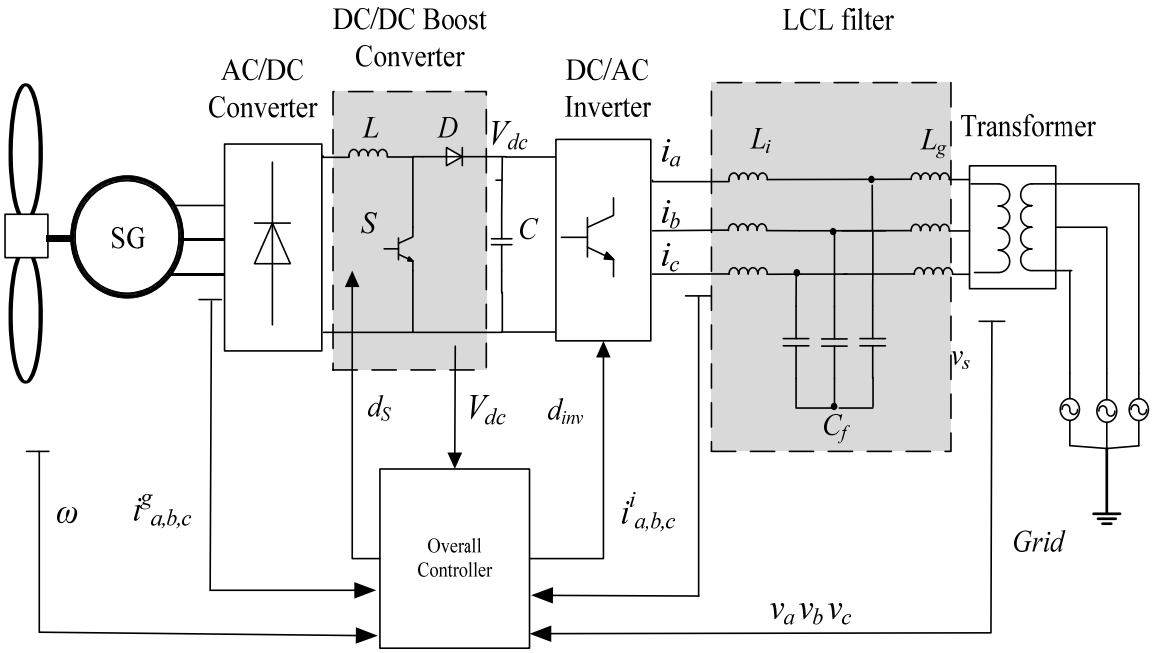

Figure 7: Grid-connected wind power system.

The wind turbine and synchronous generator generate power extracted from the wind and transfer it to the grid side. To fully control the grid current, the DC-link (capacitor C) voltage must be increased to a level higher than the amplitude of the grid

line-line voltage. Since the rated power is usually large, a multiple boost converter topology is used to reduce the rating current of the device and to minimize the current ripple discussed in the next section. The power flow of the grid-side converter is controlled to keep the DC-link voltage constant and control of the generator side is set to track the reference speed.

Sine Pulse Width Modulation (SPWM)

SPWM (Sine Pulse Width Modulation) is typically used to control the voltage source PWM inverter. Fig. 8 shows the three-phase full bridge inverter. The expected output waveform of the SPWM control is sine wave and an isosceles triangle with a much higher frequency than that of the modulation wave is used as the carrier wave. The modulation wave is a sine wave with the same frequency as the expected output wave. The crossing of the modulation wave and carrier wave determines the on and off instances of the switching devices. During the half period of the modulation wave, a series of rectangular waveforms with the same magnitude but different width can be obtained to control the six power switches of the grid-connected Pulse Width Modulation (PWM) inverter. In a sine-triangle three-phase PWM inverter three sinusoidal reference voltage waveforms that are 120 degrees apart are compared to the same triangular carrier wave. Fig. 8 is the waveform of the SPWM. In three-phase inverter circuits, a bipolar control scheme is usually used. The three-phase PWM control uses the same triangle carrier wave and the modulation signals V_a,V_b and V_c, have 120 degree difference. The switching devices of the three-phase signals have the same control pattern. Using phase A as an example, if $V_a > V_{car,}$ then the control produces signals to turn on *S1* and turn off *S4*, and the output voltage of phase A is $V_{an} = V_{dc}/2$ (n is the neutural point of the dc

voltage source). If $V_a < V_{car}$, then the control produces signals to turn on *S4* and turn off *S1*, and $V_{an} = - V_{dc}/2$. Consequently, the signals to turn on the S1 and S4 are complementary. The control method for phases *B* and *C* are similar to phase *A*. From Fig. 9, the waveforms of V_{an}, V_{bn}, V_{cn} have only two voltages $V_{dc}/2$, $-V_{dc}/2$. The waveform of the line to line voltage V_{ab} can be obtained from V_{an}-V_{bn}. If S1 and S4 are turned on, then $V_{ab} = -V_{dc}$, if S3 and S4 are turned on, then $V_{ab} = -V_{dc}$. And if S1 and S3 or S4 and S6 are turned on, then $V_{ab} = 0$. Thus, the output of the line-to-line voltage of the inverter consists of a three-level voltage.

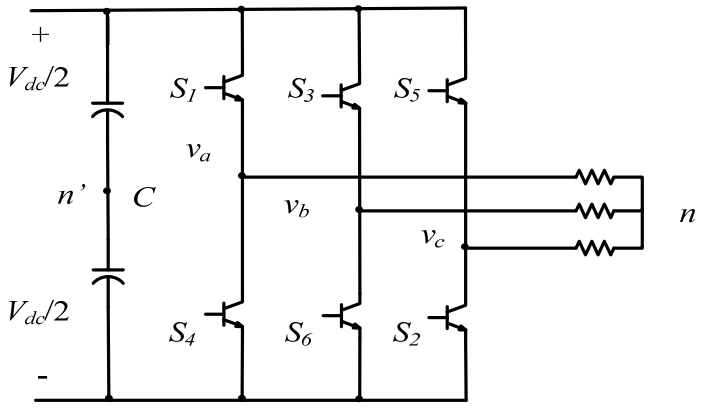

Figure 8: Three-phase inverter.

A modulation index *m* is defined as the amplitude of the modulating waveform/amplitude of the carrier waveform and is related to the fundamental (sine wave) output voltage magnitude. If *m* is high, then the sine wave output is high and vice versa. If $0 < m < 1$, the linear relationship holds: $V_o = mV_{in}$, where V_o and V_{in} are fundamentals of the output voltage and input (DC) voltage, respectively.

The output *rms* fundamental line-to-line voltage of the three-phase SPWM inverter is $\frac{\sqrt{6}}{4} m V_{dc}$, and its amplitude is $\frac{\sqrt{3}}{2} m V_{dc}$.

The harmonics of the output voltage are mainly located *at* $n\omega_{car} \pm k\omega_s$, where ω_{car} is the frequency of the carrier wave and ω_s the frequency of the modulation wave:

$n = 1, 3, 5, \ldots, k = 3(2d-1) \pm 1, d = 1,2,3, \ldots$

$n = 2, 4, 6, \ldots, k = 6d+1, d = 0, 1, 2, \ldots$ *or* $k = 6m-1, m = 1, 2, 3, \ldots$

The high order harmonics of the integral multiple of the carrier wave frequency will not exist. Also, the harmonics of the integral multiple of 3 will not exist in the output line-to-line voltage of the inverter.

Generator-Side Single DC/DC Boost Converter

The generator-side converter extracts the maximum power from the wind using the MPPT curve. For a specific wind turbine, the maximum power curve is given and the reference rotor speed is calculated from that curve and tracked by adjusting the boost converter gate signal. Because the DC voltage of capacitor is kept constant by the grid-side converter, changing the duty ratio of the boost converter can change the AC/DC converter-side voltage and the current flow into the DC/AC inverter, resulting in a change of the rotor speed of the wind turbine so that it follows the maximum power point. The control scheme is shown in Fig. 10, showing the single boost converter control method.

The boost converter consists of a switching device *S*, an inductor *L*, and a diode *D*. Since V_{dc} is constant, the speed is controlled by the DC/DC boost converter. The input voltage V_{dg} and output voltage V_{dc} of the boost converter are related by the following equation:

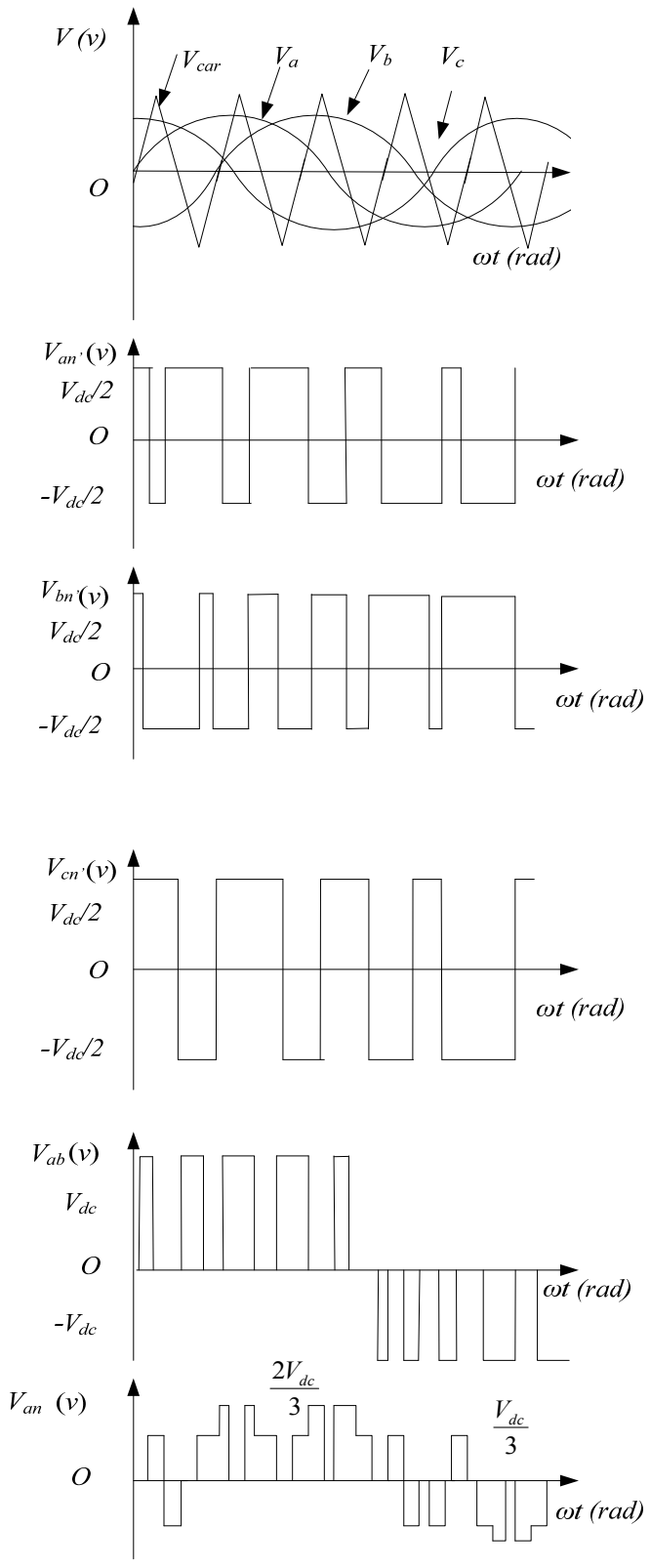

Figure 9: Waveform of the SPWM inverter.

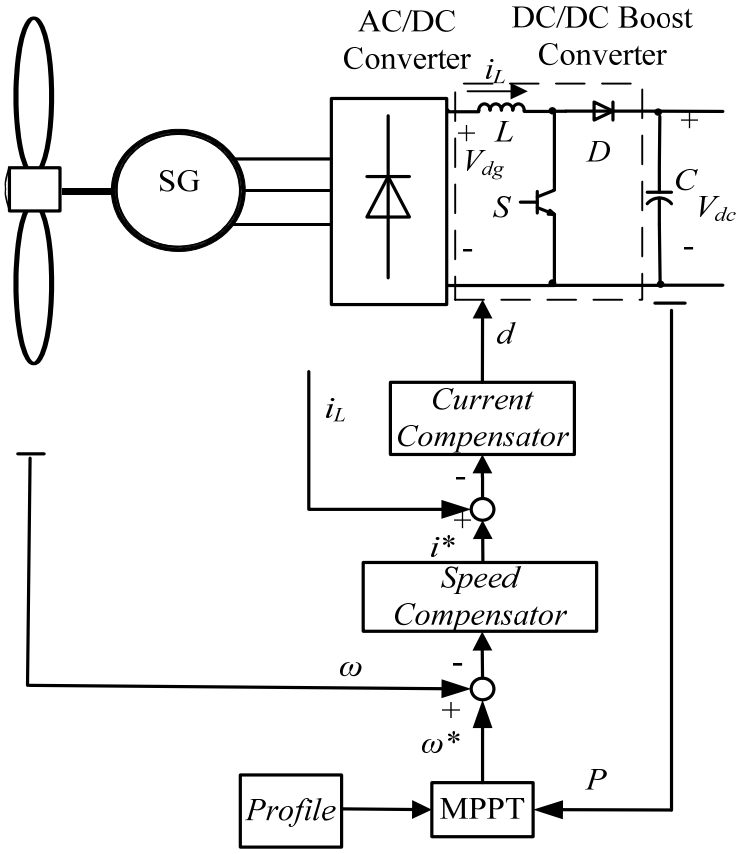

Figure 10: Generator-side block diagram.

$$V_{dc} = \frac{1}{1-d} V_{dg} \tag{9}$$

where d is the duty ratio ($d = T_{on}/T_s$), T_{on} is the time duration when the switching device S is on and T_s is the total switching period. Since V_{dc} is fixed, changing d will change V_{dg} which, finally, changes the rotor speed ω, because the rotor speed ω is a function of the voltage V_{dg} and current i_L. The control system consists of two controllers. One is inner current loop and the other one is outer speed loop. The power output of the system and the power profile are the input of MPPT, which provides the rotor speed reference ω^*. The power which flows into the boost converter equals to the power flows out of the boost converter. When the input current i_L changes, to make a balance of the power

between V_{dg} side and V_{dc} side, the input voltage of the boost converter V_{dg} also changes as well as the duty ratio d. When the voltage V_{dg} changes, the speed ω will also change, and the input current i_L will change to some reference value which can balance the power input and output, and this current reference should be a function of the speed error $\Delta\omega$ and also a function of the actual speed ω. When current i_L changes, the duty ratio d should change to make the balance, and this updated d should be a function of the error of the current Δi_L. A speed compensator is used to produce the current reference and a current compensator is used to produce the desired duty ratio. In this case, PI controller can be used for both compensators to eliminate the steady-state error. The error between the reference ω^* and actual ω becomes the input of the speed PI regulator which provides the current reference i^*. The current reference i^* is compared with actual i_L, and the error passes through the current PI regulator producing the duty ratio d. The detailed speed and current controller design has been discussed in [26]-[27].

Multiple DC/DC Boost Converter

Since the rated power of the overall system is mega watt level, a single DC/DC boost converter must work at a high instant voltage and current. But, it is difficult and expensive to select a device which has such a capability. To overcome this kind of disadvantage, a multiple parallel DC/DC boost converter design is usually used. Fig. 11 represents a two DC/DC boost converters in parallel. The components of two boost converters are similar where the gate signal is shifted by 180 degrees. The total current I is the sum of these two boost converter currents I_1 and I_2. The current passing through each device is 1/2 of the total input current [28].

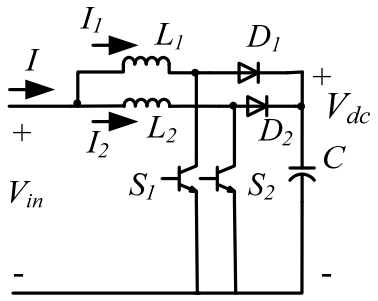

Figure 11: Two DC/DC boost converter in parallel.

In this thesis, three DC/DC boost converters are used in the system, as shown in Fig. 12. The total current is the sum of these three boost converter currents I_1, I_2, I_3. The current passing through each device is 1/3 of the total current. The three boost converters are operated in parallel with each control signal shifted by 120 degrees. This reduces harmonic distortion and inductor size, and furthermore, the current rating of the power device is reduced. The MPPT scheme now can be achieved by adding the three currents together to follow the total reference signal. Fig. 13 is the control scheme [28 -29].

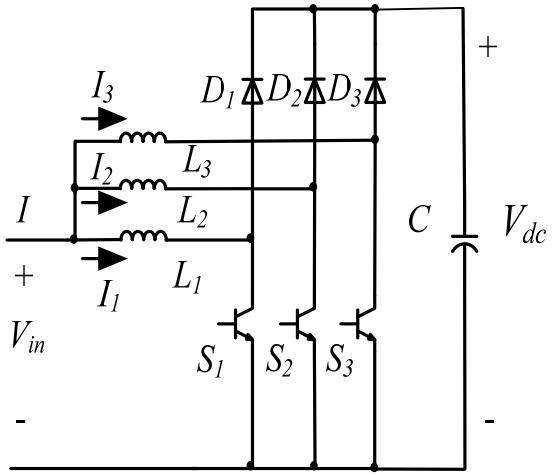

Figure 12: Three DC/DC boost converter.

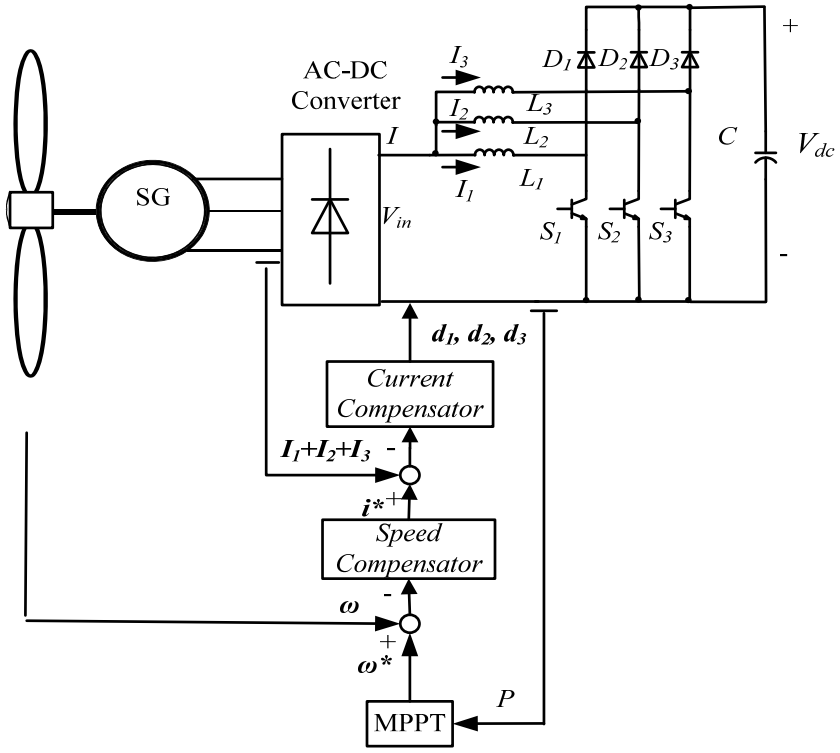

Figure 13: Control scheme for MPPT control.

In this chapter, the overall wind power generation system was discussed. A DC/DC boost converter was adopted to control the rotor speed of the generation to track the maximum power point. To reduce the current rating of the device, a multiple DC/DC boost converter and its control method were introduced. The next chapter will discuss the grid-side PWM inverter and its control method.

CHAPTER THREE

A New Current Controller Using Proportional plus Resonance Control

The previous chapter introduced the design, analysis of a wind power generation system, where the generator-side components, configuration and control scheme was mainly discussed. This chapter will focus on the grid-side inverter control scheme.

With the improvements in wind power conversion technologies, the wind power resources can easily be connected to the power grid. In the conventional wind power system, the direct-quadrant PI controller is used to reduce the harmonic distortion. But the PI controller exhibits two well known drawbacks: inability of the PI controller to track a sinusoidal reference without steady-state error and poor disturbance rejection capability. In order to eliminate these problems, a proportional plus resonance (PR) controller can be used. The PR controller is a double integrator that has an infinite gain at a certain frequency and almost no attenuation outside this frequency. Therefore, the PR controller can be used as a notch filter to compensate the harmonics in a very selective way.

In the conventional grid-side inverter system, an L filter was used to interface with the grid. To improve the attenuation ability for high frequencies, the L filter was replaced by an LCL filter, and a damping resistor was added to improve the stability of the filter. If the rated power of the system is large, the power loss on the damping resistor is also large. To decrease the power loss, a new control scheme named active damping without damping resistor is proposed in this chapter. In the conventional control method,

all control parameters were calculated in the synchronous frame (*dq*-frame) which is complex, while the control scheme proposed in this chapter calculates the parameters in the stationary frame ($\alpha\beta$-frame) which is easier and more accurate. Although the new control scheme needs one more current sensor than the conventional scheme, when the rated power goes high, comparing the reduction of the power loss and the cost of the sensor, this scheme becomes practical and economical.

Grid-Connected Inverter and LCL filter

The grid side DC/AC inverter introduced in this chapter is shown in Fig. 14. It consists of DC link, PWM three-phase inverter, LCL filter and the grid. In the conventional wind power system, the L filter (only one inductor) is used to interface with the grid to minimize the grid current harmonics, while a bulky size of L filter is required to achieve a good performance. Because of its better attenuation for switching frequency harmonics and its lower cost, LCL filter is popular for grid-connected power systems. An LCL filter consists of two inductors and one capacitor. The inductance of an LCL filter is much smaller than that of an L filter, but with the same ability to minimize the harmonics at the switching frequency. However, an LCL filter has its own drawbacks. Because of the peak at the resonance frequency, the LCL filter will increase instability of the overall control system. In the conventional LCL filter, a damping resistor is used to make the LCL filter stable but it will increase the power loss. To increase the stability of the system and to minimize the power loss, a novel control method based on the LCL filter without damping resistor is proposed in this chapter. Fig. 15 is the equivalent LCL filter model.

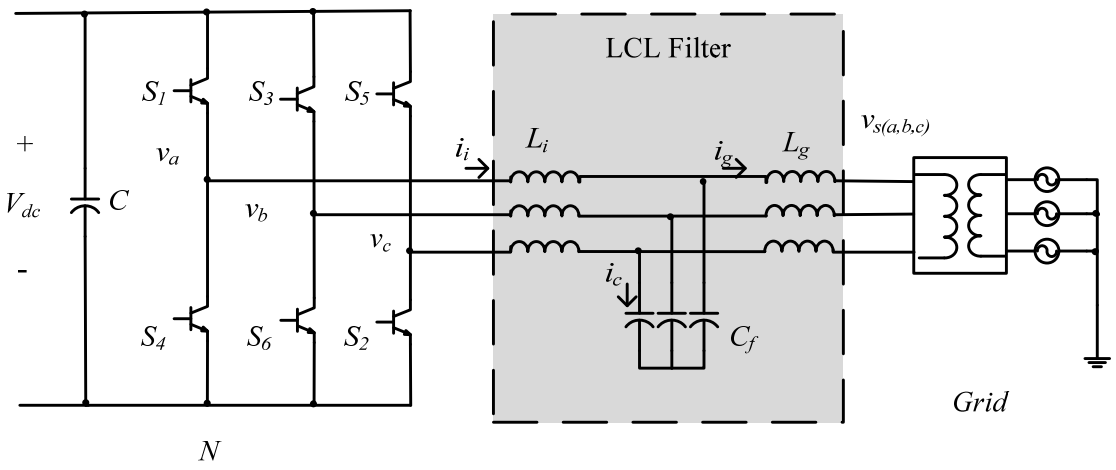

Figure 14: Grid-side DC/AC inverter.

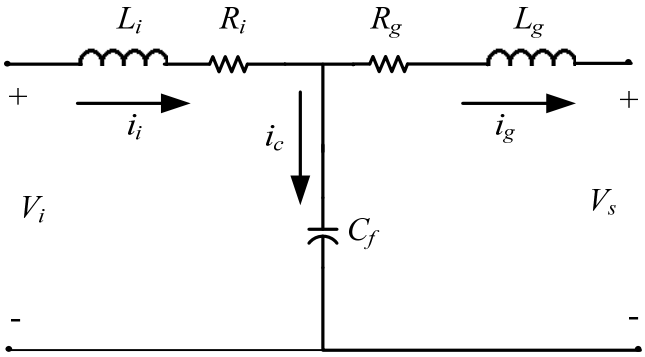

Figure 15: Equivalent LCL filter model.

Here, the LCL filter is composed of a grid-side inductor L_g and grid-side inductor resistance R_g; an inverter-side inductor L_i and an inverter-side inductor resistance R_i; and a capacitor C_f. $L_s = L_g + L_i$ is the total inductance of the filter. In Fig. 15, V_i is the inverter-side voltage and V_s is the grid voltage. The current flows from inverter side to the grid, i_i is the inverter-side current, i_g the grid current, and i_c the capacitor current. Fig. 16 shows the input filter model. The filter model in the s-plane can be written as (ignoring the influence of R_g and R_i) [30]:

$$
\begin{aligned}
i_i - i_c - i_g &= 0 \\
V_i &= i_i L_i s + V_c \\
V_s &= -i_g L_g s + V_c \\
V_c &= i_c \frac{1}{C_f s}
\end{aligned}
\tag{10}
$$

where

L_g = grid-side inductor filter

L_i = inverter-side inductor

C_f = capacitor

V_i = inverter-side voltage

V_s = grid voltage

V_c = the voltage of the capacitor.

i_i = inverter-side current

i_g = grid current

i_c = capacitor current

The inverter side and grid side currents can be derived as:

$$
\begin{aligned}
i_i &= \frac{1}{L_i s}(V_i - V_c) \\
i_g &= \frac{1}{L_g s}(V_c - V_s) \\
V_c &= (i_i - i_g)\frac{1}{C_f s}
\end{aligned}
\tag{11}
$$

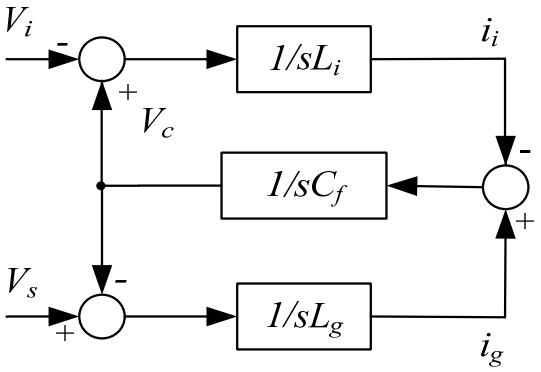

Figure 16: Input LCL filter model.

The grid voltage is assumed to be an ideal voltage source, it has a short circuit for harmonic frequencies, and it is set to zero for filter analysis ($V_s = 0$). Ignoring the influence of R_g and R_i, the transfer function of the model can be defined as:

$$G_{lcl}(s) = \frac{i_g}{V_i} = \frac{1}{L_g L_i C_f s^3 + s(L_g + L_i)} \tag{12}$$

On the other hand, the transfer function of L filter is:

$$G_l(s) = \frac{i}{V_i} = \frac{1}{L_s s} \tag{13}$$

where L_s is the total inductance of LCL filter.

Using the transfer functions of the two filters, the Bode plots are obtained to determine the ability of minimizing the harmonics at high frequencies. Fig. 17 is the Bode plot of these two kinds of filters.

These two kinds of filters have the same total inductance. The slopes of the LCL filter and the L filter before the resonance peak are almost the same (about -20dB/dec), and the LCL filter has a peak at the resonance frequency. To the right of the resonance frequency, the slope of the LCL filter becomes -60dB/dec while the slope of the L filter stays the same (-20dB/dec). Thus, the LCL filter has a better attenuation of high

frequency harmonics than the L filter. In other words, if the attenuation of harmonics is the same, an LCL filter needs less total inductance than an L filter. At the resonance frequency, the total impedance of the filter is zero, which will destroy the stability of the control system. To increase stability, a damping resistor is connected in series with the capacitor filter. This kind of filter is called passive damping filter shown in Fig. 18, where R_d is the damping resistor to stabilize the LCL filter. Fig. 19 is the Bode plot of the LCL filter, with and without the passive damping resistor R_d. With R_d, the peak at the resonance frequency is much lower than that without R_d in the LCL filter, but the slope at high frequencies decreases slightly.

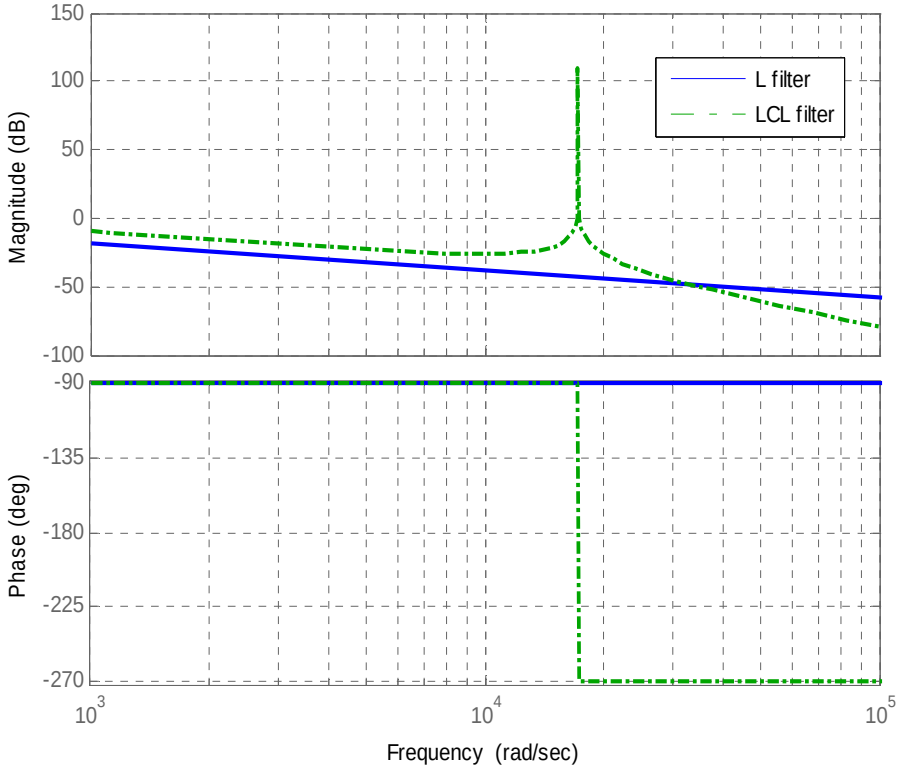

Figure 17: Bode plots of LCL filter and L filter.

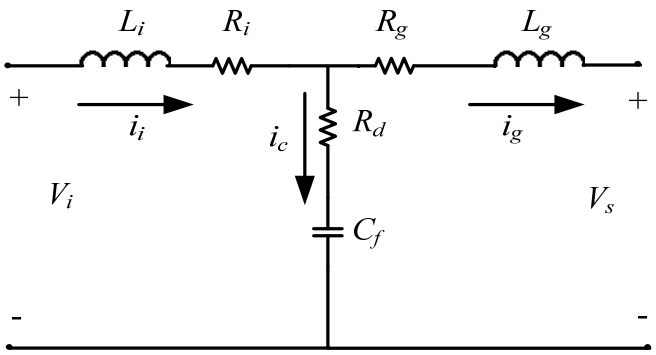

Figure 18: LCL filter with damping resistor.

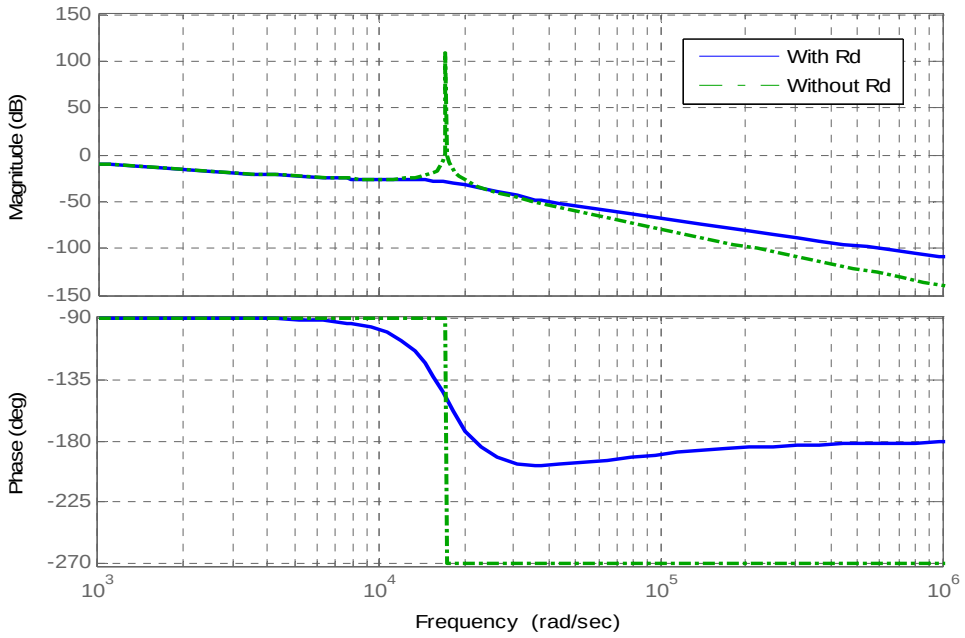

Figure 19: Bode plot of LCL filter with and without R_d.

Using a damping resistor can increase the stability of the control system, but at same time, it will also increase the power loss of the wind power system. If the rated power of the overall system is large, the power loss is considerably large too. To have a good attenuation of the harmonics and a lower power loss, a new control scheme is

introduced based on the LCL filter without damping resistor. This kind of method is called active damping and will not introduce power loss to the system.

This section introduced the grid-connected LCL filter, with its modeling and transfer function. Compared to the L filter, the LCL filter has a better attenuation at high frequencies. To increase the stability of the system, a damping resistor was used in the conventional method.

LCL Filter Design Optimization

There are many tradeoffs when designing an LCL filter, the total inductance should be large to have lower harmonic distortion, but it will also slow down the system response. To have a high power factor, the capacitor should not be too large since it absorbs reactive power. And the damping resistor should not be too large since it would produce a large power loss.

The following is assumed for the filter design:

The rated power of the wind power system $P = 250kW$, DC bus voltage $V_{dc} = 600V$, grid frequency $f = 60Hz$, PWM carrier frequency $f_{pwm} = 3kHz$, and the line-to-line *rms* based voltage $V_{ab(L\text{-}L)} = 208V$.

According to the principles of LCL filter design, parameters are calculated in several steps:

First, the overall inductance value of L_s is chosen. To improve the current tracking ability and the system response speed, L_s should be small; however, we can have better filter effect if L_s is large. Here we choose a suitable value of L_s [31]

$$\frac{v_{dc}}{4\sqrt{3}i_{ripple}f_{sw}} \le L_s \le \frac{\sqrt{\frac{v_{dc}^{\ 2}}{3} - E_m^{\ 2}}}{\omega I_m} \tag{14}$$

where E_m is the peak phase voltage of grid, I_m is the peak current of grid, f_{sw} is the switching frequency, and i_{ripple} is current ripple, which is set to be 20% of I_m.

Second, the capacitance value of C_f is chosen. To avoid the lower power factor, generally the reactive power absorbed from the capacitor should be less than 5% of the nominal power of the system [31]:

$$C_f \le \frac{0.05 \cdot P_n}{3 \cdot 2\pi \cdot f_n \cdot E_n^{\ 2}} \tag{15}$$

where f_n is the grid frequency and E_n is *rms* value of phase voltage, and P_n is rated power produced by the grid-side inverter.

Finally, choose the inductance values of L_g and L_i. The chosen ripple attenuation of high order harmonics at the switching frequency is g, and r (= L_g/L_i) is defined. The selected g, C_f, and L_s are related as a positive solution of the following equation:

$$g^2 + (2g + 1 - g\omega_{sw}^{\ 2} L_s C_f) \cdot r + g + 1 = 0 \tag{16}$$

If the solution is not positive, the values of d, C_f, L_s should be rechosen to obtain a positive solution.

Using r (= L_g/L_i), we can get L_i and L_g as

$$L_i = \frac{L_s}{1+r}$$
$$L_g = rL_i \tag{17}$$

It is necessary to check the resonant frequency to satisfy the following equation:

$$10f_n \le f_{res} \le 0.5f_{sw} \tag{18}$$

where f_n is the nominal frequency of the grid and the resonant frequency f_{res} is given by[31].

$$f_{res} = \frac{1}{2\pi}\sqrt{\frac{L_i + L_g}{L_i L_g C_f}} \tag{19}$$

If it does not satisfy the equation, the parameters should be chosen again.

TABLE I: Parameters of System

Parameter	Description	Value
L_i	Inverter side inductor filter	0.18mH
R_i	Inverter side inductor resistance	0.034Ω
R_g	Grid side inductor resistance	0.007Ω
L_g	Grid side inductor filter	0.036mH
C_f	Capacitor filter	0.00076F
f_{pwm}	PWM carrier frequency	3kHz
f	Grid frequency	60Hz
P_{out}	Nominal power	250kW
$v_{ab(L\text{-}L)}$	Line-to-line rms base voltage	208V
V_{dc}	DC bus voltage	600V

From the three steps above, the LCL parameters are obtained as in TABLE I

In this section, a detailed design procedure of an LCL filter was discussed, and based on the wind power generation system. All the parameters of LCL filter were calculated to meet the requirements.

Conventional PI Current Controller

Current regulation is an important issue for power electronic converters and inverters. Over the last few decades, much research has been done in this area for voltage source inverters. A PI controller is commonly used for a fixed switch frequency. However, the common PI controller for static coordinates (*abc* three-phase frame) has difficulty eliminating steady-state error for AC current reference since a PI controller has the infinite gain only at DC zero frequency. Consequently, if the reference becomes AC, then the PI controller does not work well. A coordinate transformation (*abc-dq*) is used to solve such problem. For a synchronous rotating frame (*dq* frame), an AC reference becomes a DC reference and zero steady-state error can be realized with a PI controller. Fig. 20 shows the control diagram of a PI controller with an L filter for simplicity.

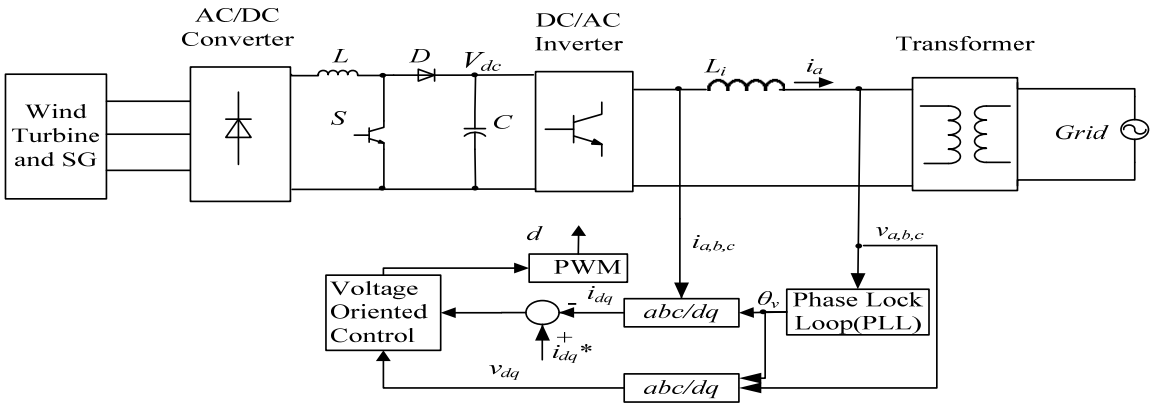

Figure 20: Conventional control diagram of DC/AC inverter.

In Fig. 14, the voltages and currents of the inverter at low frequency can be written as [32]:

$$\begin{bmatrix} v_a \\ v_b \\ v_c \end{bmatrix} = R_s \begin{bmatrix} i_{sa} \\ i_{sb} \\ i_{sc} \end{bmatrix} + L_s \frac{d}{d_t} \begin{bmatrix} i_{sa} \\ i_{sb} \\ i_{sc} \end{bmatrix} + \begin{bmatrix} v_{sa} \\ v_{sb} \\ v_{sc} \end{bmatrix} + \begin{bmatrix} v_N \\ v_N \\ v_N \end{bmatrix} \tag{20}$$

where, v_{sa}, v_{sb}, and v_{sc} are the grid voltages, and v_a,v_b, and v_c are the inverter output voltages. Currents i_{sa} i_{sb} and i_{sc} are the grid current of A,B and C phase, R_s and L_s are the values of the resistance and the reactance ($L_s = L_i+L_g$) in the filter and v_N is the voltage between N and ground. The neutral voltage v_N is considered to be zero in the conventional three-phase inverter with balanced load. After *abc-dq* transformation, (20) becomes as:

$$\begin{bmatrix} v_d \\ v_q \end{bmatrix} = R_s \begin{bmatrix} i_{sd} \\ i_{sq} \end{bmatrix} + L_s \frac{d}{dt} \begin{bmatrix} i_{sd} \\ i_{sq} \end{bmatrix} + L_s \omega \begin{bmatrix} i_{sq} \\ i_{sd} \end{bmatrix} + \begin{bmatrix} v_{sd} \\ v_{sq} \end{bmatrix} \tag{21}$$

where ω is the angular speed of the synchronous reference frame. The d-axis is synchronized with the grid-voltage space vector, thus v_{sq} is zero [33]. There are coupling terms in (21), and thus a feed-forward term to decouple the control system is used. Fig. 21 shows the decoupled current control loop diagram.

The synchronous frame PI controller is more complex, as it requires transforming a measured stationary frame ac current to a rotating frame dc quantities, and transforming the resultant control action back to the stationary frame for execution. If the frame transformation is not accurate, errors could be introduced at the synchronous compensation network. And a further disadvantage of PI control is that it is not easy to be implemented for single-phase current regulated systems, where synchronous frame transformations are more difficult to apply [34-36].

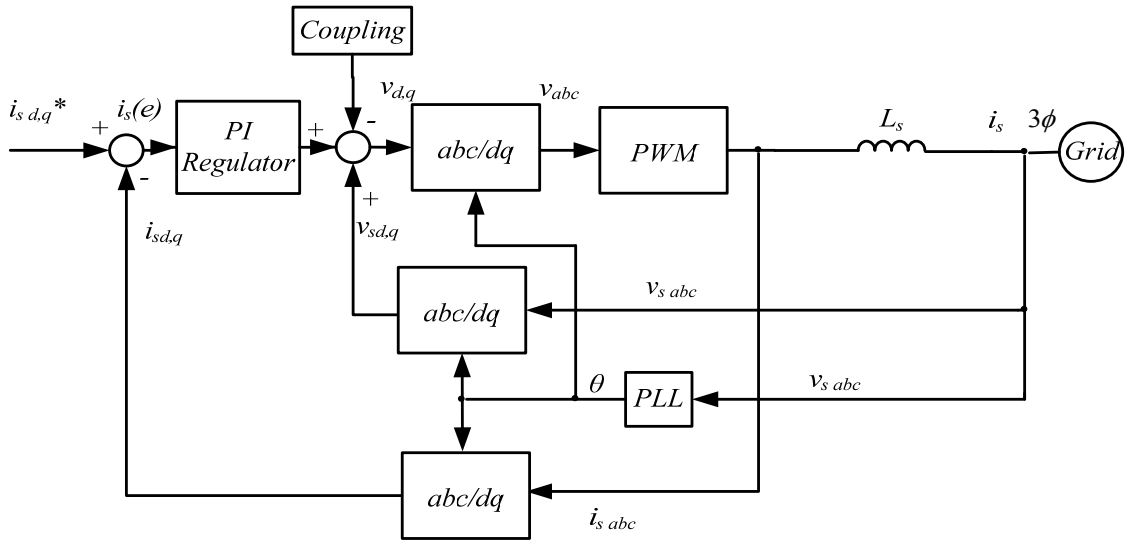

Figure 21: Current control loop with PI.

Proposed Current Controller using PR Control

To overcome the disadvantages of a PI controller, an alternative approach is proposed to use proportional plus resonance (PR) control, which is the frequency transformation of the dc type controller into an equivalent ac regulator. This results in an equivalent stationary frame current controller with theoretically identical performance of the synchronous frame current controller. A PR controller can provide infinite gain at a specific frequency and achieve zero steady-state error in a stationary frame. Also, it is applicable to either single-phase or three-phase systems. When the reference signal bandwidth is small in comparison with the reference frequency itself, we can use the following transformation to obtain a PR controller from a PI controller [37]:

$$G_{AC}(s) = G_{DC}\left(\frac{s^2 + \omega^2}{2s}\right) \tag{22}$$

A dc controller can be transformed into an equivalent ac controller. Thus, considering a conventional PI controller transfer function,

$$G_{DC}(s) = K_p + \frac{K_i}{s} \tag{23}$$

the equivalent ac controller (PR controller) can be obtained as:

$$G_{AC}(s) = K_p + \frac{2K_i s}{s^2 + \omega^2} \tag{24}$$

where, ω is the fundamental frequency of the grid, and K_p and K_i in these two transfer functions are the same. Fig. 22 shows the bode plots of PI and PR transfer functions for two arbitrary K_p, K_i. The figure shows that the magnitude of (24) becomes infinite at the specific frequency and that is why this kind of controller can track AC reference values with no phase or magnitude errors. After the infinite gain at the specific frequency (usually the fundamental frequency of the grid), the magnitudes and phases of these two kinds of controller are almost the same.

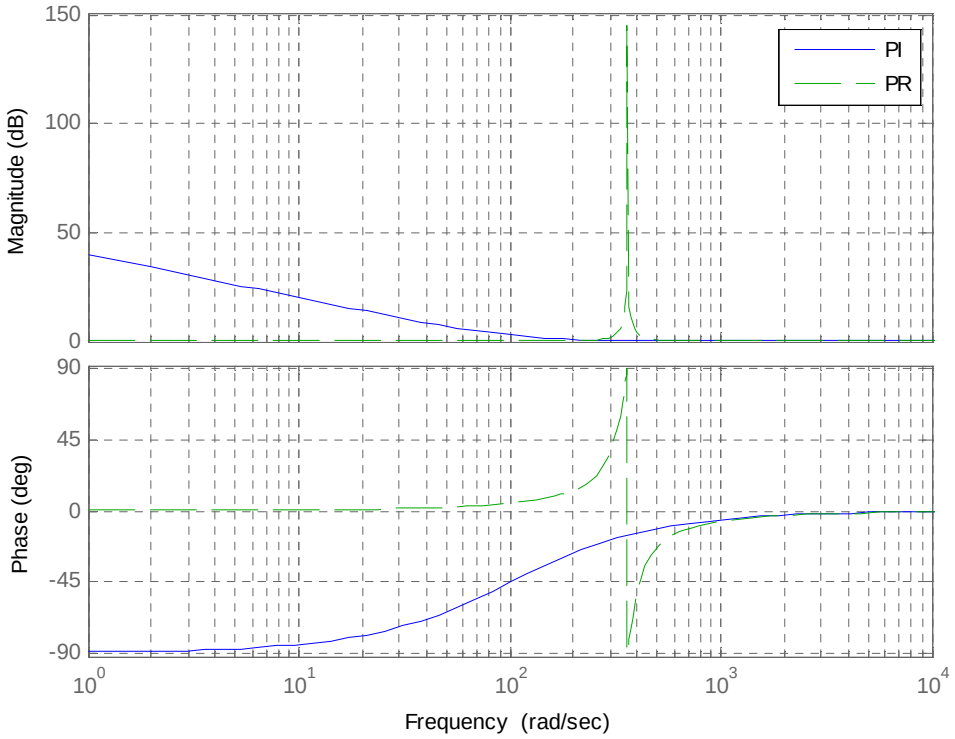

Figure 22: Bode plots of PI and PR controller.

With the PR controller we are working at the stationary frame, and thus we do not have the complexity of transforming a measured ac current in stationary frame to dc quantities in rotating frame. The system response can be improved because we do not have error involved in the coordinate transformations. A harmonic compensator (HC) $G_h(s)$ can be used to eliminate the 3rd, 5th, and 7th harmonics because they are the most prominent harmonics in the current spectrum. $G_h(s)$ is defined as [37-38]:

$$G_h(s) = \sum_{h=3,5,7} K_{ih} \frac{s}{s^2 + (\omega h)^2} \tag{25}$$

where h is the order of the harmonics.

Fig. 23 shows the Bode plot of $G_h(s)$, with peaks at the fundamental, 3rd, 5th and 7th order harmonics.

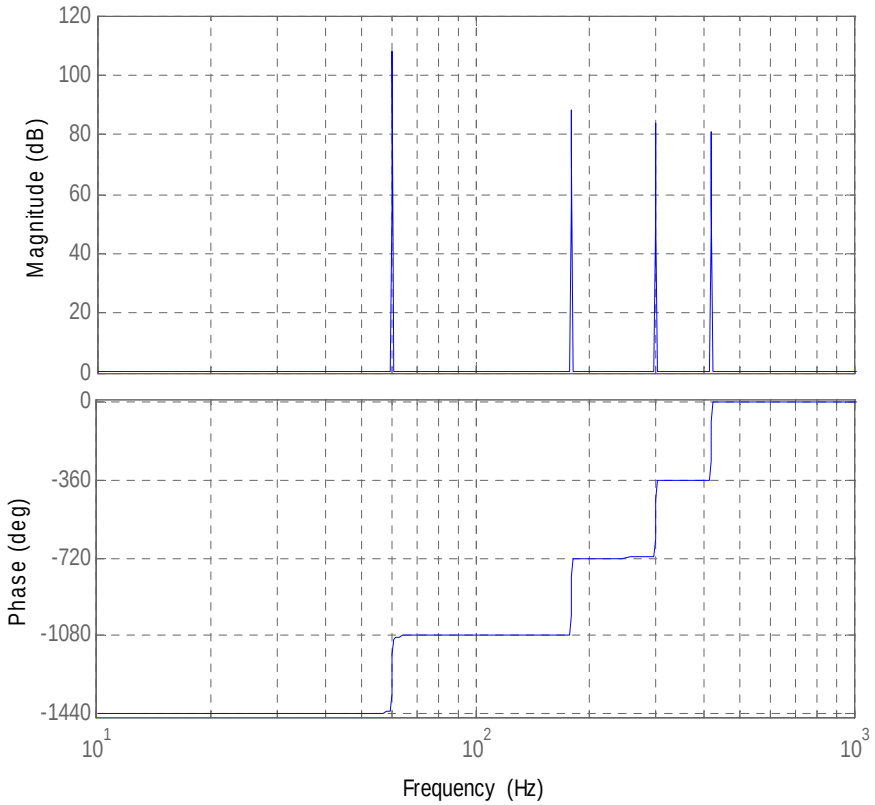

Figure 23: Bode plot of harmonics compensator.

Next, a controller design will be discussed with a new two-current loop. The control scheme is based on the coordinate transformation. In electrical engineering, coordinate transformation is a mathematical transformation used to simplify the analysis of three-phase circuits. In the case of balanced three-phase circuits, application of the coordinate transformation reduces the three AC quantities to two AC or DC quantities. It is often used in order to simplify the analysis of three-phase synchronous machines or to simplify calculations for the control of three-phase inverters. In Fig. 14, the three-phase circuit can be transformed into two single decoupled circuits using a *abc-αβ* transformation which is described in Appendix B, (R_i and R_g are the resistors associated with inverter side and grid-side inductors, respectively):

$$\begin{aligned} L_i \dot{i}_{ik} &= v_k - (i_{ik} R_i + v_{ck}) \\ L_g \dot{i}_{sk} &= v_{ck} - v_{sk} - i_{sk} R_g \\ C_f \dot{v}_{ck} &= i_{ik} - i_{sk} \end{aligned} \tag{26}$$

where i_{ik} is the inverter-side current, i_{sk} is the grid-side current, v_k is the inverter side voltage, v_{sk} is the grid voltage, and v_{ck} is the capacitor voltage, with $k = \alpha, \beta$, (α, β is the stationary frame using *abc- αβ* transformation). Fig. 24 is the single-phase circuit.

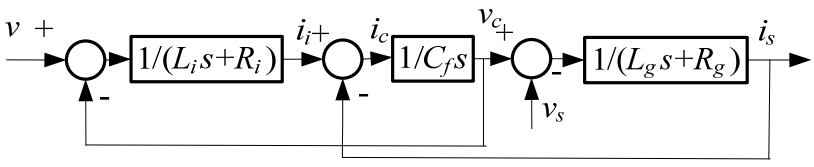

Figure 24: Single-phase block diagram with LCL filter.

In the conventional control method, a single grid current loop controller is used based on LCL filter with damping resistor. If the damping resistor is eliminated, the

single loop is not sufficient for the stability of the system. To obtain a steady control system, a multi-loop is introduced where the capacitor current is used as inner-loop variable. Since the inner loop doesn't affect the accuracy of the outer loop, a proportional controller *K* is used for inner loop, and for the outer loop a proportional resonance controller (PR controller) is used. The PR controller has the same frequency response with PI controller but at different coordinates. However, for simplicity, the PI controller is used instead of a PR controller. Then, after the parameters are calculated, the PR controller will be used and analyzed. Fig. 25 shows the control block of the system. The inner feedback is the filter capacitor current and the outer feedback is the grid current. The outer PR controller $G_c(s)$ is tentatively assumed as the PI controller, $K_p + K_i / s$.

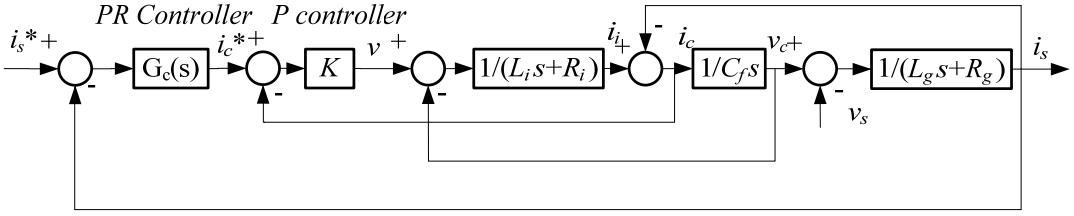

Figure 25: Proposed two-current loop control block diagram.

The open-loop transfer function and closed-loop transfer function with the PR controller are calculated from Fig. 25.

$$G_{op}(s) = \frac{a_0 s + a_1}{b_0 s^4 + b_1 s^3 + b_2 s^2 + b_3 s} \tag{27}$$

$$G_{cl}(s) = \frac{a_0 s + a_1}{b_0 s^4 + b_1 s^3 + b_2 s^2 + (b_3 + a_0) s + a_1} \tag{28}$$

where $a_0 = K_p K$, $a_1 = K_i K$, $b_0 = L_i L_g C_f$, $b_1 = R_i L_g C_f + R_g L_i C_f + L g C_f K$, $b_2 = L_i + L_g + R_i R_g C_f + R g C_f K$, $b_3 = R_i + R_g$.

Fig. 26 shows the root locus of the system. K and K_i are fixed ($K = 0.5$, $K_i = 80$) and K_p is a variable because the system stability is primarily determined by K_p.

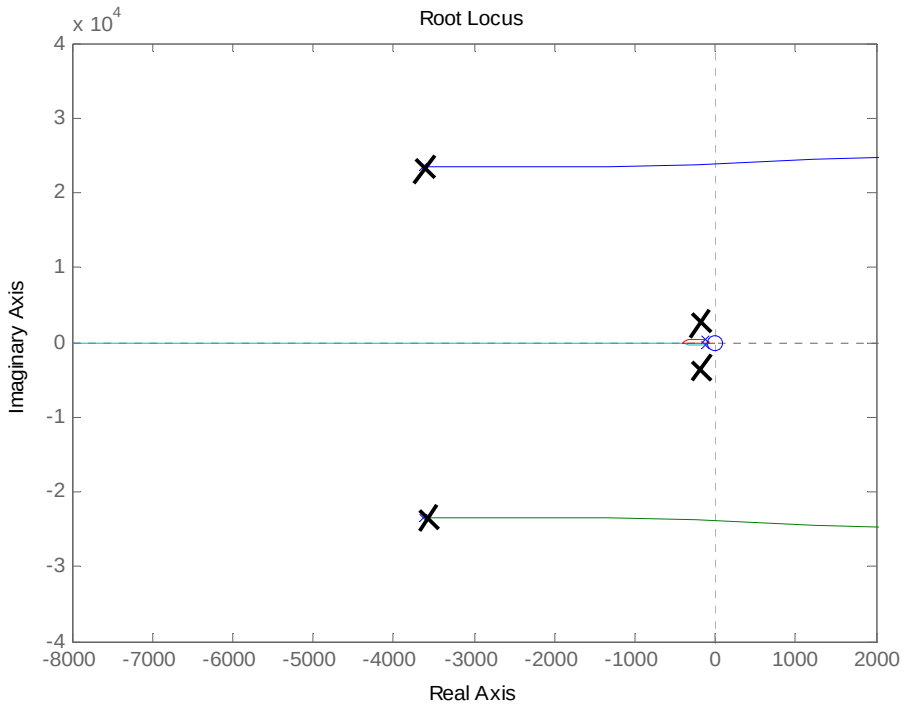

Figure 26: Root locus of system (K and K_i are fixed (K=0.5, K_i=80) and K_p is variable.

There are two conjugate poles and two other poles near the zero at the origin of the coordinate. When K_p increases, the two conjugate poles will move towards the imaginary axis and finally go into the right-half plane. And one of the two poles near the zero will go further from the imaginary axis, while the other one will move towards the zero. When gain is 0, the conjugate poles are at $-3627 \pm 23550i$. We can make the conjugate poles as dominate poles with a large K_p and also make one pole at the same place as the only zero, so the impact of this pole can be eliminated. And the other pole is put far away from the imaginary axis. Then, the conjugate poles will be the dominate poles and become the main factor to influence the response and other

characteristics of the system. Hence the numerator of the closed-loop transfer function is a factor of the denominator to make a pole and zero to be canceled. After the same factors of the denominator and numerator are cancelled, a new third order transfer function can be obtained as:

$$G_{op\_new}(s) = \frac{x_0}{s^3 + (y_1 - x_1)s^2 + (y_2 - x_1(y_1 - x_1))s} \tag{29}$$

$$G_{cl\_new}(s) = \frac{x_0}{s^3 + (y_1 - x_1)s^2 + (y_2 - x_1(y_1 - x_1))s + x_0} \tag{30}$$

where $x_0 = a_0 / b_0$, $x_1 = a_1 / a_0$, $y_1 = b_1 / b_0$, $y_2 = b_2 / b_0$.

The pole-zero cancelled transformation should satisfy the following using long division.

$$y_3 - x_1(y_2 - x_1(y_1 - x_1)) = 0 \tag{31}$$

where $y_3 = b_3 / b_0$.

The transfer function (30) can be considered to be a third-order system with a dominant pair of roots and a third pole, which can be transformed into:

$$G_{cl\_new}(s) = \frac{x_0}{(s^2 + 2\zeta\omega_n s + \omega_n^2)(1/\tau + s)} \tag{32}$$

when $\tau << 1/\zeta\omega_n$, the third pole will have little effect on the step response of the control system. Usually, $|1/\tau| \geq 10|\zeta\omega_n|$, here 10 is used. The combination of (30) and (32) yields:

$$\begin{aligned} y_1 - x_1 &= 12\zeta\omega_n \\ y_2 - x_1(y_1 - x_1) &= (20\zeta^2 + 1)\omega_n^2 \\ y_3 - x_1(y_2 - x_1(y_1 - x_1)) + x_0 &= 10\zeta\omega_n^3 \end{aligned} \tag{33}$$

Then, the combination of (31) and (33) yields:

$$12\zeta b_3 - (20\zeta^2 + 1)\omega_n b_2 + (20\zeta^2 + 1)^2 \omega_n^3 b_0 = 0 \tag{34}$$

Firstly, ζ is chosen according to a specific requirement. And here $\zeta = 0.6$ is used. From (33) and (34), K_p, K_i, K, ω can be calculated: $K = 0.9$, $K_i = 29.1$, $K_p = 0.1$, $\omega = 8326$. The poles and zeros of the closed-loop transfer function (28) are shown in Fig. 27 and Fig. 28.

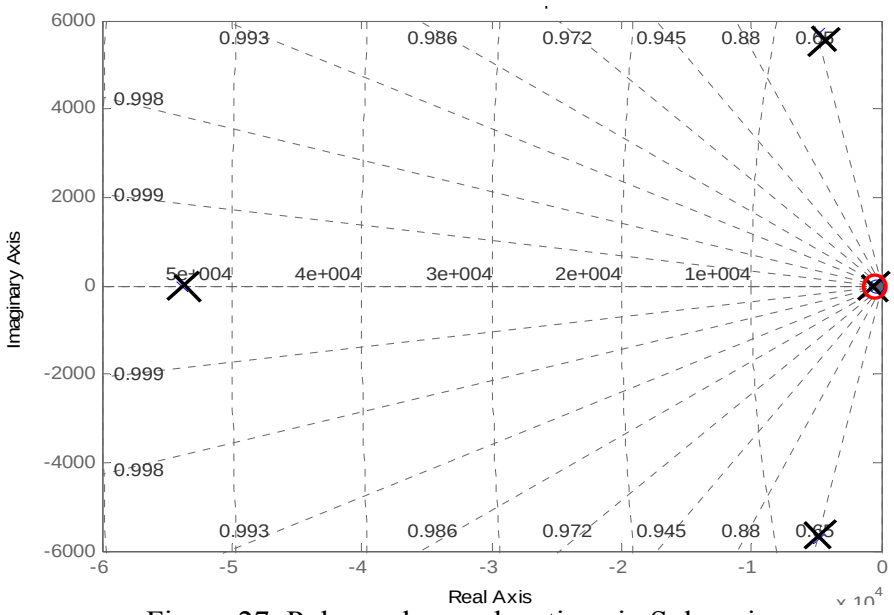

Figure 27: Poles and zeros locations in S domain.

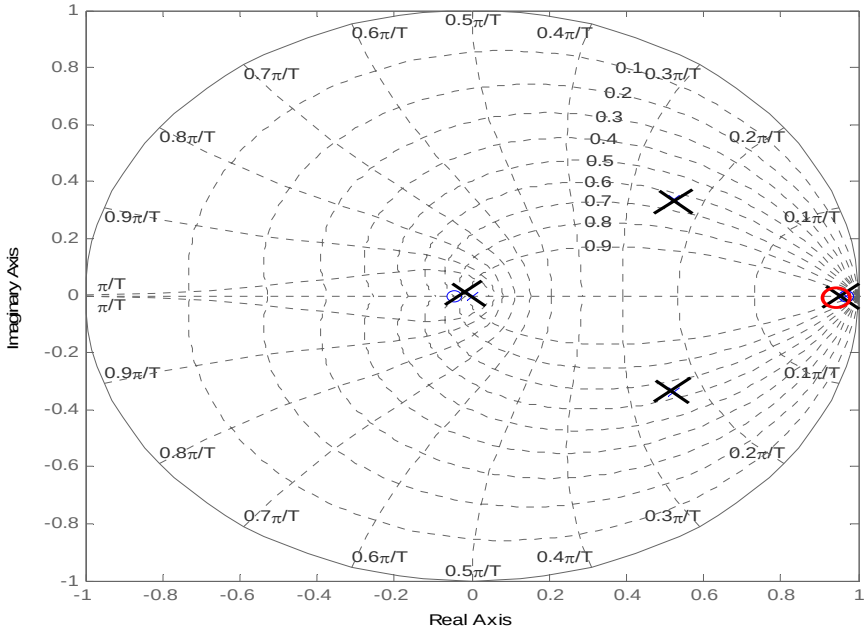

Figure 28: Poles and zeros locations in Z domain.

The position of the poles and zeros are located where we would expect. One zero and one pole are almost at the same place and one pole stays far away from the pair of dominant conjugate poles. The dominant poles are located at $0.524 \pm 0.336i$, the pole/zero are located at 0.971 and the last pole is located at 0.00461 in Z domain. Second, we then use the Routh's Stability Criterion to make sure the system is stable. All parameters should satisfy (35):

$$\begin{aligned} & b_0 > 0 \\ & b_1 > 0 \\ & b_2 > 0 \\ & b_3 + a_0 > 0 \\ & a_1 > 0 \\ & b_1 b_2 - b_0 (b_3 + a_0) > 0 \\ & b_1 b_2 - b_0 (b_3 + a_0) > b_1^2 a_1 / (b_3 + a_0) \end{aligned} \tag{35}$$

The open-loop Bode diagram is shown in Fig. 29. The phase margin is 60.3 deg and the gain margin is 21.6 dB. Thus, the system is stable using the calculated parameters.

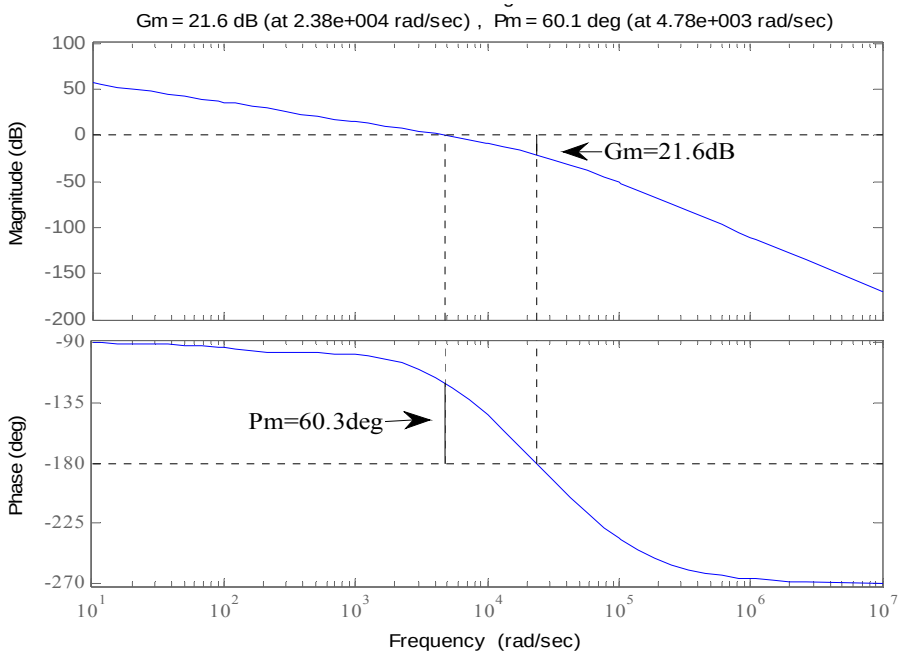

Figure 29: Bode diagram of the open-loop system.

The previous parameters are calculated based on ζ = 0.6, and ζ is not a fixed number and it can be set to other values. Fig. 30 shows the open-loop Bode plots with different value of ζ. For example, the phase margin increases from 48.9 degree to 61.4 degree when ζ increases from 0.5 to 0.7.

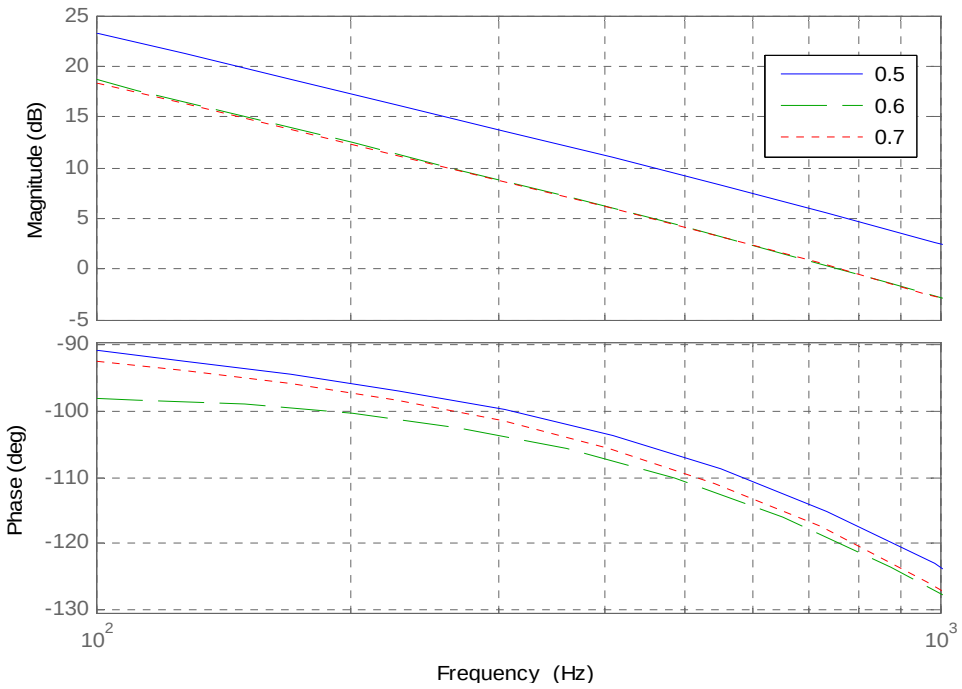

Figure 30: Open-loop Bode plot with different ζ.

As we know, the impedance of the grid can change, consequently the calculated parameters may also change. For example, when the grid side inductor filter changes 50%, the open-loop Bode diagrams are shown in Fig. 31. The phase margin changes from 65.7 degree to 55.4 degree.

Fig. 32 and Fig. 33, respectively, show the Bode plots when inverter side inductance filter and capacitance filter change. The phase margin changes from 48.7

degree to 70.1 degree and from 67.3 degree to 53.1 degree, respectively. Thus, when the grid impedance is changing, the control system can still be stable.

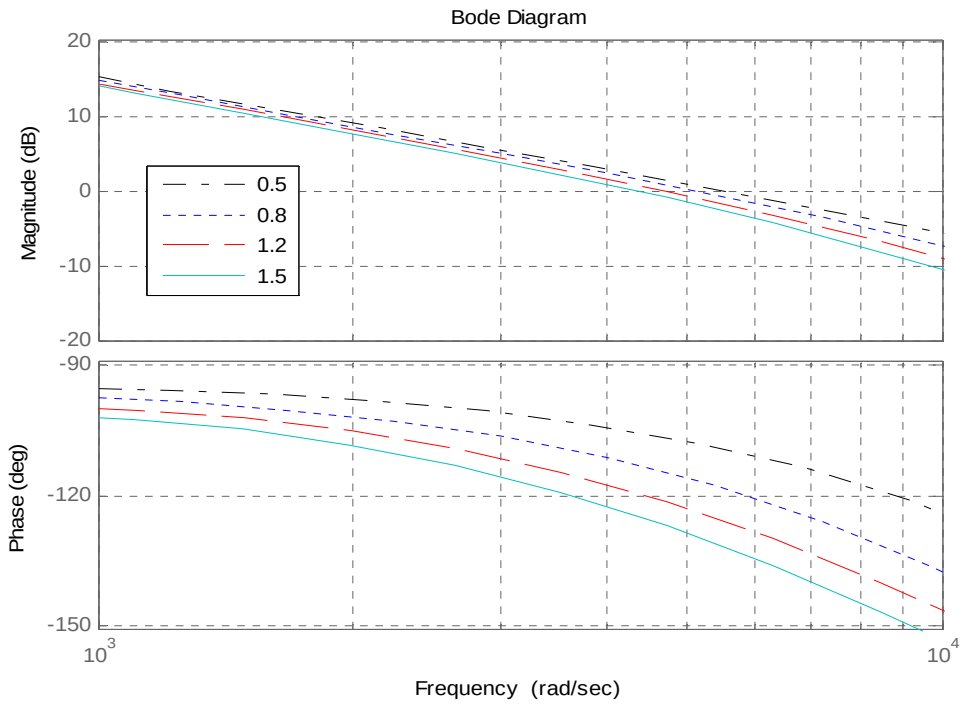

Figure 31: Bode diagram when grid inductance changes from 0.5 p.u – 1.5 p.u.

In a real control system, a PI controller will be substituted by a PR controller in stationary frame. The parameters are all same for either controller. The PR controller is used for simulation in the next chapter.

Fig. 34 is the closed-loop Bode plot of the system. It shows that the bandwidth of the current controller is about 1,290Hz. The PI controller and PR controller have the same frequency response and thus they have the same closed-loop Bode plot.

In this section, a new control scheme was introduced for a current loop. A PR control is easier and more accurate than a PI control, and a detailed design procedure was discussed. The Bode plots verified the stability of the control system and practicability of

the design method when the grid is not stable and the parameters of the filter were changing. The inner current loop was designed with a higher bandwidth to have a faster response.

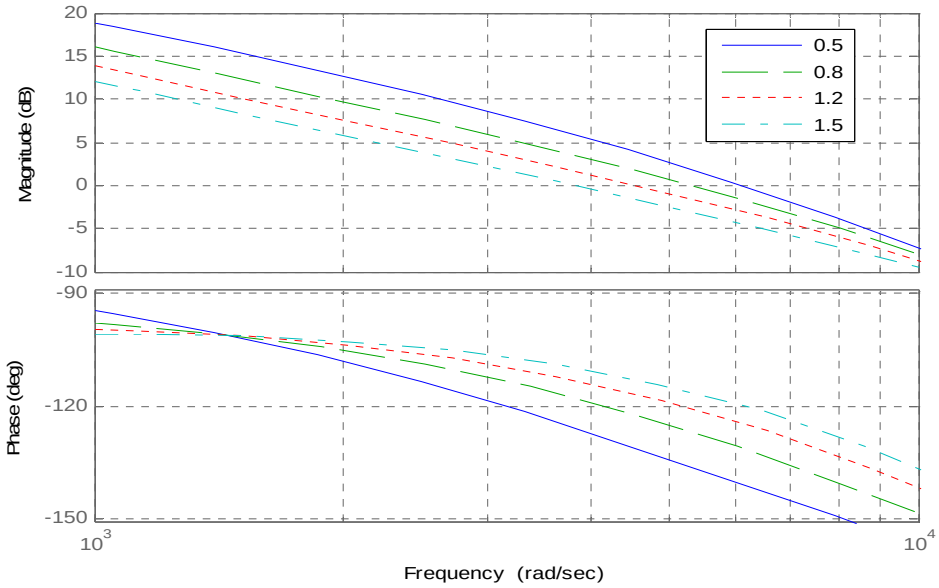

Figure 32: Bode diagram when inverter side inductance changes from 0.5 p.u – 1.5 p.u.

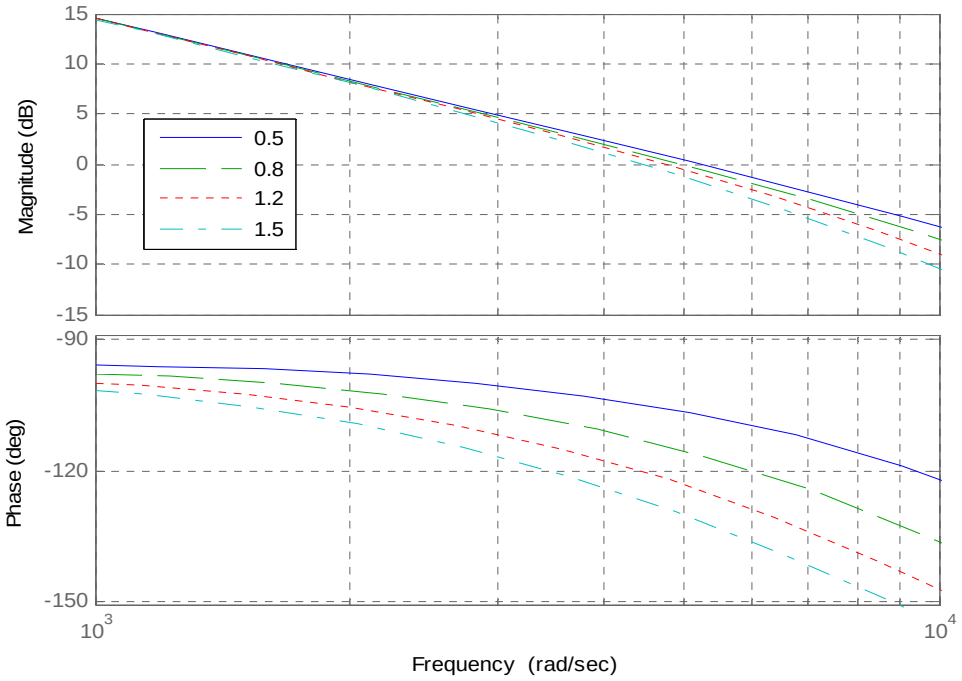

Figure 33: Bode diagram when capacitance changes from 0.5 p.u – 1.5 p.u.

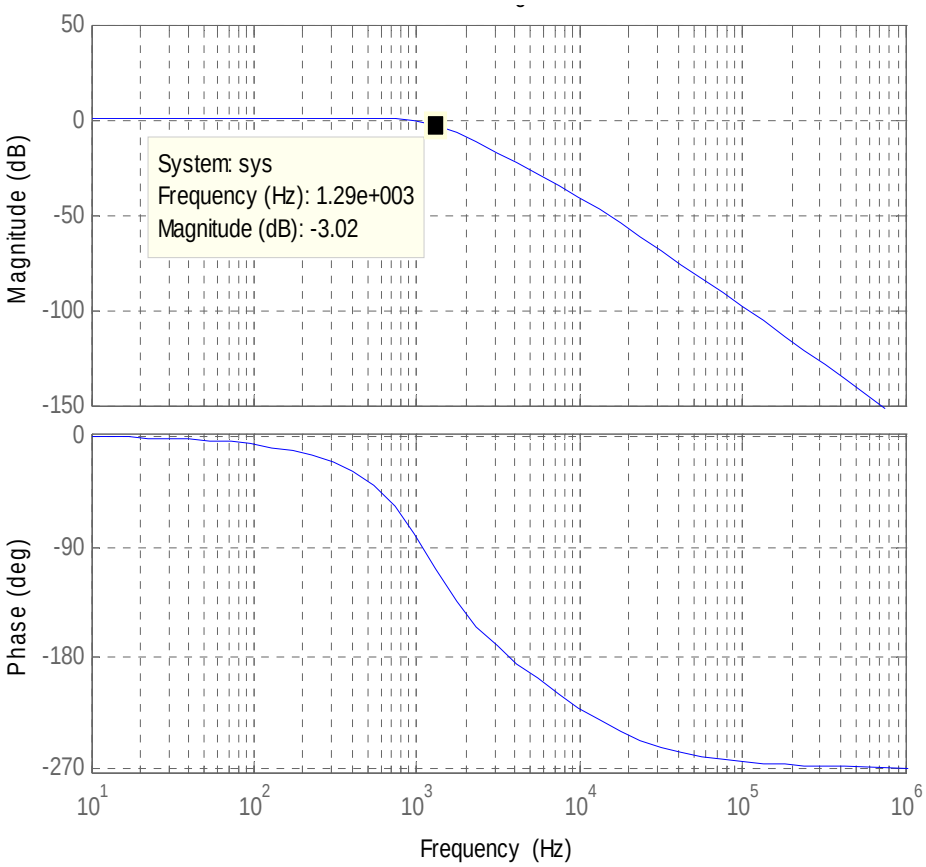

Figure 34: Bode diagram of closed-loop system.

DC Voltage Control

The overall controller has an inner loop which is a two-current loop and an outer loop which is a DC voltage loop. The inner loop design method has been discussed in the previous section, whereas this section discusses how to design the outer voltage loop which keeps the DC capacitor link voltage constant. The control structure is shown in Fig. 35. The voltage of DC capacitor link is compared with the reference DC voltage, and produces the reference signal of the inner current loop, and then produces the reference of the voltage signal to produce the gate signal. The inner current loop has a faster dynamic response and the outer loop has a smaller bandwidth to have slower settling times so that these two loops can be decoupled and designed separately.

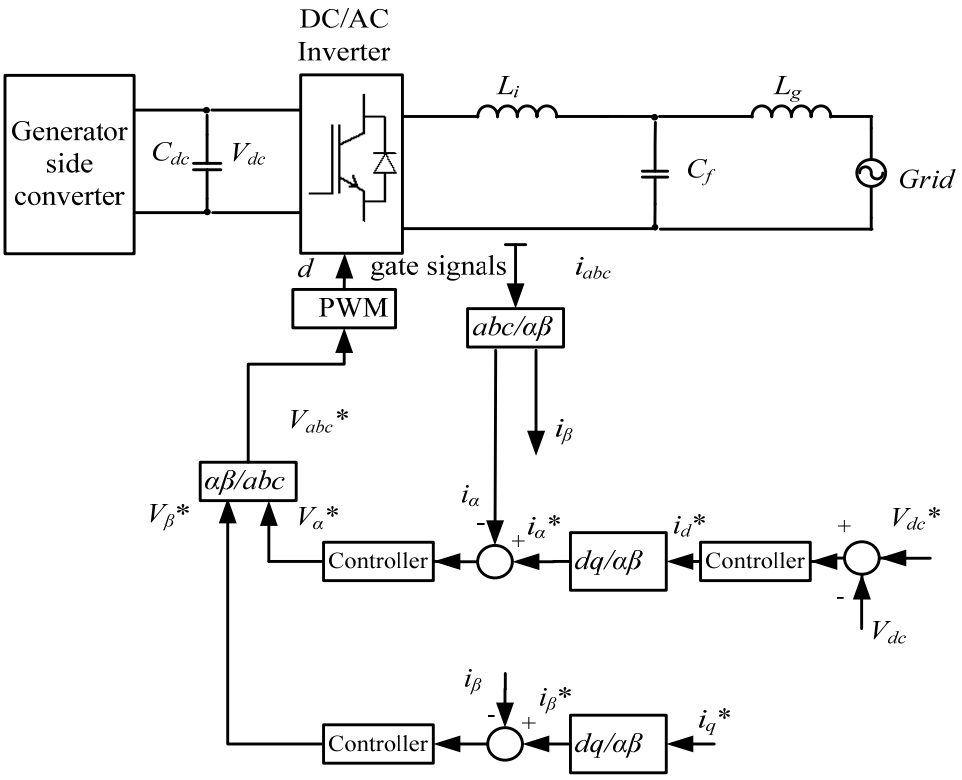

Figure 35: Control structures of voltage and current loop.

The DC link voltage controller adopt PI controller and the control diagram is shown in Fig. 36. The feedback sensor is set to be one and the plant model is as follows [39]:

$$G_{dc} = \frac{3s_d}{4}\frac{1}{C_{dc}s} \tag{36}$$

where s_d is the steady-state signal of the switching on the d-axis which is averaged to 1.

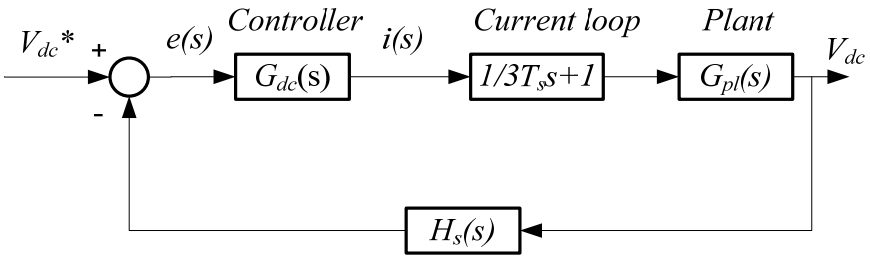

Figure 36: Voltage control loop diagram.

Since the inner loop is much faster than outer loop, when designing the outer loop, the inner loop can be regarded as a delay and T_s is the switching period. The $G_{dc}(s)$ is a PI controller: $G_{dc} = K_{pdc}(1+1/T_i s)$, using the optimum symmetrical method[36], we can obtain the parameters as follows:

$$\begin{aligned} K_{pdc} &= \frac{4C_{dc}}{9aS_d T_s} = 833 \\ T_i &= 3a^2 T_s = 0.0017 \\ a &= \frac{1+\cos(\phi)}{\sin(\phi)} = 2.4 \end{aligned} \tag{37}$$

where ϕ is the phase margin, and here 45 degree is used.

Fig. 37 shows the open-loop Bode diagram. The phase margin is 44.4 degree. And Fig. 38 shows the closed-loop Bode diagram. The bandwidth of the outer loop is about 441Hz which is smaller than the inner loop (1,290Hz). Thus, it has a slower dynamic response than the inner current loop, but provides a better turbulence rejection ability to keep the DC capacitor voltage constant.

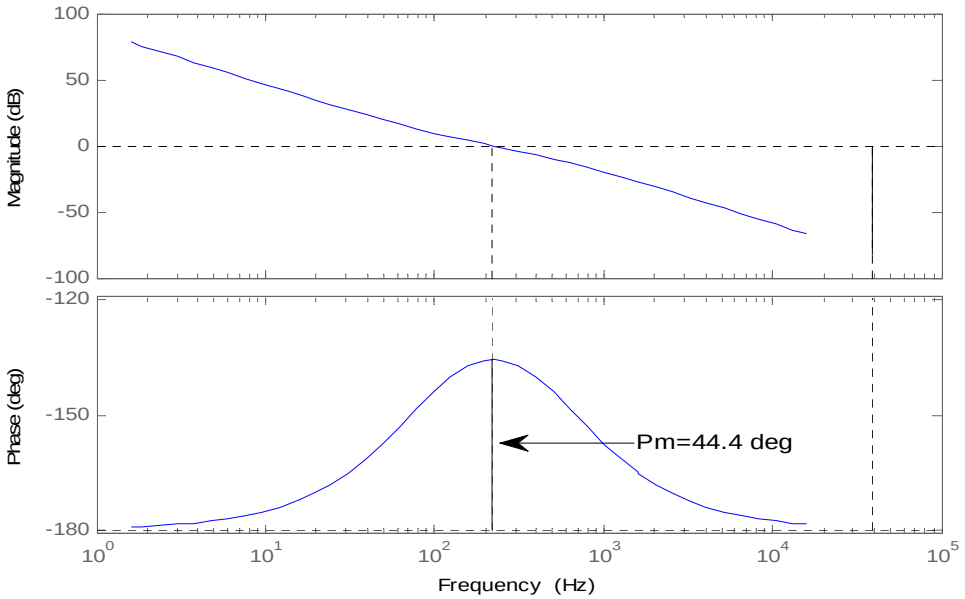

Figure 37: Bode diagram of open-loop system.

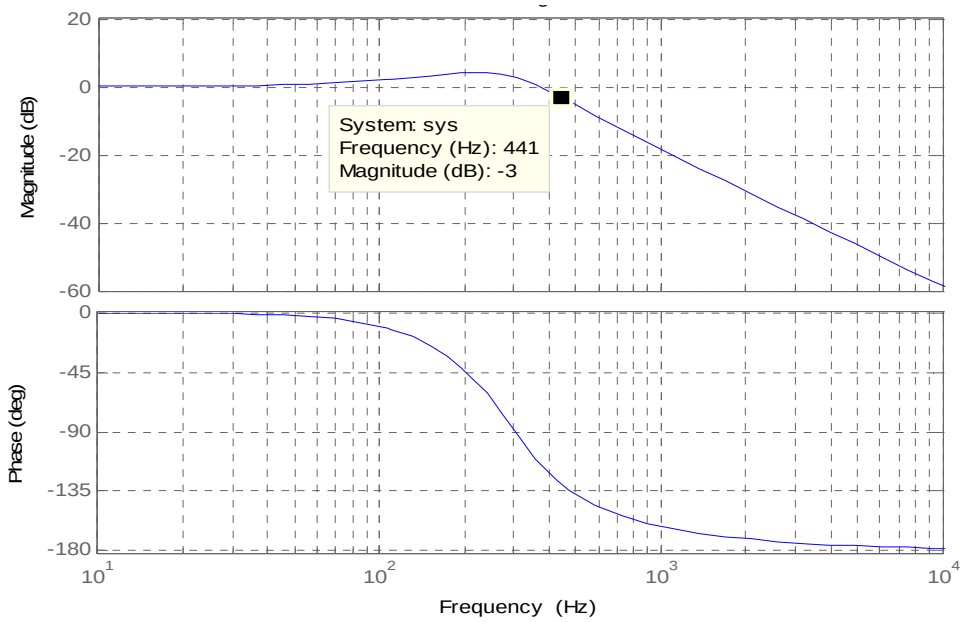

Figure 38: Bode diagram of closed-loop system.

In this section, a detailed DC voltage loop design method was introduced. The outer voltage loop has adopted a PI controller since the voltage is constant. The phase margin showed in the Bode plots is 44.4 degree which indicates the stability of the voltage-loop controller. The voltage loop was designed to have a bandwidth of 441Hz which is smaller than the inner current loop to provide a stable capacitor voltage.

This chapter mainly discussed the grid side inverter and the LCL filter. A detailed design procedure was developed. Using the designed LCL filter and the controllers for current loop, when the grid impedance is changing, the phase margins of the control system change from 48.1 degree to 70.1 degree which indicate a stable control system. And to design the inner current loop and outer voltage loop separately, a faster inner loop with a bandwidth of 1,290Hz and a slower outer loop with a bandwidth of 441Hz were adopted. Next chapter will discuss the simulation of the overall wind power generation system to verify that the system works well and provides power to the grid.

CHAPTER FOUR

System Simulation and Discussions

System Simulation Environment

The system is simulated using MATLAB/Simulink, with all components selected from the Simulink. The system consists of the grid, LCL filter, grid side PWM inverter, DC capacitor link, DC/DC boost converter, generator side diode rectifier, synchronous generator and wind power input. The model is shown in the Appendix A.

The devices of the grid-side inverter are IGBT plus Diodes. The parameters of the generator are: The nominal power is 250kW, the nominal frequency is 60Hz, the inertial coefficient is 0.62, the pole pairs is 12. The rated wind speed of this wind power system is 13m/s which produces the rated 250kW power to the grid. A natural wind speed profile is used, thus the wind is not constant and is changing all the time, usually consists of a basic wind, a gust and a random noise wind. Fig. 39 is the wind profile used in the simulation after combining the three elements of the wind. Fig. 40 (a) is the active power output waveform, (b) is the generator torque and (c) is the generator rotor speed. When the wind speed is changing, the active power output, generator torque and generator rotor speed are also changing accordingly, while the reactive power is kept about zero since the reactive power reference is set to zero. Thus, the wind system decouples the active and reactive power output successfully and the power output can be controlled independently. Fig. 41 shows the profile of the tip speed ratio and Fig. 42 shows the profile of power coefficient C_p. When the wind speed is changing, the

generator control system adjusts the rotor speed to make the tip speed ratio and power coefficient C_p stable to extract the maximum power from the wind using MPPT algorithm.

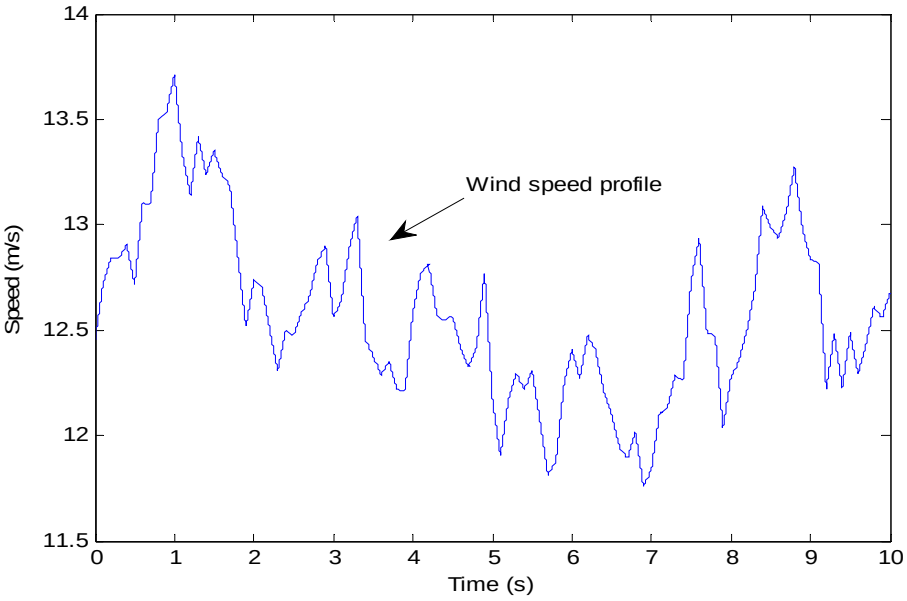

Figure 39: Wind speed profile.

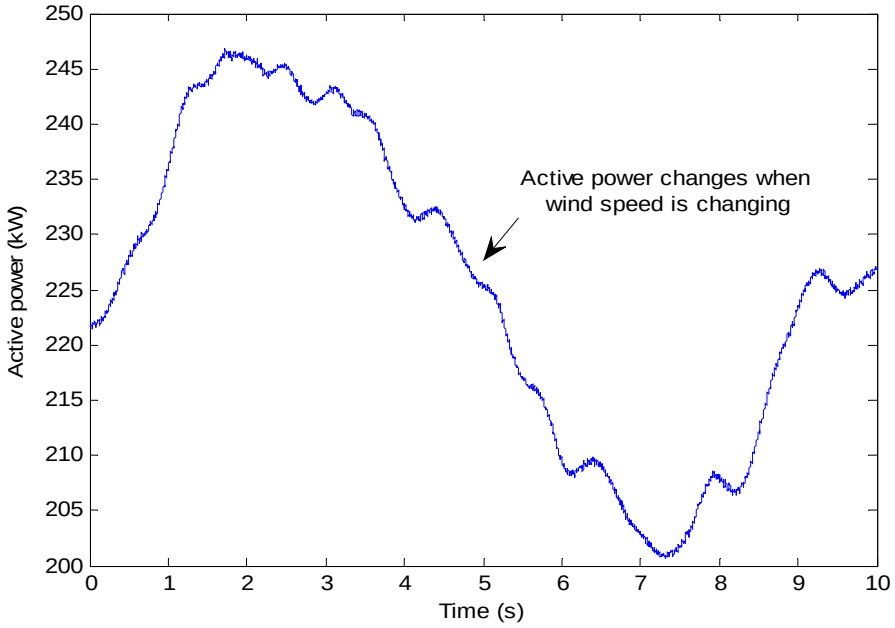

(a) Active power output.

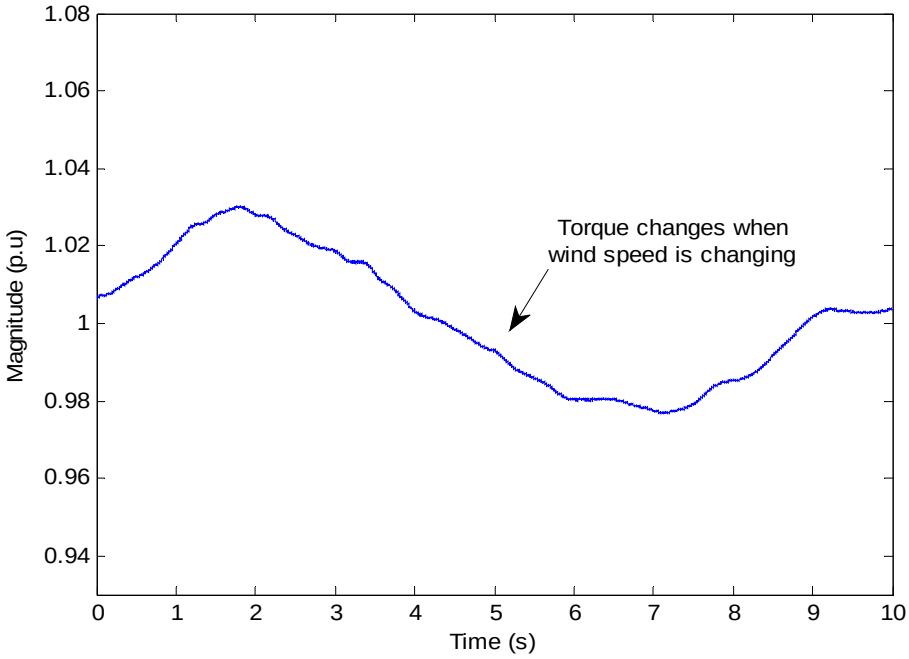

(b) Generator torque.

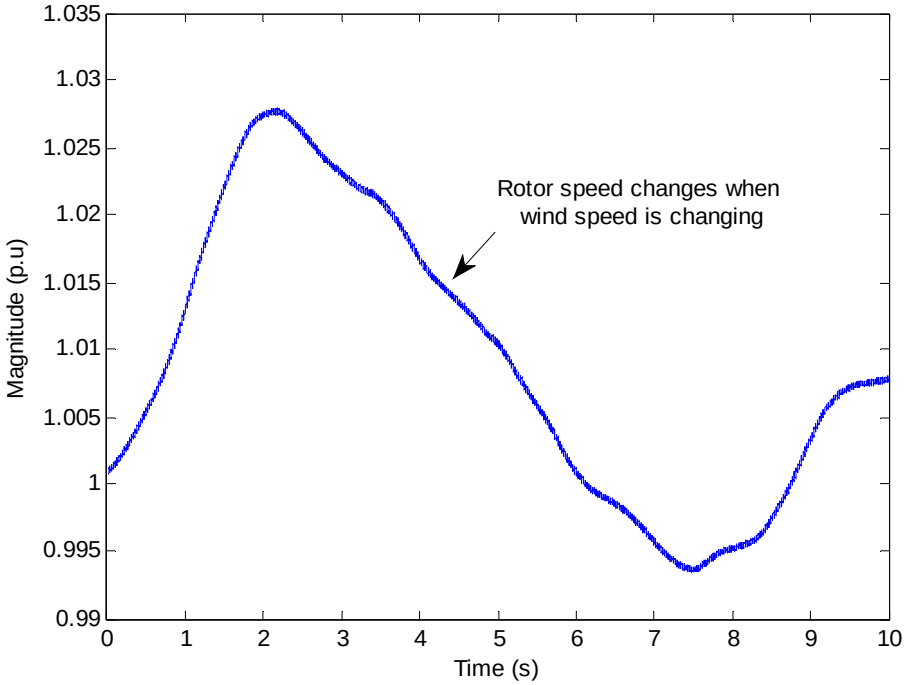

(c) Generator rotor speed.

Figure 40: Power output under various wind speed.

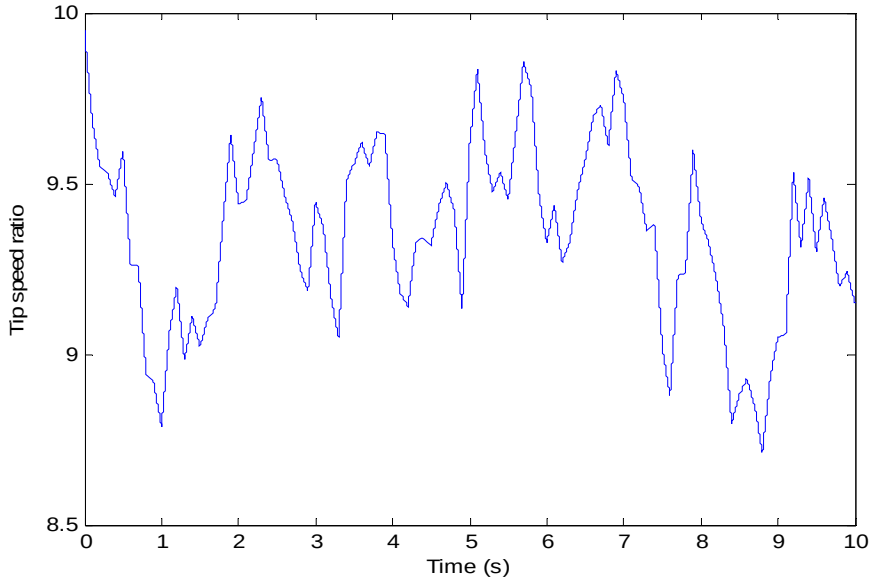

Figure 41: Tip speed ratio.

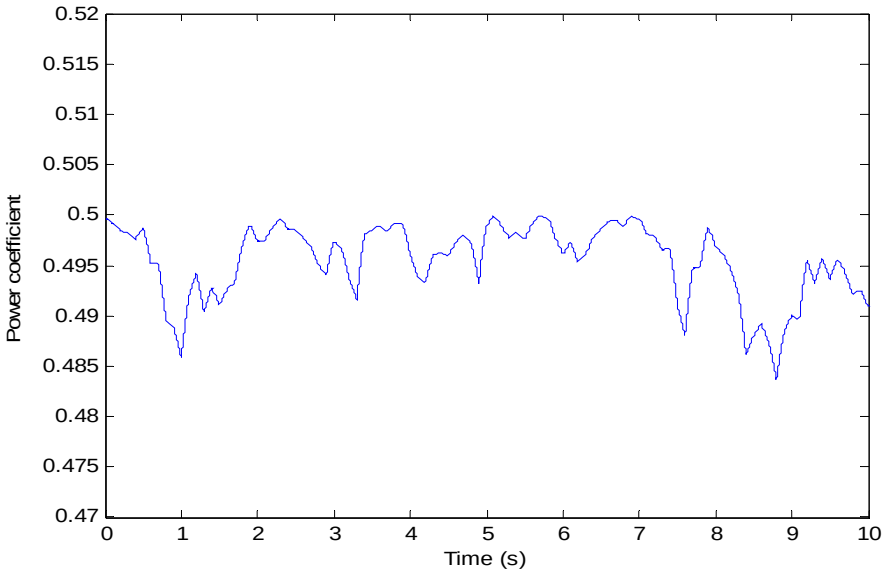

Figure 42: Power coefficient C_p.

Fig. 43 is the DC link capacitor voltage waveform, the inverter-side control scheme successfully kept the DC voltage to be 600v. Fig. 44 shows the waveforms of the reference current and actual current in αβ frame. The actual current exactly tracked the

reference current. The largest error occurred at the top and the bottom of the sine wave and the error is less than 0.1%.

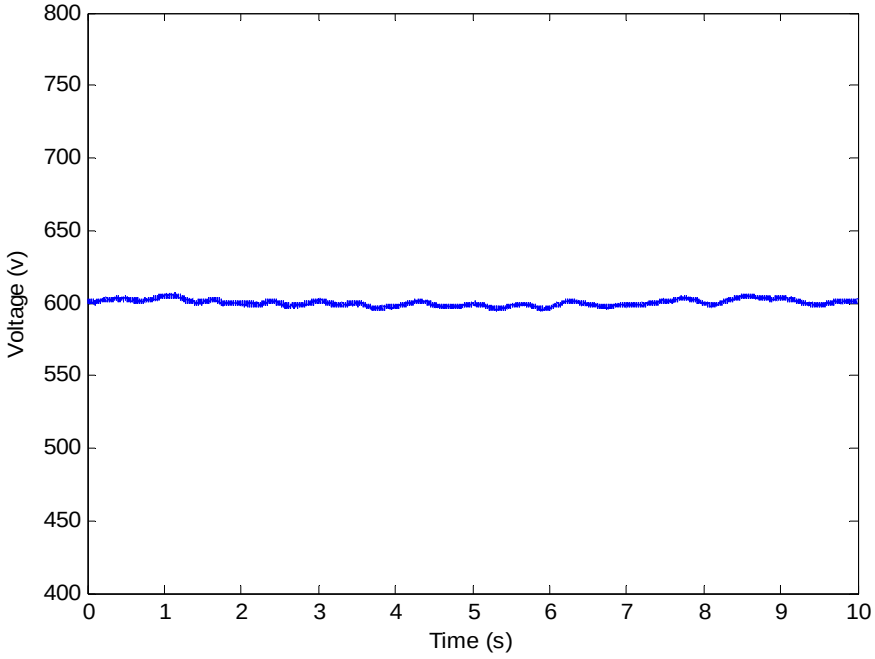

Figure 43: DC capacitor link voltage.

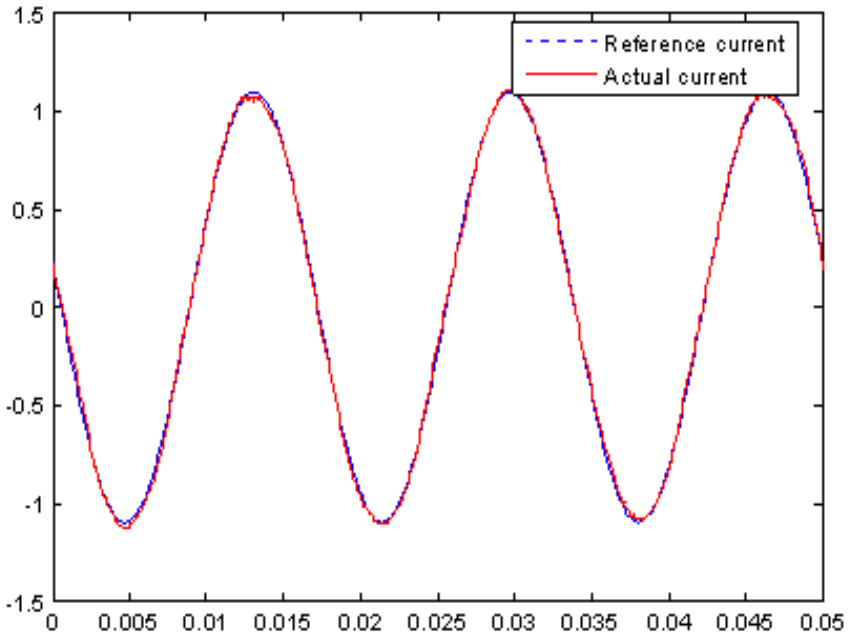

(a) α frame.

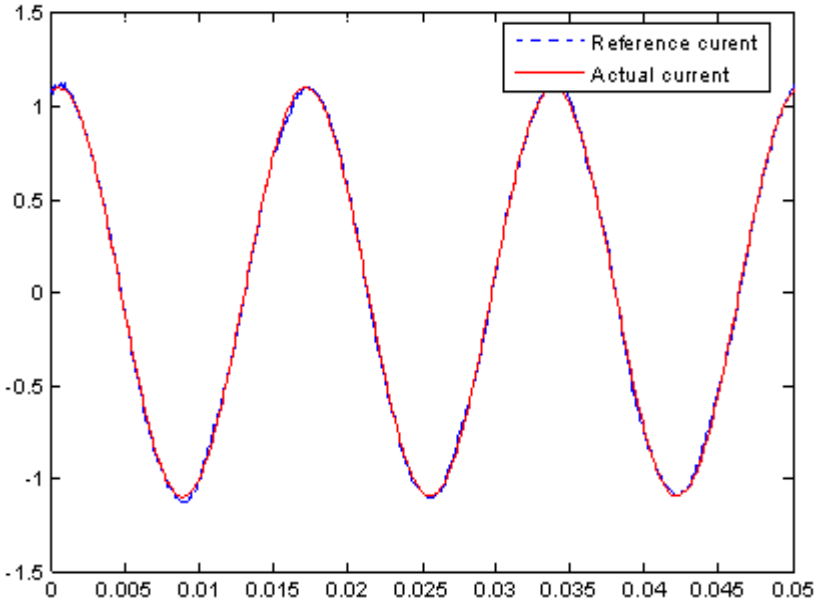

(b) β frame.

Figure 44: Waveforms of reference current and actual current in α, β frame.

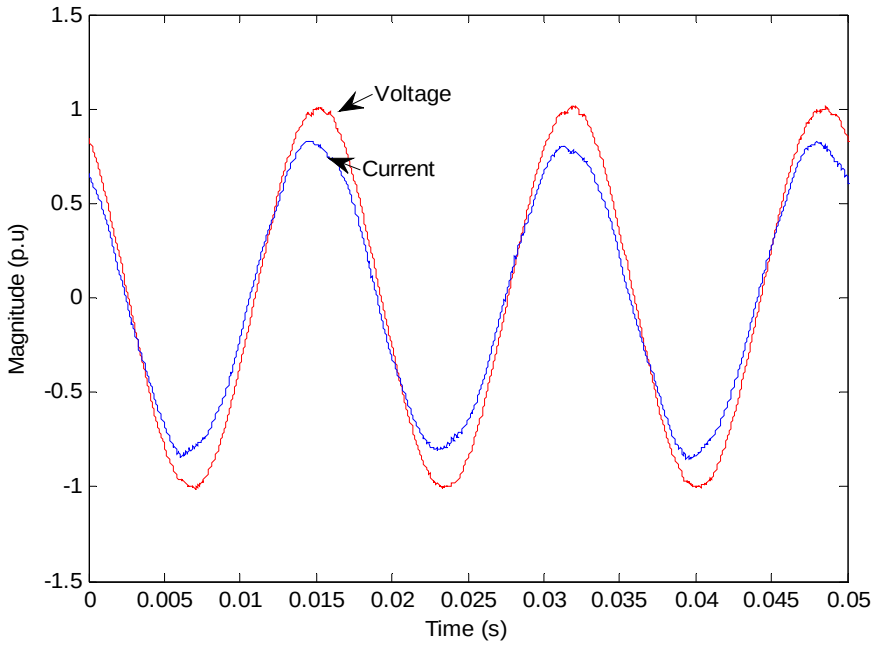

(a) Voltage and current are in phase.

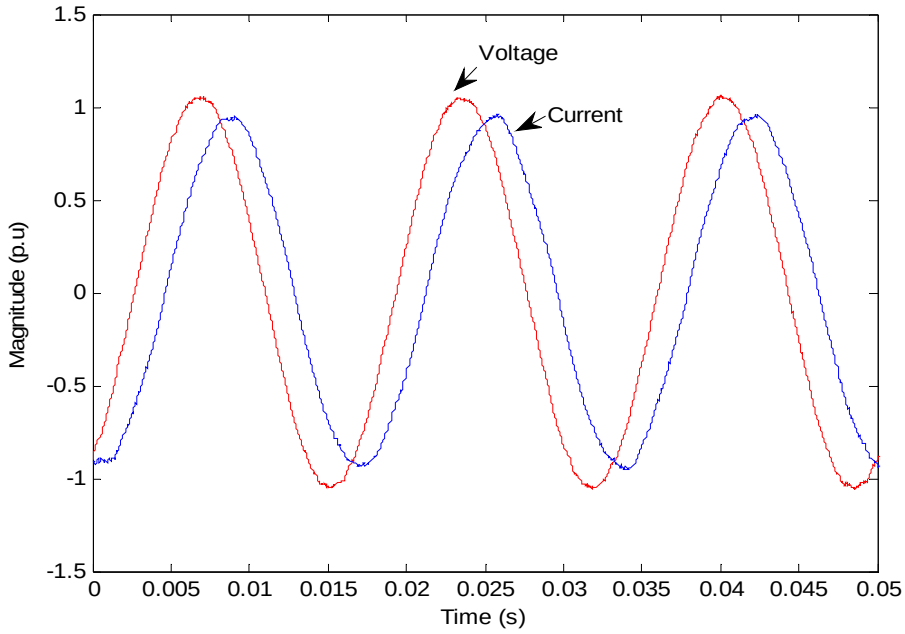

(b) Voltage and current are not in phase.

Figure 45: Waveforms of the grid voltage and current.

Fig. 45 (a) shows the waveforms of the grid voltage and grid current. The grid voltage is assumed to have a constant voltage amplitude and frequency. The voltage and current are in phase since the reactive output reference is set to be zero and the power factor is almost 0.99. Fig. 45 (b) shows that the voltage and current are not in phase.

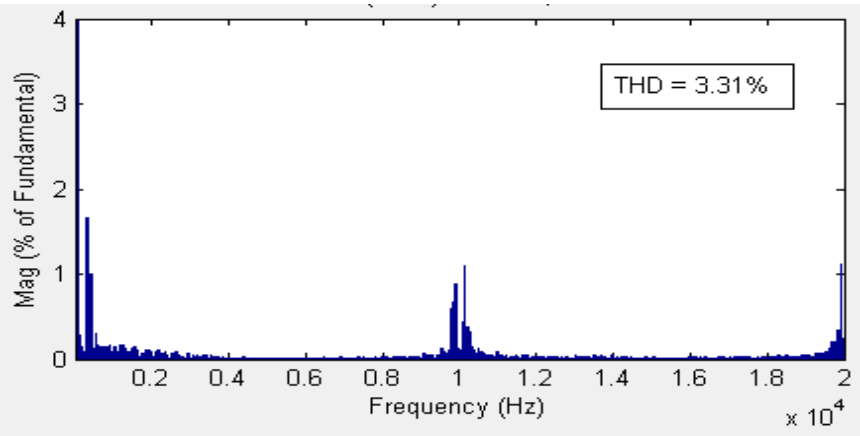

(a) Inverter-side current THD=3.31%.

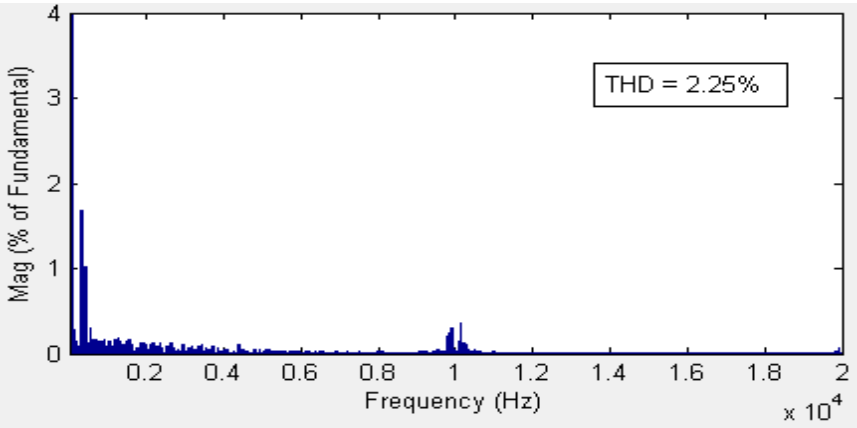

(b) Grid-side current THD=2.25%.

Figure 46: THD plots of inverter side current and grid side current.

Fig. 46 is the total harmonics distortion (THD) analysis of the inverter-side current and the grid-side current. At the switching frequency (3kHz), the magnitude of the harmonics decreased to 0.3% (grid-side) from 1% (inverter-side), and the THD decreased to 2.25% from 3.31% which indicate the effectiveness of the LCL filter.

In this section, a simulation of the overall wind power generation system was conducted. From the simulation results, we can see that when the wind speed is changing, the system tracked the wind speed profile to produce the maximum power to the grid under various wind speed and it kept the DC voltage of the capacitor link stable. Furthermore, the LCL filter effectively reduced the harmonics of the grid current at the switching frequency from 3.31% to 2.25%. The simulation results are what we expected from the theory.

Voltage Transient Analysis and Simulation

Why Voltage Transient Analysis Necessary

In a normal situation, the grid voltage can be regarded as a voltage which has constant magnitude and constant frequency (60Hz). In previous section, a controller was discussed in detail for this situation, and simulation results have shown the effectiveness of the controller. But in other situations, the grid voltage may not remain stable. These situations are called "voltage sag" as defined by IEEE Standard 1159 [38], "IEEE Recommended Practice for Monitoring Electric Power Quality." Voltage sag is "a decrease in RMS voltage or current at the power frequency for durations from 0.5 cycles to 1 minute, reported as the remaining voltage." Typical values are between 0.1 p.u to 0.9 p.u. A voltage sag is stated as a percentage of the nominal voltage. Thus a voltage sag of 60% is equivalent to 60% of nominal voltage, or 288 Volts for a nominal 480 Volt system. Typical sag clearing times range from three to thirty cycles depending on the fault current magnitude and the type of overcurrent detection and interruption. Another definition, as given in IEEE Std. 1159, 3.1.73, is **"**A variation of the RMS value of the voltage from nominal voltage for a time greater than 0.5 cycles of the power frequency but less than or equal to 1 minute. Most voltage sags do not go below 50 percent of the nominal voltage, and they normally last from 3 to 10 cycles.

Voltage sags can occur on utility systems both at transmission voltages and distribution voltages. Voltage sags which occur at higher voltages will normally spread through a utility system and will be transmitted to lower voltage systems via transformers. And voltage sags can also be created within an industrial complex without any influence

from the utility system. These sags are typically caused by starting large motors or by electrical faults inside the facility.

There are several causes of voltage sags within the utility system. If a substation circuit breaker or a recloser is tripped, then the line which it is feeding will be temporarily disconnected. All other feeder lines from the same substation system will see this disconnection event as a voltage sag which will spread to consumers on these other lines. The depth of the voltage sag at the consumer's site will vary depending on the supply line voltage and the distance from the fault. Typically a higher supply voltage will have a larger sag affected zone. If electrical equipment fails due to overloading or cable faults, then protective equipment will begin operating at the substation and voltage sags will be seen on other feeder lines across the utility system.

Voltage sags can cause thermal damage to a device, such as over-current at the point of grid-connection. Bus and windings can also suffer mechanical damage due to high magnetic forces during faults, and voltage sags can increase the grid current. If the sag is severe, over-current will be transferred into the WPGS and the DC capacitor link. The voltage on the link can increase significantly and cause damage to the DC capacitor. Thus, voltage transient analysis is necessary to design the protection method for the wind power generation system.

Types of Voltage Faults

There are usually two types of voltage fault: balanced faults and unbalanced faults. A balanced fault voltage has an equal magnitude in all phases and a phase shift of 120º between the phases. An unbalanced fault voltage doesn't have the same magnitude in all phases or a phase shift of 120° between the phases, and these types are more

complicated. Unbalanced faults happen when the amplitude of one or two phase voltages drop. This section will analyze the influence of the voltage fault to a wind power generation system.

Case One: Balanced voltage sags [40]. Symmetrical three-phase sags account for less than 20% of all sag events and are caused either by switching or tripping of a three-phase circuit breaker, switch or recloser, which will create a three-phase voltage sag on other lines fed from the same substation. Fig. 47 (a) shows the balanced voltage fault where the grid voltage drops from 1 p.u to 0.8 p.u. for 10 cycles (166.7ms), (b) shows the grid voltage drops from 1 p.u. to 0.1 p.u. for 10 cycles. The faults happen at 0.05s and recover after 166.7ms.

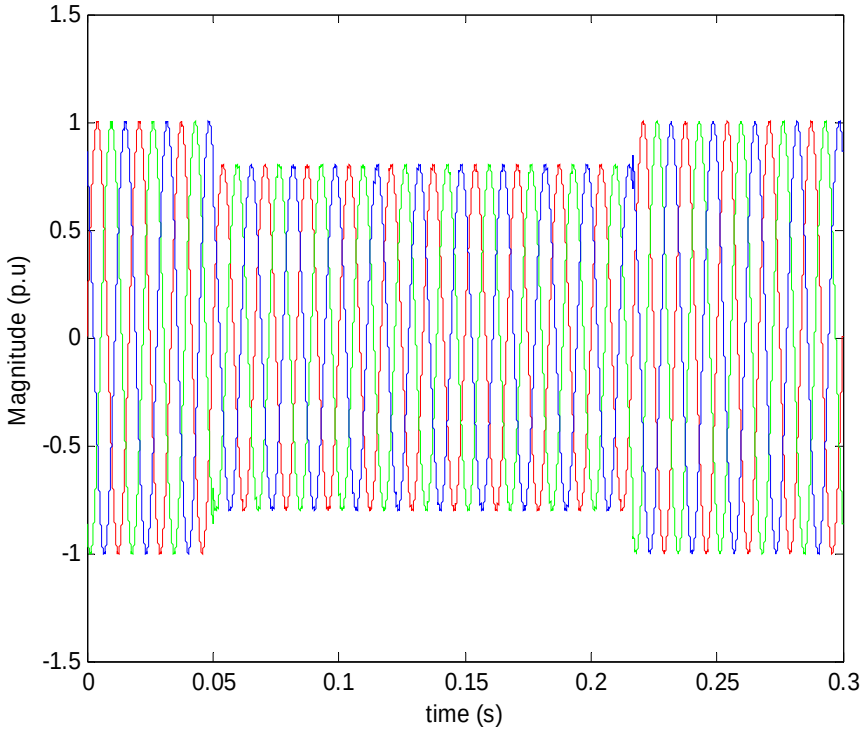

(a) Voltage drop from 1 p.u. to 0.8 p.u. for 166.7ms.

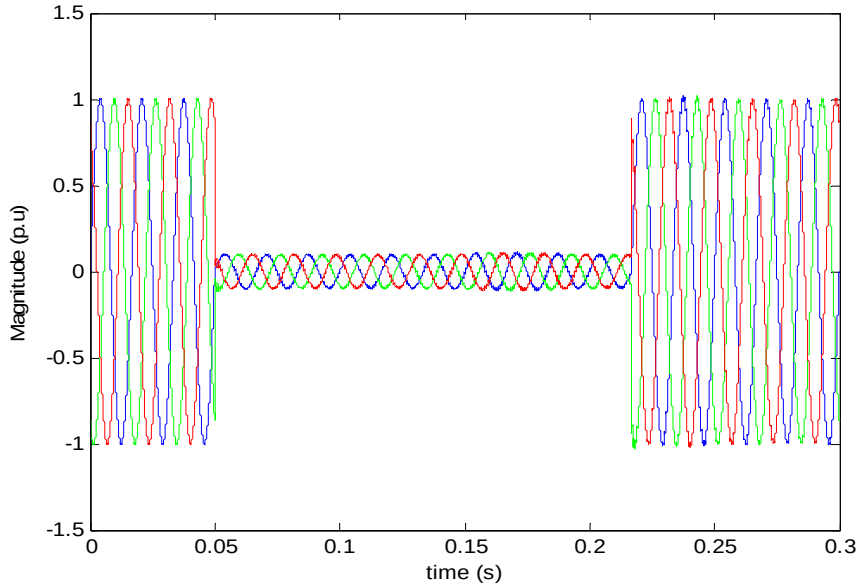

(b) Voltage drop from 1 p.u. to 0.1 p.u for 166.7 ms.

Figure 47: Balanced voltage faults for 166.7 ms.

Fig. 48 shows the waveform of the inner current loop current reference and actual current during the voltage fault from 1 p.u. to 0.8 p.u. (a) shows the waveforms of current in an α-frame, and (b) shows the waveforms of current in a β-frame.

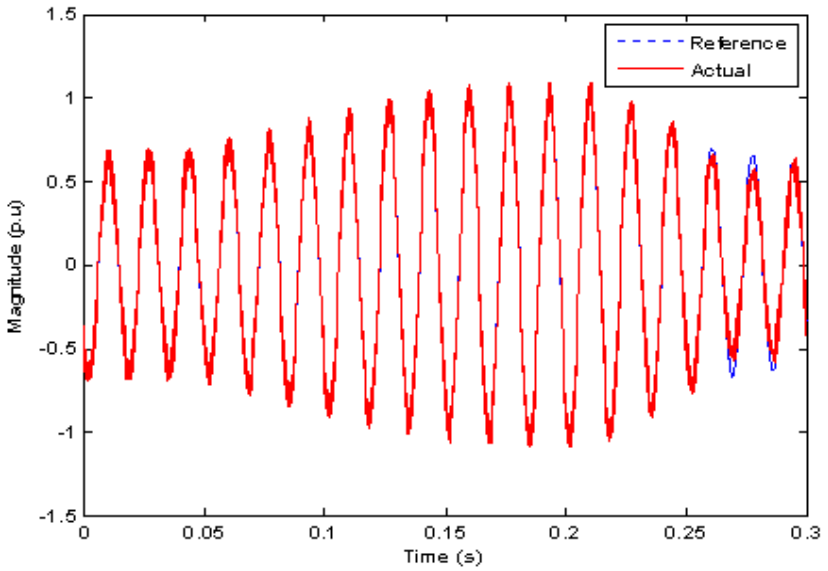

(a) Waveform of the reference current and actual current in α-frame.

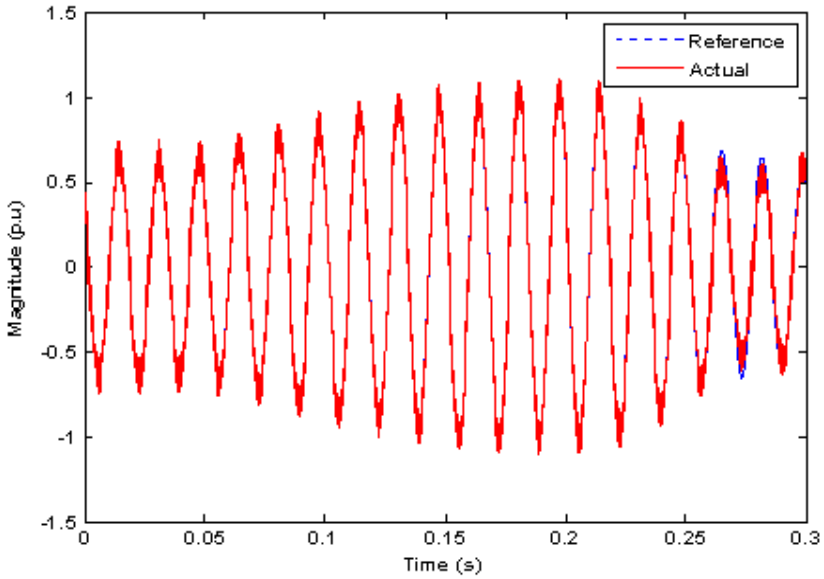

(b) Waveform of the reference current and actual current in β-frame.

Figure 48: Waveforms of the current during voltage faults.

Fig. 49 shows the generator rotor speed during the voltage fault drop from 1 p.u. to 0.8 p.u. Fig. 50 shows the output active power during the voltage fault with voltage drop from 1 p.u. to 0.8 p.u.

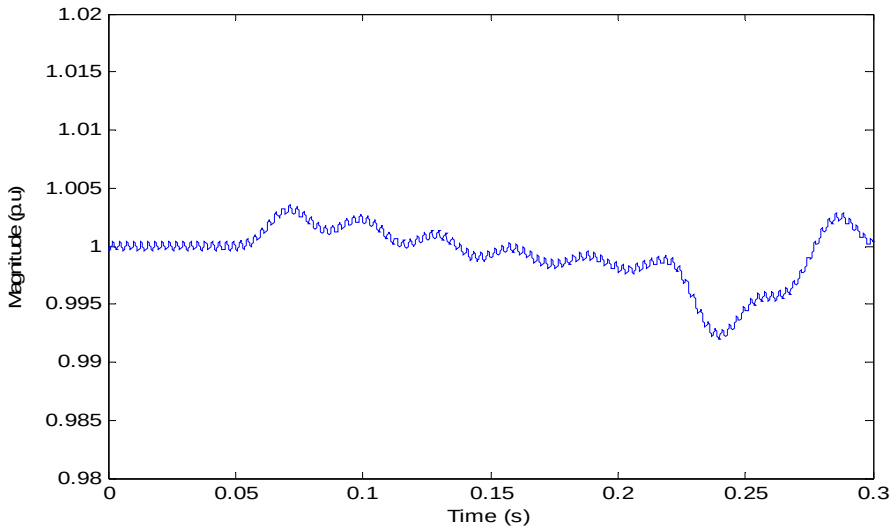

Figure 49: Generator rotor speed during voltage faults.

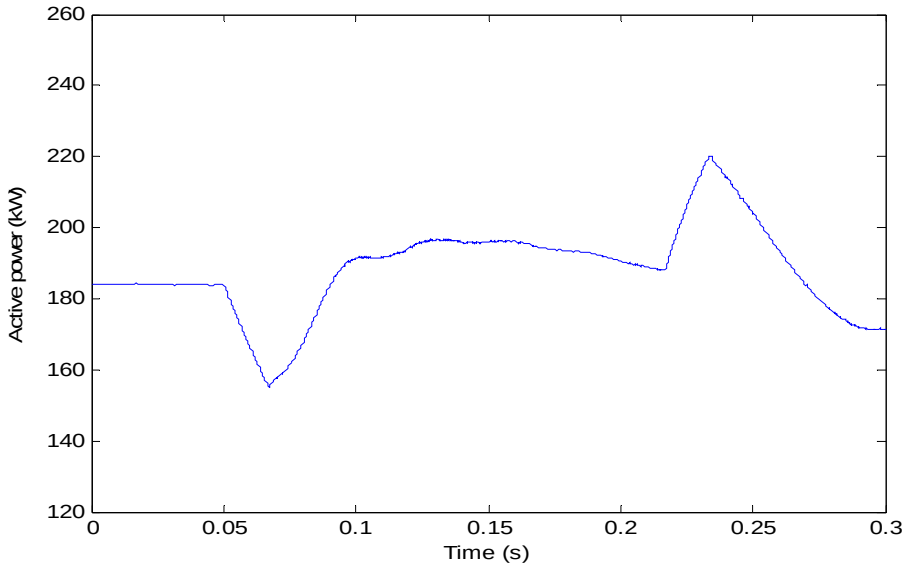

Figure 50: Active power output during voltage faults.

Fig. 51 shows the waveform of the grid current during the voltage fault with voltage drop from 1 p.u. to 0.8 p.u.

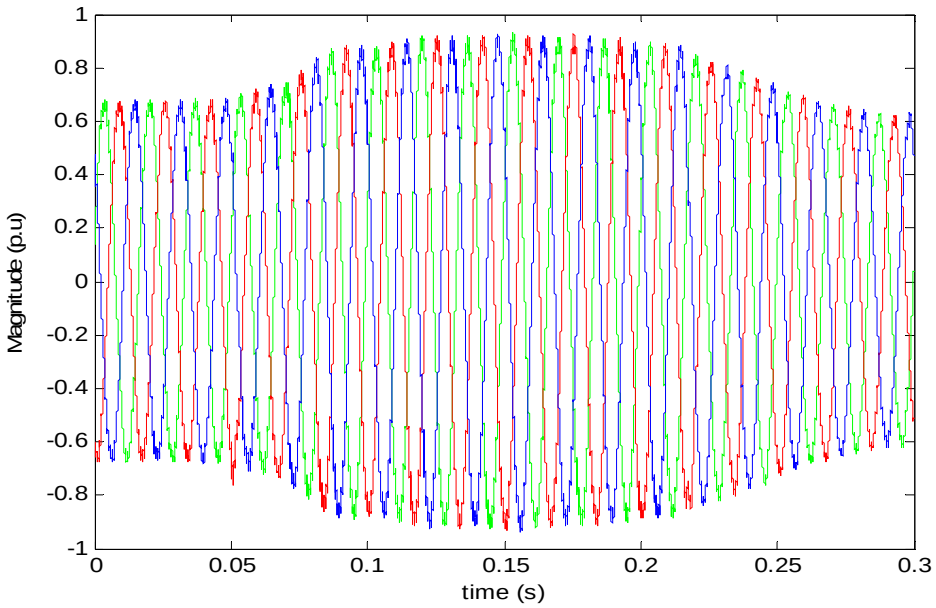

Figure 51: Grid current during balanced voltage faults.

From the above figures, during the grid voltage drops from 1 p.u. to 0.8 p.u, the output active power decreased because of the voltage drop. Since the active power

extracted from the wind doesn't change, both the inner loop current references increased to make the output active power equal to the input power from the wind. The three-phase gird current increased according to the increase of the current in the $\alpha\,\beta$-frame. And the voltage faults also make the generator rotor speed increase slightly. If the generator-side rotor speed controller was working at MPPT mode, and the wind speed did not change, the power extracted from the wind was still the same. And the output active power of the wind power system reduced due to the grid voltage sags. Since the voltage dropped from 1 p.u. to 0.8 p.u., the output active power dropped to 150kW, increasing the grid current by about 0.2 p.u. made the system run in a normal operation. During this kind of voltage faults, the controller recovered the active power output after the voltage sags occurred and the wind power generation system did not need any other protection methods.

Fig. 52 shows the waveform of the inner current loop current reference and actual current during the voltage fault with voltage drop from 1 p.u. to 0.1 p.u. (a) shows the waveforms of current in α-frame, and (b) shows the waveforms of current in β-frame.

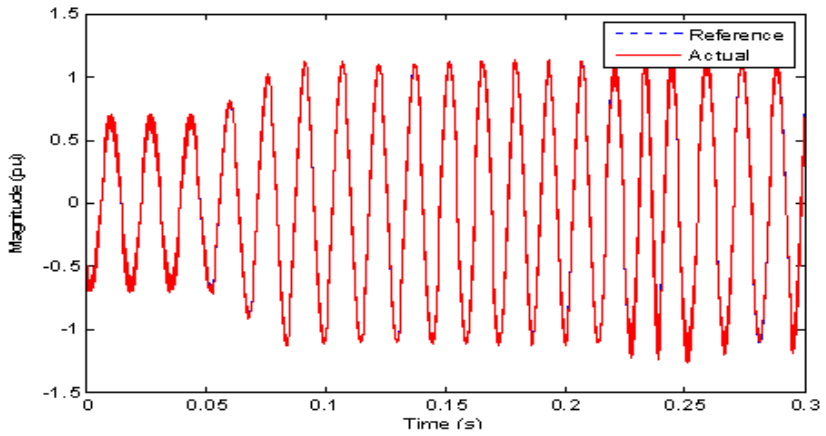

(a) Waveform of the reference current and actual current in α-frame.

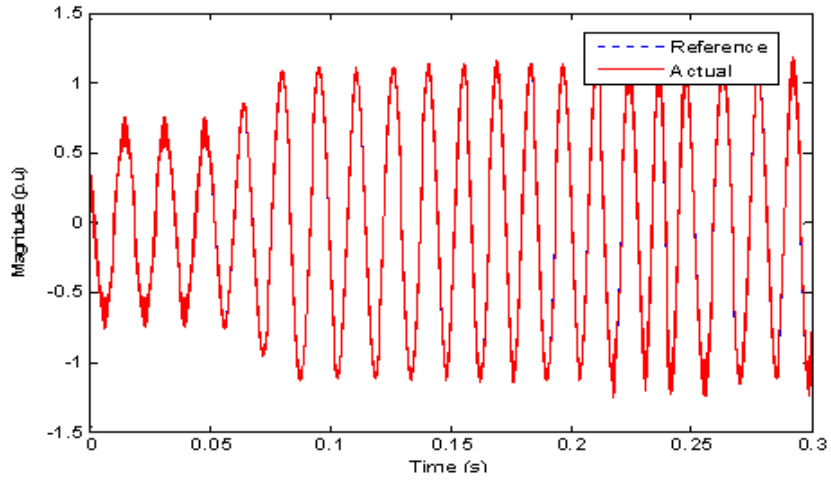

(b) Waveform of the reference current and actual current in β frame.

Figure 52: Waveforms of the inner loop current during voltage drops to 0.1 p.u.

Fig. 53 shows the generator rotor speed during the voltage faults drop from 1 p.u to 0.1 p.u. Fig. 54 is the output active power of the wind power generation system.

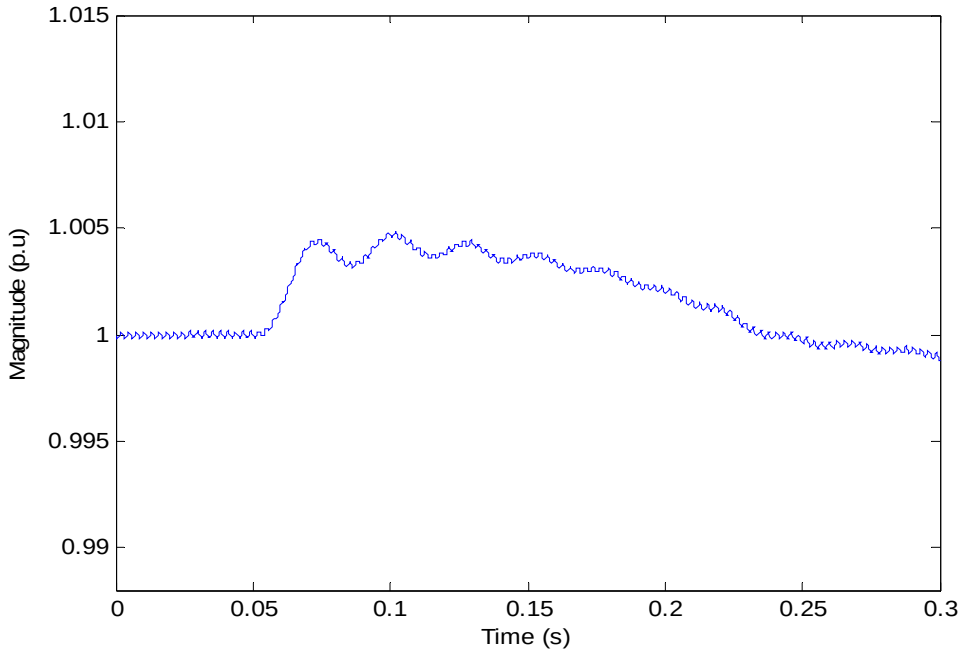

Figure 53: Generator rotor speed during the voltage fault with voltage drop from 1p.u. to 0.1 p.u.

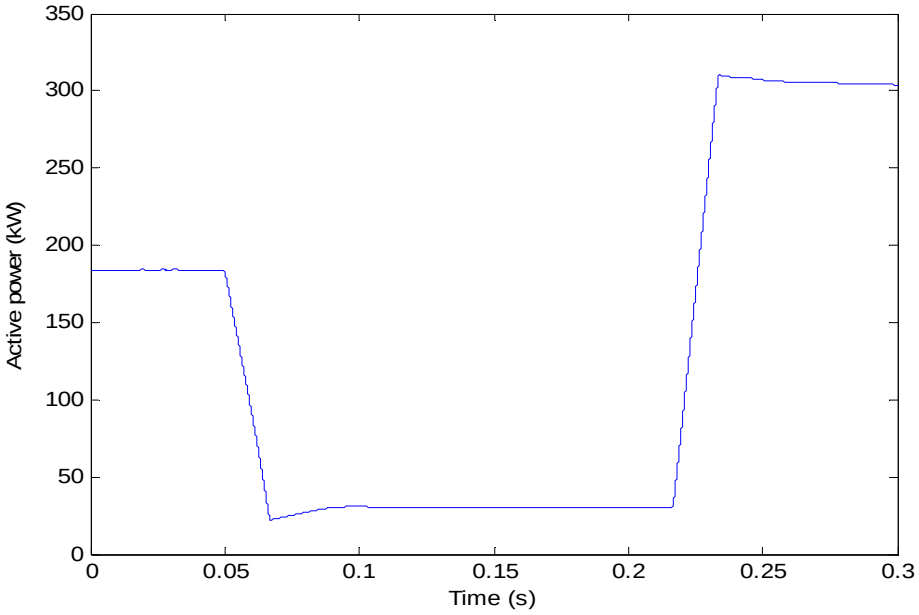

Figure 54: Active power during voltage faults.

Fig. 55 shows the grid current during voltage fault with voltage drop from 1 p.u. to 0.1p.u.

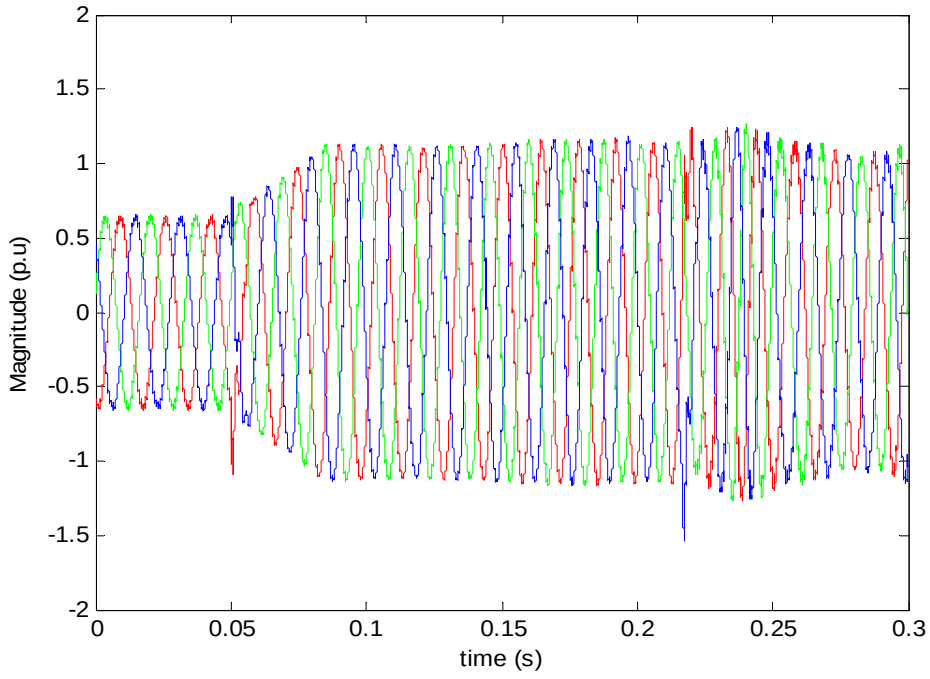

Figure 55: Grid current during voltage faults.

Comparing the figures from Fig. 52 to Fig. 55 with figures from Fig. 48 to Fig. 51, when the voltage drops from 1.0 p.u. to 0.1 p.u. The output active power decreased to 20kW. And also the inner loop current references increased by about 0.4 p.u. to make the output active power equal to the input power from the wind. The three-phase grid current increased by about 0.6 p.u. according to the increase of the current in the α β-frame. Since the mechanical torque is larger than electrical torque during the voltage fault, the generator rotor rotated faster. Consequently the power coefficient C_p which can reduce the power extracted from the wind is reduced. Because of the large inertia of the wind turbine, the rotor speed cannot be increased immediately, and the input power cannot be reduced so quickly to match the output active power during the voltage faults. The output power was reduced and quickly recovered during the voltage sag from 1 p.u. to 0.8 p.u. (Fig. 50), while when voltage sag was from 1 p.u. to 0.1 p.u., the output power was reduced, but was not recovered during the sag (Fig. 54). Thus, the difference between the input power and output power flowed into the DC capacitor link. During this kind of severe voltage faults, the controller cannot work effectively anymore and the wind power generation system needs other protection systems.

Case Two: Unbalanced sags. The most common voltage sags, over 70%, are single-phase events which are typically due to a phase-to-ground fault occurring somewhere in the system. This phase-to-ground fault appears as a single-phase voltage sag on other feeders from the same substation. Typical causes are lightning strikes, tree branches, animal contact, etc. It is not uncommon to see single-phase voltage sags to 30% of nominal voltage or even lower in industrial plants. Fig. 56 are the waveforms of

an unbalanced fault voltage. A single-phase voltage drops from 1 p.u. to 0.8 p.u. and 0.1 p.u., respectively. The faults happen at 0.5 second for 10 cycles.

Fig. 57 shows the waveforms of the inner loop reference current and actual current in the αβ-frame for the voltage sag from 1.0 p.u.to 0.8 p.u.

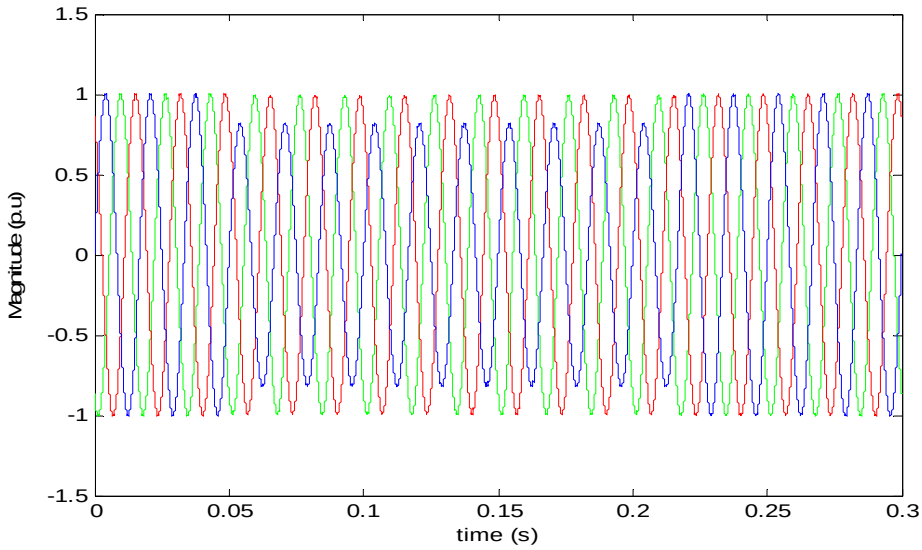

(a) Voltage drop from 1.0 p.u. to 0.8 p.u.

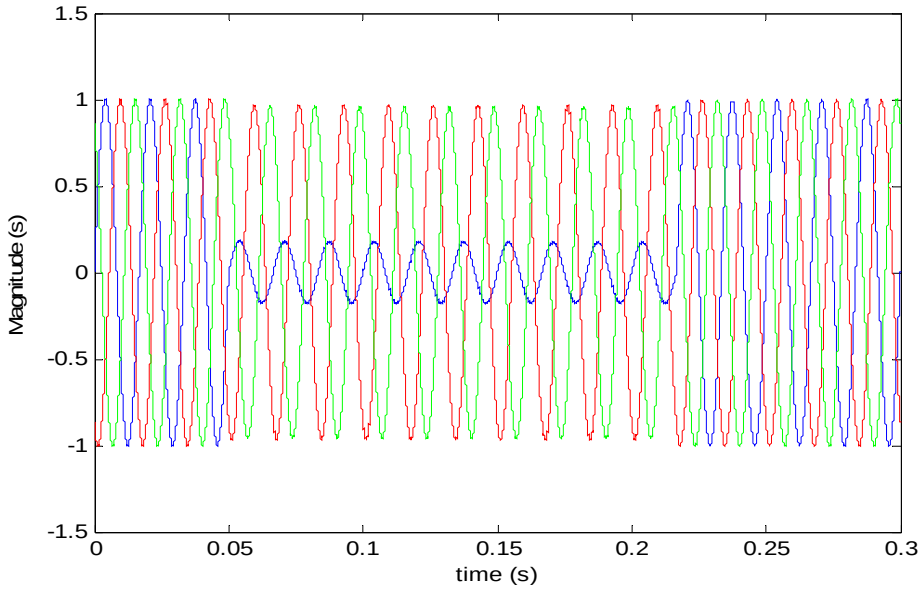

(b) Voltage drop from 1.0 p.u to 0.1 p.u.

Figure 56: Single phase voltage faults for 166.7ms.

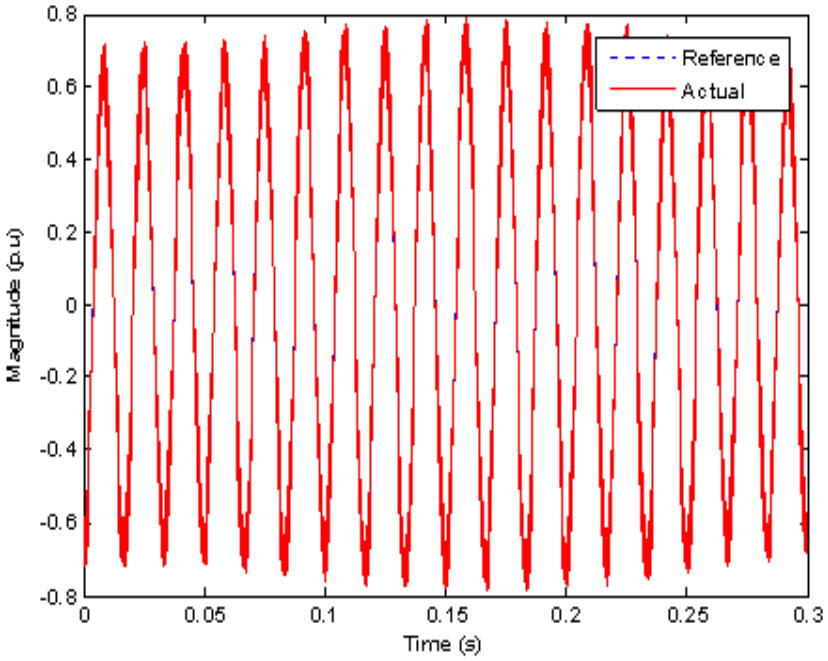

(a) Reference current and actual current in α-frame.

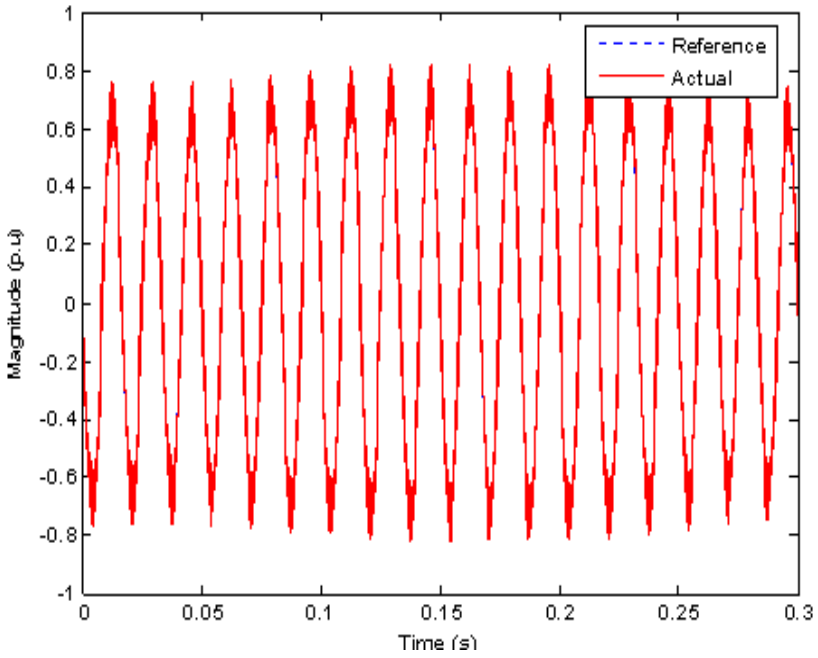

(b) Reference current and actual current in β-frame.

Figure 57: Reference current and actual current during voltage fault with voltage sag from 1.0 p.u. to 0.8 p.u.

Fig. 58 shows the generator rotor speed. Fig. 59 is the active power output of the wind power generation system. Fig. 60 is the three-phase grid current.

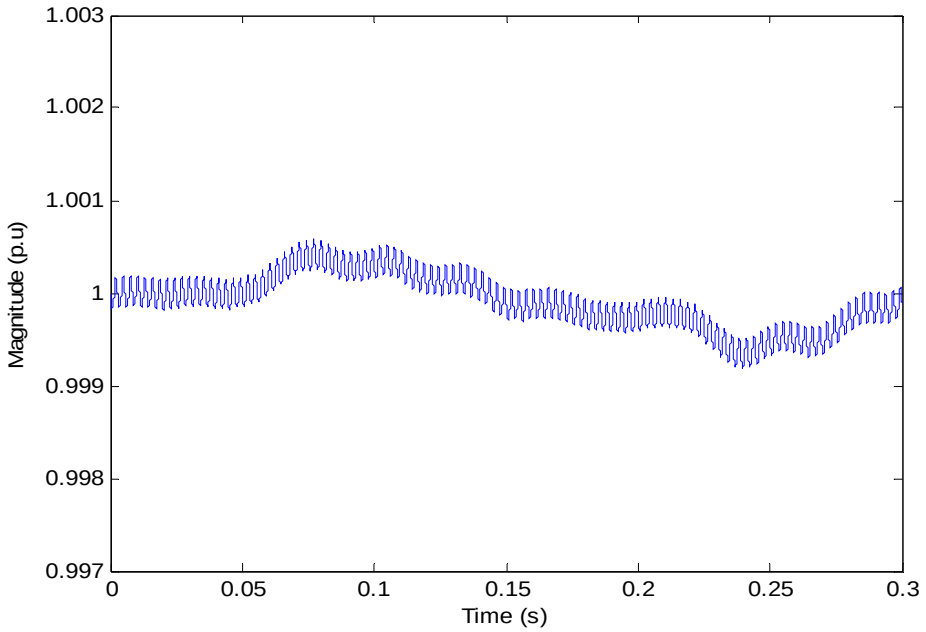

Figure 58: Generator rotor speed during voltage fault with voltage sag from 1.0 p.u. to 0.8 p.u.

.

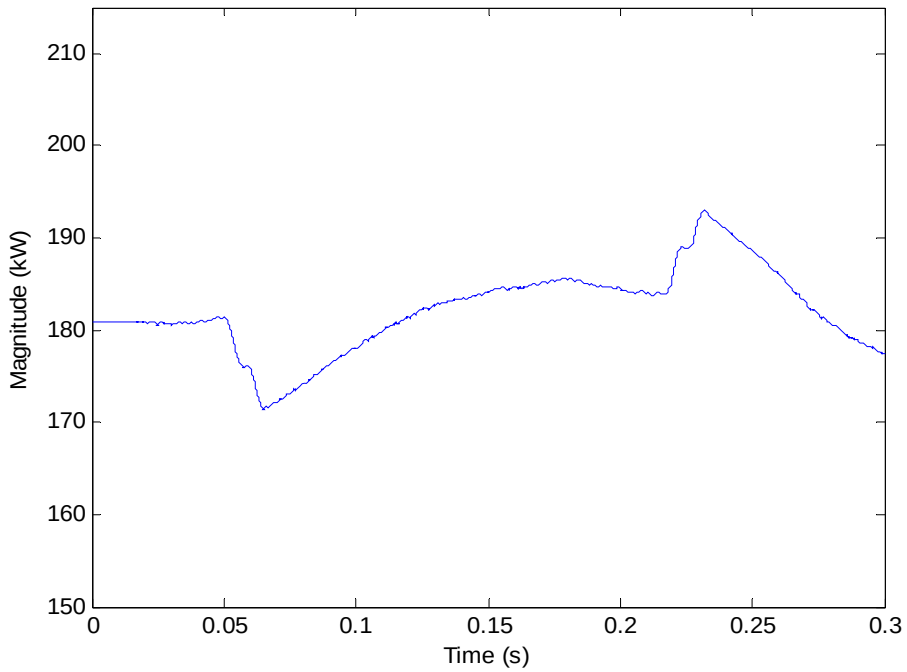

Figure 59: Active power output during voltage drop from 1 p.u. to 0.8 p.u.

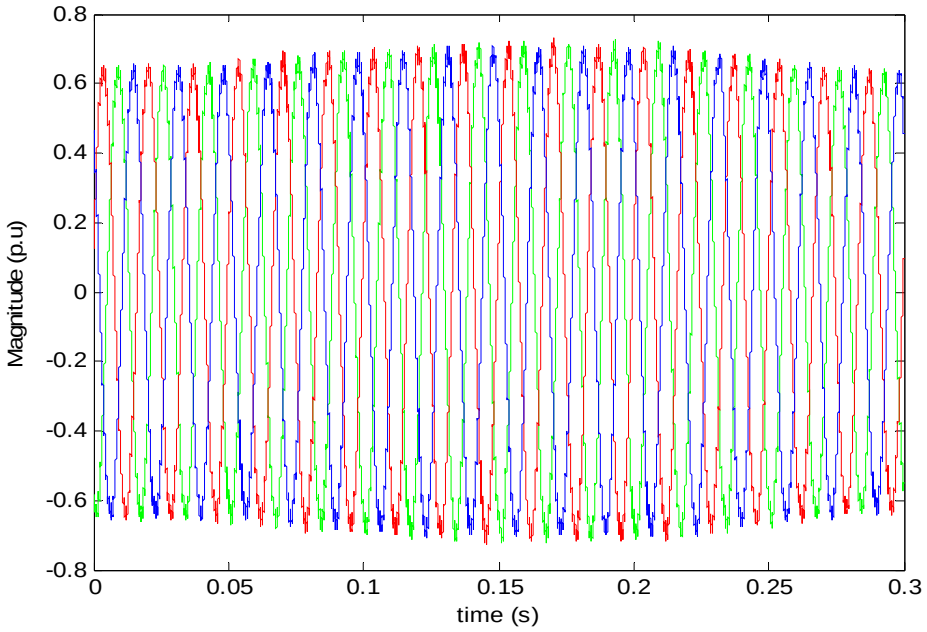

Figure 60: Grid current when voltage drops from 1 p.u to 0.8 p.u.

Under single-phase voltage sag, the reference currents in the αβ-frame increased slightly and as well as the generator side rotor speed because of only a slight sag of the voltage. And the active power output decreased when voltage faults happened and then increased to match the input power of the wind power generation system immediately after the voltage sag.

The grid current increased to compensate the sag of the voltage. Under this kind of faults, the controller of the wind power generation system worked effectively and the system was running at normal operation without any other protection system.

Fig. 61 shows the waveforms of the inner current loop current reference and actual current during the single-phase voltage faults from 1 p.u. to 0.1 p.u. (a) shows the waveforms of current in α-frame, and (b) shows the waveforms of current in β-frame. Fig. 62 shows the generator rotor speed and Fig. 63 is the active power output. Fig. 64 shows the grid current.

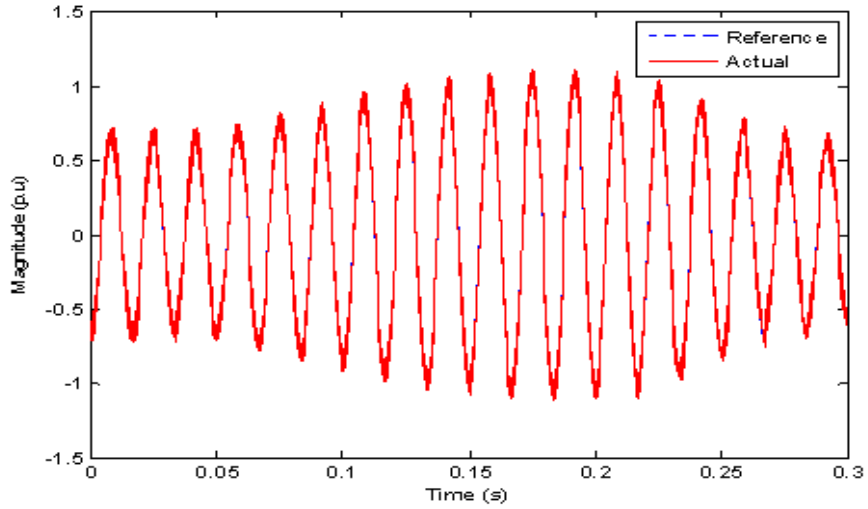

(a) Reference current and actual current in α frame.

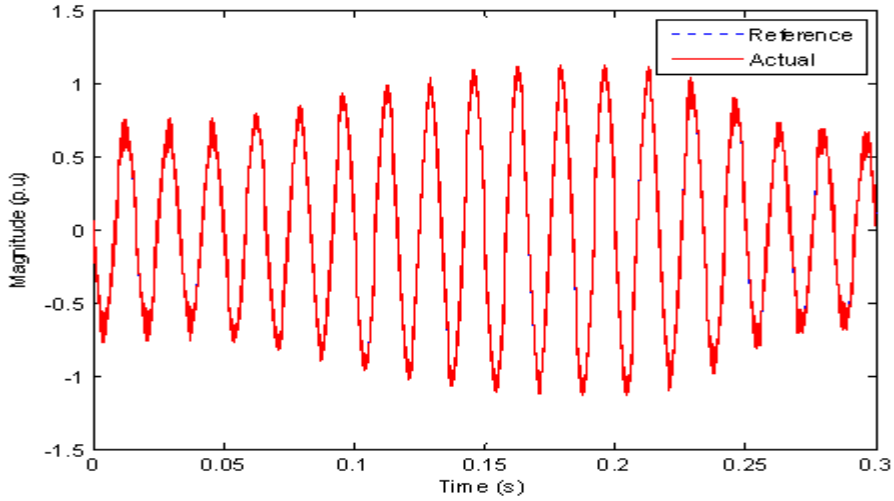

(b) Reference current and actual current in β frame.

Figure 61: Waveforms of the current loop current reference and actual current.

The changes of all the signals are similar with those under balanced voltage faults. The active power decreased much more than that under balanced voltage fault of 0.8 p.u.. Comparing all the figures above with figures when a single-phase voltage drops from 1.0 p.u to 0.8 p.u. both the inner loop current references increased more to make the output active power equal to the input power extracted from the wind. The three-phase grid current increased more according to the increase of the current in the αβ-frame. From the

analysis above, under some severe voltage fault condition, the system needs a protection system to protect the system from being damaged. Next section will discuss a way to keep the wind power generation system to operate without disconnecting from the grid.

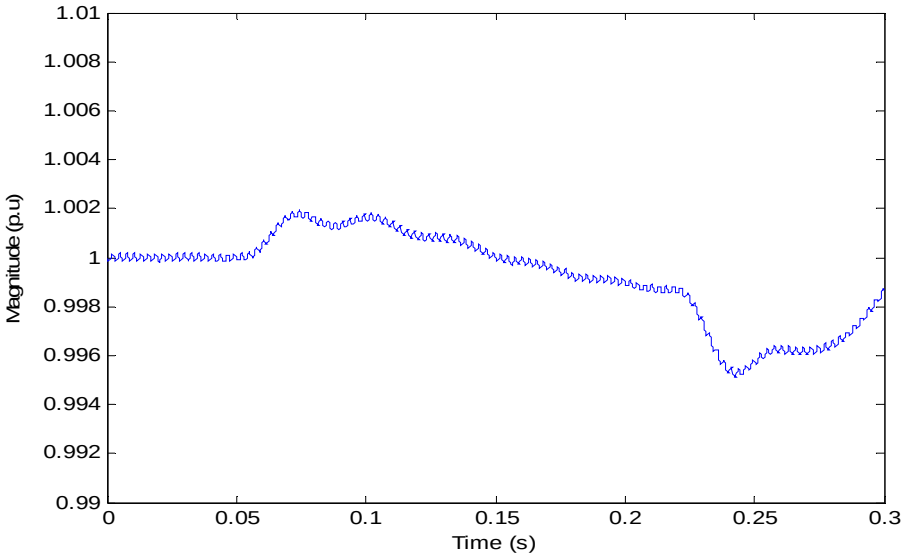

Figure 62: Generator rotor speed during voltage faults.

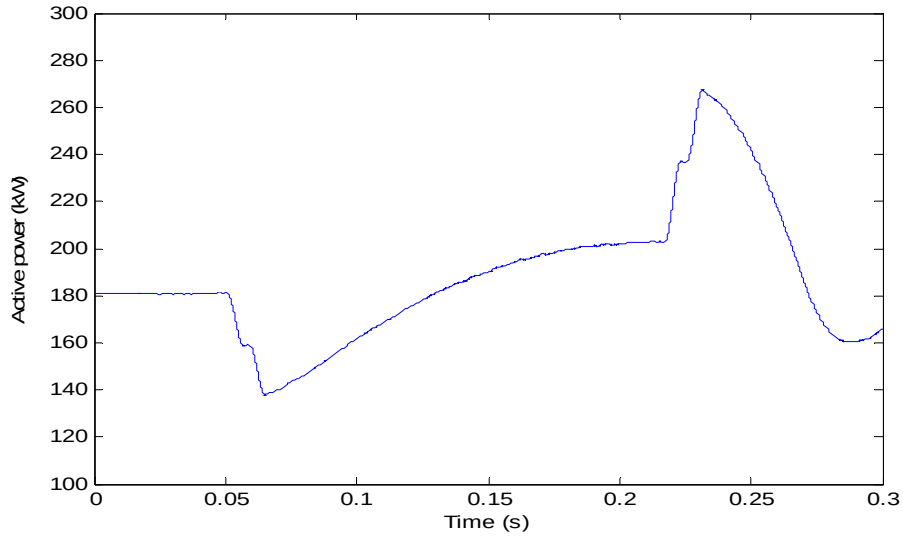

Figure 63: Active power output during voltage faults.

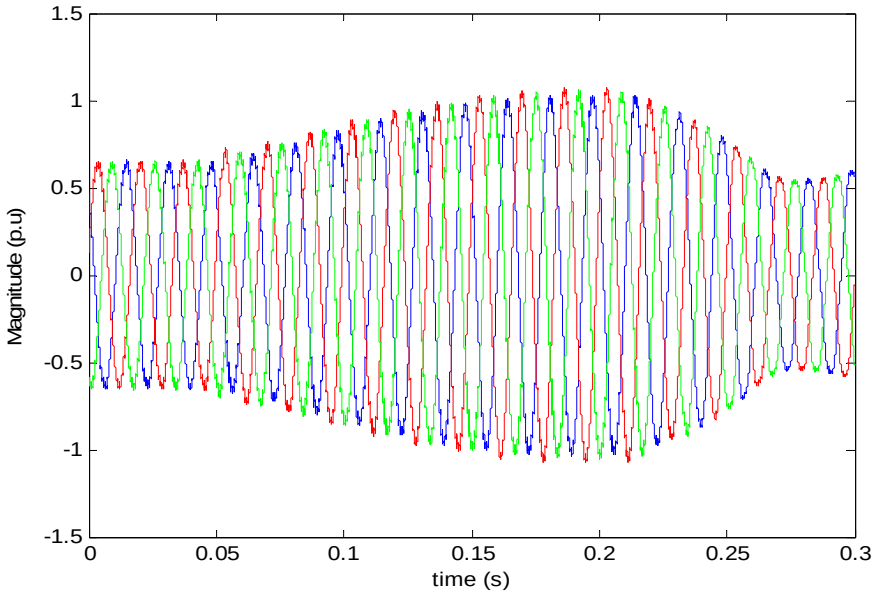

Figure 64: Grid current during unbalanced voltage faults.

Low-Voltage Ride-Through

In the past, wind power generation was only a small percentage of the total installed generating capacity. Wind turbines were allowed to be disconnected from the grid whenever the situation suited the wind turbine. However, today wind power has been increasing and consequently, disconnection of a significant percentage of generating capacity can have a profound effect on the stability of the grid. In the United States, the Federal Energy Regulatory Commission (FERC) proposed a low-voltage ride-through (LVRT) requirement, Large Generator Interconnection Agreement (LGIA), which was issued June 2, 2005 [41]. The new LVRT rule, applying to wind turbine facilities greater than 20 MW, specifies a depth of sag versus time envelope for which a wind turbine is expected to remain on-line as shown in Fig. 65 [42]. An applicable wind turbine generator is required to remain online during a low-voltage down to 15% of nominal voltage for up to 0.625 seconds (37.l5 cycles at 60 Hz). And other countries also

proposed similar rules. And the North American Electrical Reliability Council (NERC) together with the American Wind Energy Association (AWEA) have since proposed a change to the LVRT requirement of Order No. 661 to resolve differences with the existing NERC standard TPL-002-0 which dictates minimum system performance following a single grid fault. The proposed change would require generators to remain on-line for low-voltage conditions down to zero volts for a period not to exceed 9 cycles (150ms) [43]. This more severe requirement is indicated by the dashed line in Fig. 65.

The low voltage ride-through requires that the wind power generation system must stay connected to the grid during the voltage faults for a given time duration. From the previous section, during the voltage fault the grid current will increase, and if the grid current is too large, it will destroy the grid side inverter. Moreover, when the grid voltage drops, the active power transmitted to the grid also decreases, but the power extracted from the wind is still the same and the difference in power is transmitted to the DC capacitor bus continuously by the generator.

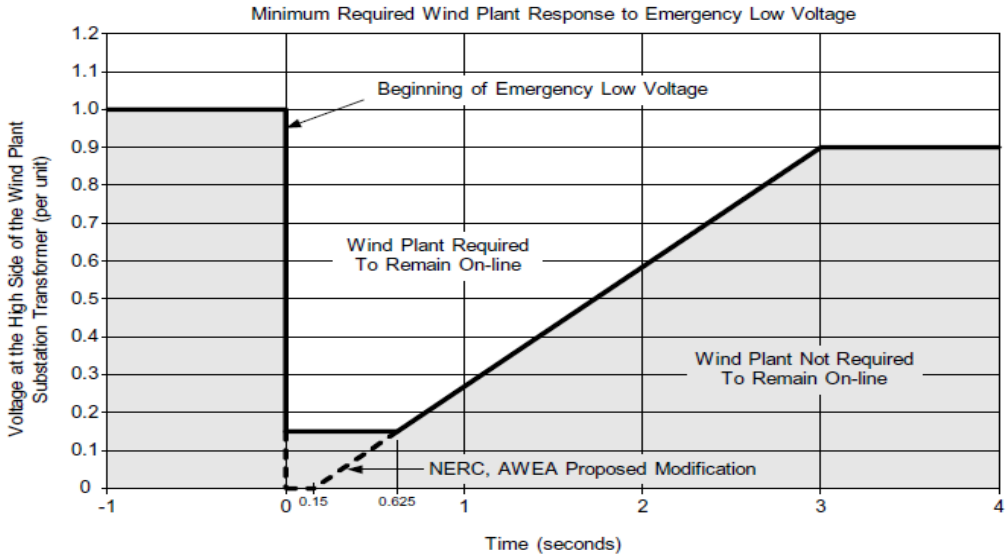

Figure 65: Low-Voltage Ride-Through requirement [43].

Fig. 66 shows the power produced from the generator and transmitted to the grid under normal operation and voltage drop operation, where the actual boost-converters consist of three boost converter. P_w is the power extracted from the wind and after passing through the rectifier it becomes P_g, and finally transmitted to the grid through the grid-side inverter. P_w equals to P_g and P_{inv} under normal voltage operation. Since the voltage of the DC capacitor does not change, all the power extracted from the wind is transmitted to the grid. While under a voltage fault condition, the power transmitted to the grid is reduced due to the voltage drop. Thus, P_{inv} is reduced and $P_g = P_c + P_{inv}$. Since P_g does not change, the power injected to the DC capacitor bus P_c will increase. The increased DC bus power will cause the increase of the voltage of DC capacitor. The large voltage of DC bus will damage the capacitor and converter.

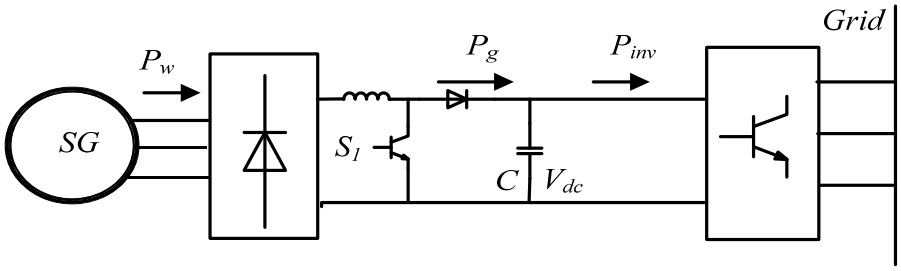

(a) Power flow under normal condition

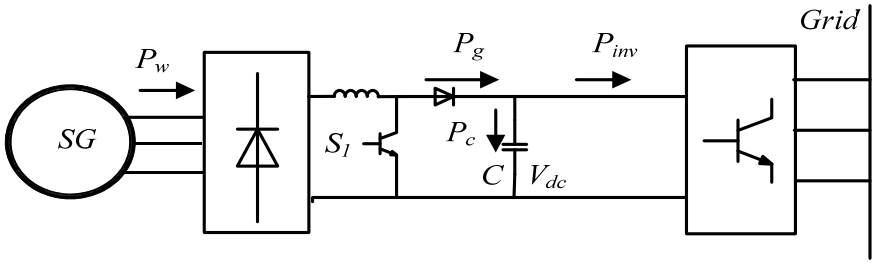

(b) Power flow under voltage faults condition

Figure 66: Power flow through DC link.

Figures 67 (a) and (b) show the voltages of the DC capacitor bus when the grid voltage drops from 1 p.u. to 0.8 p.u. and to 0.1 p.u., respectively. Under the 0.8 p.u. fault condition, the DC capacitor voltage increases to about 640V and decreases to about 540V after the grid voltage recovers. In this situation, the DC capacitor voltage is still in the normal voltage range and will not damage the capacitor. On the other hand, under the 0.1 p.u. fault condition, the DC capacitor voltage increases to about 1300V which will definitely damage the capacitor and converter. Thus, an additional control protection scheme should be adopted to solve this problem.

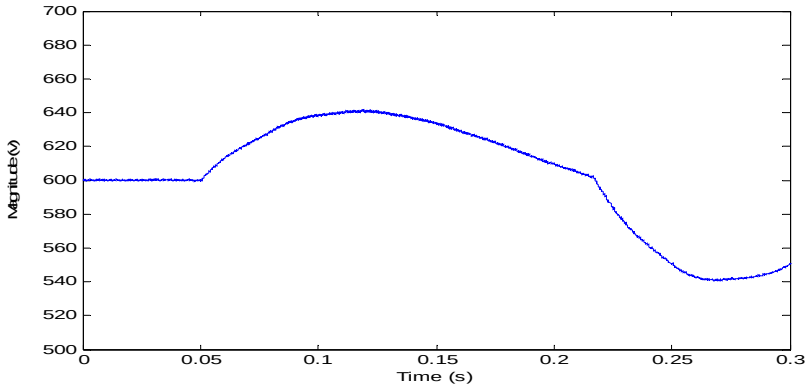

(a) DC voltage when grid voltage drops to 0.8 p.u.

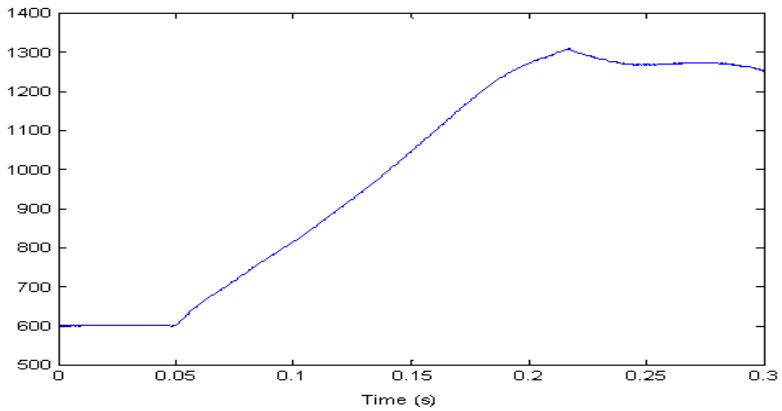

(b) DC voltage when grid voltage drops to 0.1 p.u.

Figure 67: DC capacitor voltage waveforms during grid voltage faults.

There are many solutions to limit the voltage of the DC capacitor link, the easiest and most effective way is to add a braking resistor in parallel with the DC capacitor to dissipate the extra energy flowing into the capacitor. Fig. 68 shows the braking resistor diagram. The difference between DC voltage and reference DC voltage pass through a PI regulator and produce the gate signal *d* to control the on and off state of the braking resistor switch. However only using the DC voltage to regulate the switch is difficult to coordinate with the inverter-side voltage control loop, resulting in a long response time.

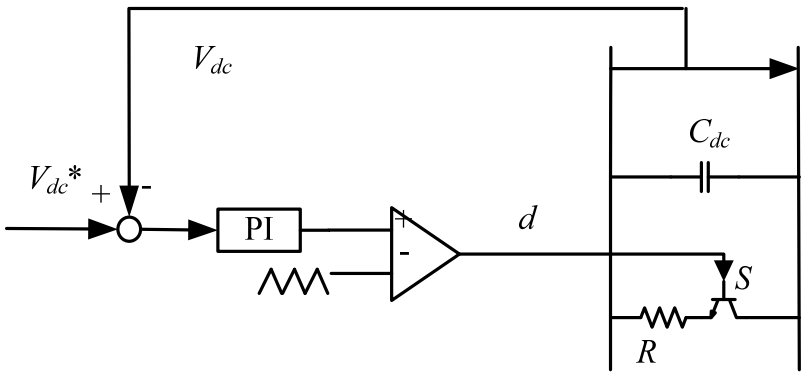

Figure 68: Braking resistor diagram.

Fig. 69 shows an improved braking resistor control diagram. After calculation, the power difference between P_g and P_{out} is used to decide if it is necessary to discharge energy. There is no need to use braking resistor if ΔP is not large; under normal grid voltage condition, there is still power variation. When ΔP is too large, the grid-side inverter cannot control the DC capacitor voltage, and the braking resistor should be turned on in the system. ΔP will pass through a PI regulator to produce the gate signal, and the extra energy will be dissipated on the braking resistor. If ΔP decreases to a reasonable range, the braking resistor will be turned off.

Using the braking resistor can effectively reduce the voltage of the DC capacitor, while the temperature of the resistor will also increase significantly if the voltage fault last long. This will cause other problems. Another method is to add an energy storage system but it will increase the cost of the whole system. From equation $P_g = P_c + P_{inv}$, if P_c should be limited as small as zero, when P_{inv} decreases, P_g should also decrease to keep P_c unchanged. Reducing P_g means reduce the power extracted from the wind. One practical way is to reduce the value of the power coefficient C_p. Increasing the pitch angel can reduce C_p, but the response time is too long to meet the requirement. Another way is to increase the tip speed ratio λ which can be achieved by increasing the wind turbine speed. The extra energy will be stored in the large inertia of the wind turbine. Thus, increasing the wind turbine speed can reduce the voltage of the DC capacitor bus to protect the system. As shown below, if the inertia and the difference in the wind turbine speed are large, the kinetic energy is also large:

$$\Delta P_m = \frac{1}{2} J(\omega_1^2 - \omega_2^2) \tag{40}$$

where J is the wind turbine inertia and ω_1, ω_2 are the wind turbine speed.

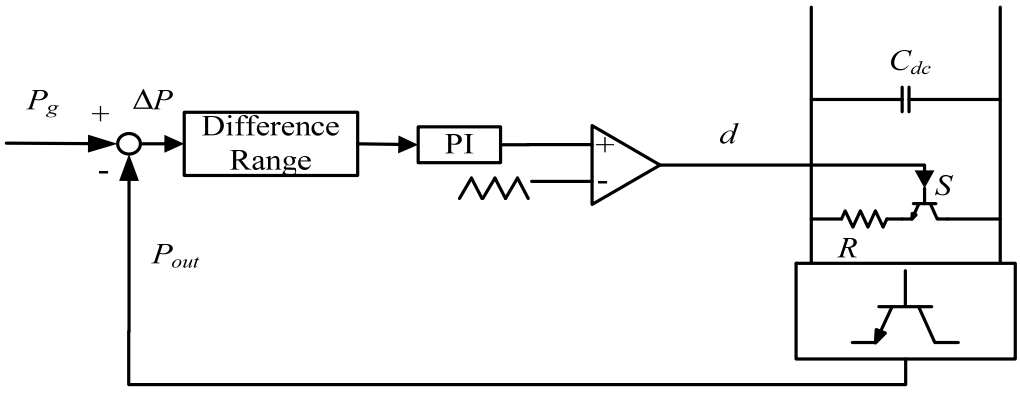

Figure 69: Braking resistor control diagram.

The relationship of mechanical torque T_m, electrical torque T_e and the rotor speed ω is given by (41). If the electrical torque decreases, while the mechanical torque does not change, the rotor speed will increase. After rotor speed increases, the mechanical torque will decrease until it equals to the electrical torque, and the rotor speed will not increase anymore.

$$T_m - T_e = J\frac{d\omega}{dt} \tag{41}$$

The speed control scheme is same as Figure 13. The current loop reference value will be reduced during the grid voltage faults, and the electrical torque will decrease. The rotor speed will increase to reduce the power extracted from the wind. Fig. 70 shows the speed control scheme. V_{gnorm} is the grid voltage under normal condition (usually 1 p.u.), and V_g is the actual grid voltage. During a voltage fault, the grid voltage will drop to a lower value. As it is discussed before, if the voltage drop is not very large, for example, 0.8 p.u., the outer voltage loop of the grid side inverter can regulate the DC capacitor voltage, and there is no need to increase the rotor speed of the wind turbine. If the voltage drops from 1 p.u. to 0.1 p.u., the speed regulator will increase the rotor speed of the wind turbine to reduce the power extracted from the wind. Fig. 71 shows the DC capacitor bus voltage during the voltage drop to 0.1 p.u. When the voltage fault starts at 0.5 second, the DC capacitor voltage increases to about 650V and then decreases to 550V. Another peak happens at 10 cycles after the fault is cleared. The magnitude is about 700V. From the figure we can see that the DC capacitor voltage changes in a small range and a good protection is provided to the capacitor.

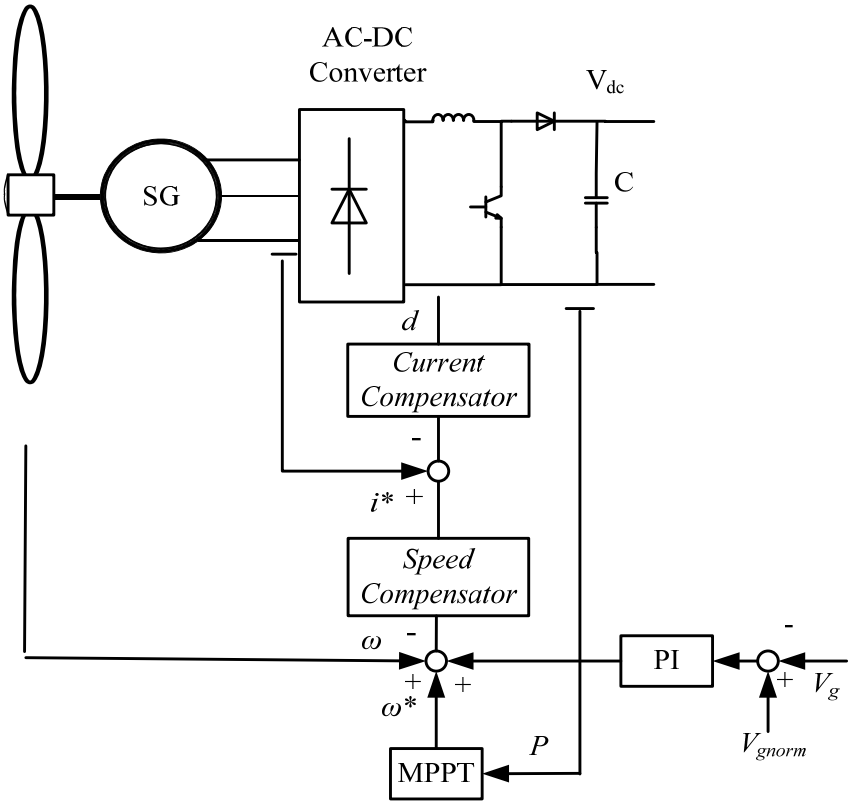

Figure 70: Speed control scheme.

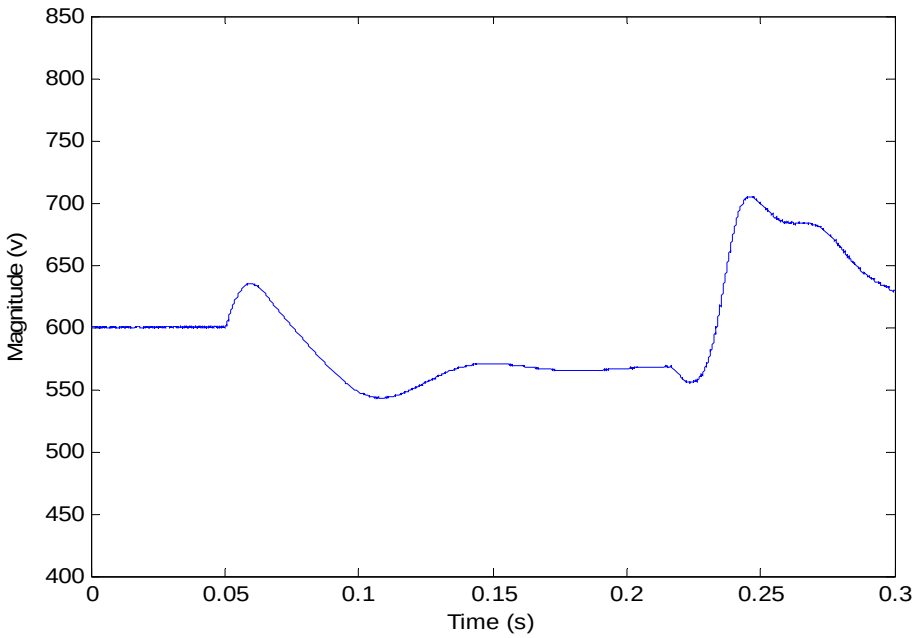

Figure 71: Waveform of DC capacitor voltage.

This chapter showed the simulation results under the normal grid condition (no grid faults occurred). With different wind speed inputs, the wind power system adjusted the rotor speed to extract the maximum power. The inverter-side controller kept the DC capacitor link voltage at 600V to transfer the generator-side power to the grid.

CHAPTER FIVE

Conclusion

This thesis presents the design, modeling and analysis of a wind power generation system (WPGS). Since the wind speed is intermittent and based on the power-wind speed curve, a maximum power tracking algorithm is adopted to control the generator-side diode rectifier and DC/DC boost converter to track the maximum power points. In order to minimize the total harmonics distortion of the current when the grid-side inverter is connected to the grid, an LCL filter is modeled and analyzed to interface with the grid. The detailed LCL filter design optimization is introduced. Because of the instability of the LCL filter, a new two-current loop control scheme is developed. Eliminating the damping resistor of the LCL filter which is used in conventional filter design, a sensor is added to limit the capacitor current. This active damping method reduces the power loss of the damping resistor to improve the overall power efficiency. Because of the drawbacks of proportional integral (PI) controller, a proportional plus resonance (PR) controller is used for the inner current loop. The system achieves zero steady-state error in the stationary coordinate frame, which is simpler and more accurate. Moreover, the inner current loop has a bigger bandwidth of 1,290Hz, which has faster dynamic response than the outer voltage loop with a bandwidth of 441Hz. With the different bandwidths, the inner current loop and outer voltage loop can be designed separately. Analysis of the stability when the grid impedance is changing shows that the inner current loop provides a good phase margin from about 48.7 degree to 70.1 degree which indicates a stable

control loop. Outer voltage loop is designed with a smaller bandwidth and a 44.4 degree phase margin to provide turbulence rejection ability.

The grid voltage is not stable and a transient analysis of the wind power system is performed. The system is simulated under different grid voltage faults conditions. The simulation results clearly show how the system reacts during the faults. If the voltage faults last long and the voltage drop is large, the outer voltage loop will no longer keep the DC capacitor bus voltage stable which will damage the capacitor and converter with a high voltage. Thus, a basic low-voltage ride-through control scheme is discussed. The simulation results show that WPGS tracks the maximum power from the wind and provides a stable control scheme. When a voltage faults occur, the DC capacitor bus voltage control limited the DC capacitor voltage into a small range to protect the capacitor.

APPENDICES

APPENDIX A

Simulation Model

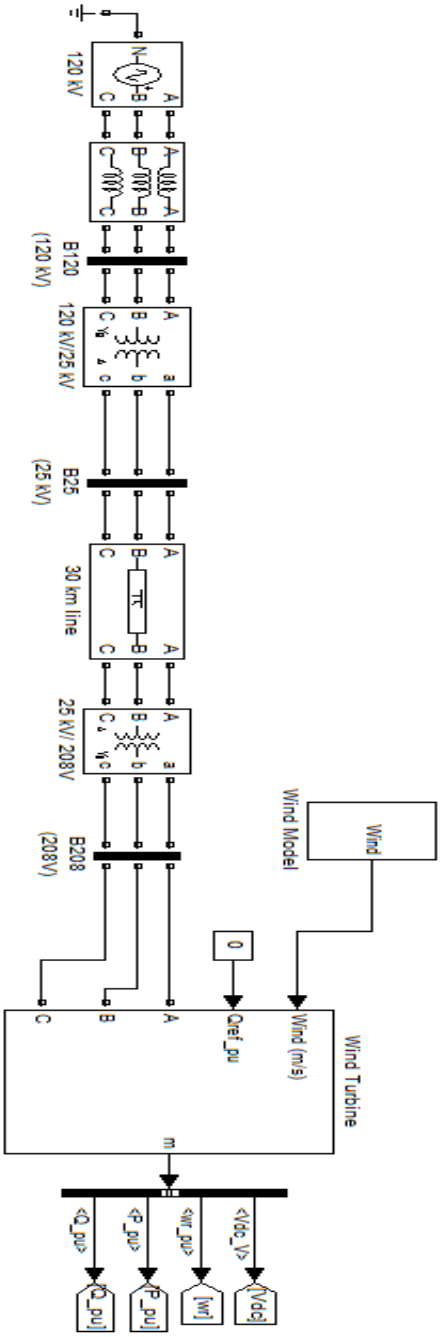

A.1: Transmission line and wind power system.

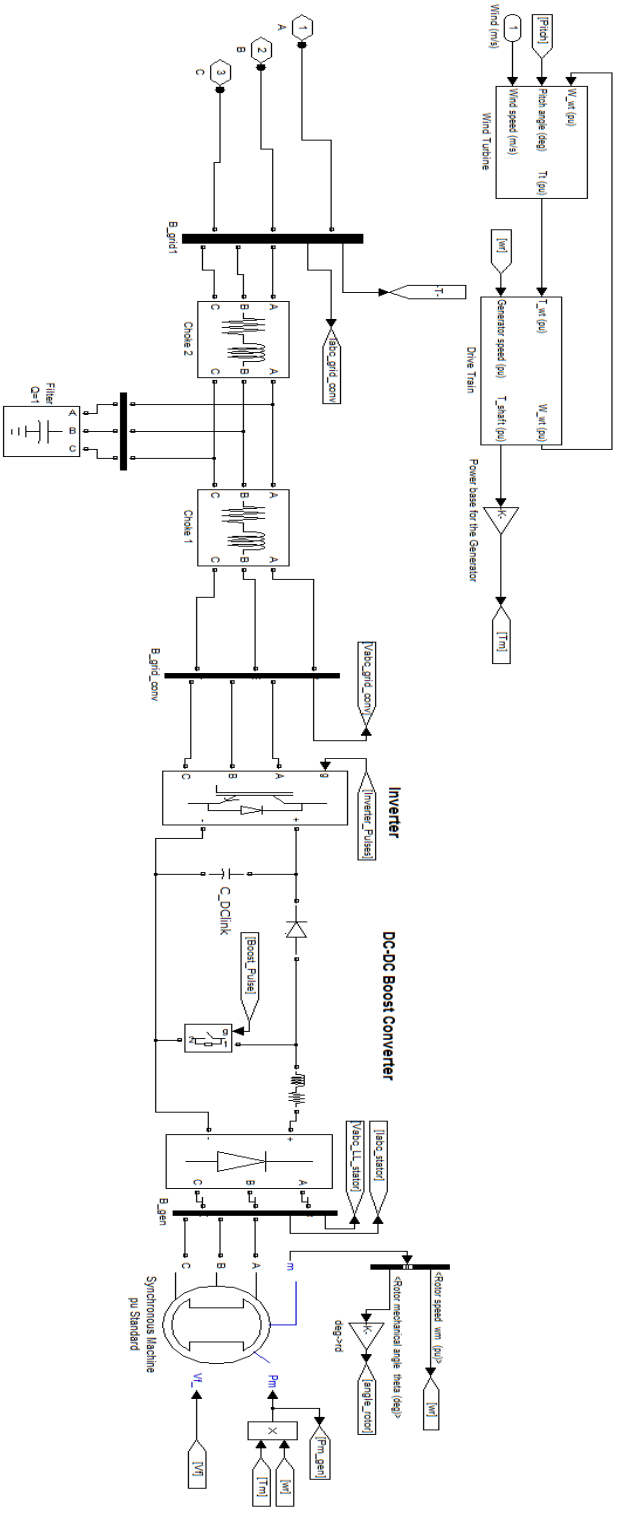

A.2: Wind Power System.

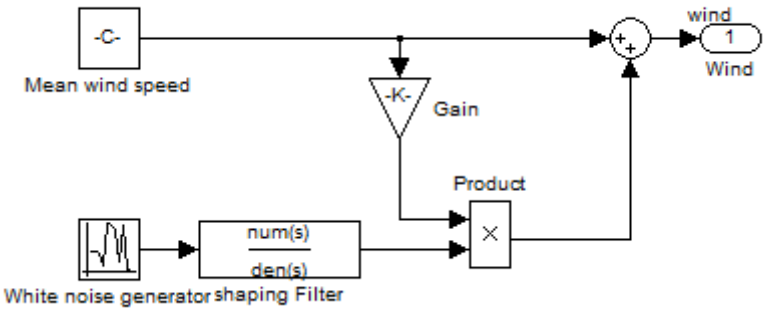

A.3: Wind Model

APPENDIX B

abc-αβ Transformation and *abc-dq* Transformation

(1) Transformation of three-phase *abc* to two-phase *αβ*

B.1 is the space vector of three-phase *abc* and two-phase *αβ*.

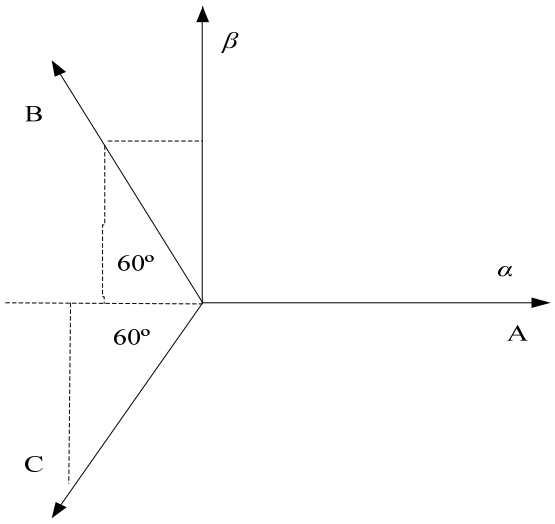

B.1: Space vector of *abc* and *αβ* in stationary coordinate.

From B.1, the transformation equation can be obtained as following:

$$\begin{bmatrix} i_\alpha \\ i_\beta \end{bmatrix} = \sqrt{\frac{2}{3}} \begin{bmatrix} 1 & -1/2 & -1/2 \\ 0 & \sqrt{3}/2 & -\sqrt{3}/2 \end{bmatrix} \begin{bmatrix} i_a \\ i_b \\ i_c \end{bmatrix} \quad (1)$$

where i_α, i_β are the currents in stationary *αβ*-coordinate, i_a, i_b, i_c are the currents in stationary *abc*-coordinate.

(2) Transformation of two phase *αβ* to two-phase *dq*

B.2 is the space vector of two-phase *αβ* and two-phase *dq*

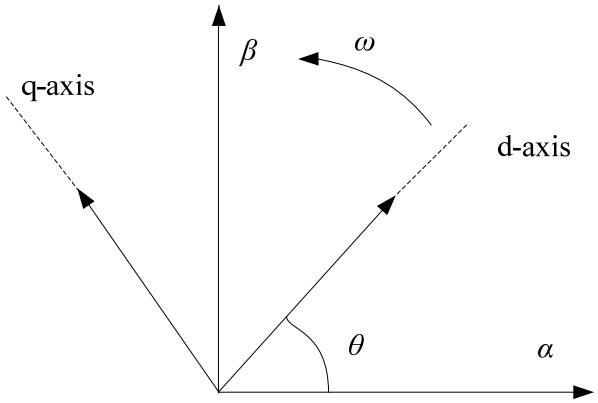

B.2: space vector of two-phase *αβ* in stationary coordinate and two-phase *dq* in synchronous coordinate.

From B.2, the transformation equation can be obtained as following:

$$\begin{bmatrix} i_d \\ i_q \end{bmatrix} = \begin{bmatrix} \cos\theta & \sin\theta \\ -\sin\theta & \cos\theta \end{bmatrix} \begin{bmatrix} i_\alpha \\ i_\beta \end{bmatrix} \tag{2}$$

where i_d, i_q are the currents in synchronous coordinate, i_α, i_β are the currents in stationary coordinate, θ is the angel between α axis and d axis.

(3) Transformation of three-phase *abc* to two-phase *dq*

From the transformation matrix of *abc*-coordinate to *αβ*-coordinate and *αβ*-coordinate to *dq*-coordinate, the transformation equation of three-phase *abc* to two-phase *dq*-coordinate can be obtained as following:

$$\begin{bmatrix} i_d \\ i_q \end{bmatrix} = \sqrt{\frac{2}{3}} \begin{bmatrix} \cos\theta & \cos(\theta - 2\pi/3) & \cos(\theta + 2\pi/3) \\ \sin\theta & \sin(\theta - 2\pi/3) & \sin(\theta + 2\pi/3) \end{bmatrix} \begin{bmatrix} i_a \\ i_b \\ i_c \end{bmatrix} \tag{3}$$

BIBLIOGRAPHY

[1] A. Murdoch, R. S. Barton, J. R. Winkelman, and S. H. Javid, "Control Design and Performance Analysis of a 6 MW wind Turbine Generator," *IEEE Transactions on Power Apparatus and Systems,* vol. 102, no. 5, pp.1340-1347, May 1983.

[2] E. S. Kim, B. M. Song, and K. Y. Lee, "Modeling and Analysis of a Grid-Connected Wind Energy Conversion System Using PSCAD/EMTDC," *IEEE 2010 PES Conference on Innovation Smart Grid Technologies*, Jan. 19-21, 2010.

[3] G. H. Kim, Y. J. Kim, M. Park, I. K. Yu, and B. M. Song, "RTDS-based Real Time Simulations of Grid-Connected Wind Turbine Generator Systems," *IEEE 2010 Applied* Power *Electronics Conference (APEC),* Feb. 22-25, 2010, pp. 2085 -2090.

[4] A. Roshan, R. Burgos, A. C. Baisden, F. Wang and D. Boroyevich, "A D-Q frame controller for a full-bridge single phase inverter used in small distributed power generation systems," in *Proc. of IEEE APEC*, Anaheim CA, Feb. 2007, pp.641-647.

[5] R.-Y. Kim, S.-Y. Choi, and I.-Y. Suh, "Instantaneous control of average power for grid tie inverter using single phase D-Q rotating frame with all pass filter," in *Proc. of IEEE IECON*, Busan, Korea, Nov. 2004, pp. 274-279.

[6] Z. Chen and E. Spooner, "Grid Power Quality with Variable Speed Wind Turbines," *IEEE Transaction Energy Conversion,* vol. 16, no. 2, pp. 148-154, June 2001.

[7] C. D. Schauder and S. A. Moran, *Multiple reference frame controller for active power filters and power line conditioners*, U.S. Patent 5309353, May 1994

[8] Z. Chen, J. M. Guerrero, and F. Blaabjerg, "A Review of the State of the Art of Power Electronics for Wind Turbines," *IEEE Transactions on Power Electronics,* vol. 24, no. 8, pp. 1859-1875, Aug. 2009.

[9] P. Zhou and Y. K. He, "Control Strategy of an active Crowbar for DFIG Based Wind Turbine under Grid Voltage Dips," *Proceeding of International Conference on Electrical Machines and Systems 2007*, Oct. 8-11, Seoul, Korea.

[10] Y. Chen and X. Jin. Modeling and control of three-phase voltage source PWM rectifier [C]. *CES/IEEE 5th International Power Electronics and Motion Control Conference,* 2006, 3:1459-1462.

[11] S. Heier, "*Grid integration of wind energy conversion systems",*[M].UK: John Wiley and sons Ltd, 1998.

[12] F. Blaabjerg and F. Iov, "Wind power - a power source now enabled by power electronics," 30 September - 4 October 2007, Keynote paper in *Proc of 9th Brazilian*.

[13] *Power Electronics Conference COBEP 07*, Blumenau Santa Catarina, Brazil, ISBN 978-85-99195-02-4.

[14] F. Blaabjerg, F. Iov, Z. Chen, and R. Teodorescu, "Power electronics in renewable energy systems," Keynote paper at *EPE-PEMC 2006 Conference*, August 30 - September 1 2006, Portoroz , Slovenia, p.17, IEEE Catalog Number: 06EX1405C, ISBN 1-4244-0449-5.

[15] F. Blaabjerg, R. Teodorescu, M. Liserre, and A. Timbus, "Overview of control and grid synchronization for distributed power generation systems," *IEEE Transactions on Industrial Electronics,* vol. 53, no. 5, pp. 1398-1409, Oct. *2006.*

[16] J. G. Slootweg, H. Polinder, and W. L. Kling, "Dynamic modelling of a wind turbine with doubly fed induction generator," *IEEE Transactions on Power Electronics,*vol. 18, no. 2, pp. 644, May 2003.

[17] F. Hansen, L. Helle, F. Blaabjerg, E. Ritche, S. Munk-Nielsen, H. Bindner, P. Sørensen, and B. Bak-Jensen, *Conceptual survey of Generators and Power Electronics for Wind Turbines.* RISØ National laboratory, December 2001.

[18] F. Blaabjerg and F. Iov, "Wind power - a power source now enabled by power electronics," 30 September - 4 October 2007. Keynote paper in *Proc of 9th Brazilian Power Electronics Conference COBEP 07*, Blumenau Santa Catarina, Brazil, ISBN 978-85-99195-02-4.

[19] A. V. Timbus, R. Teodorescu and F. Blaabjerg, "Independent Synchronization and Control of Three Phase Grid Converters," *SPEEDAM 2006 International* Symposium *on* Power *Electronics, Electrical Drives, Automation and Motion*.

[20] M. P. Kazmierkowski, R. Krishnan, and F. Blaabjerg, *Control in Power Electronics*. Academic Press, 2002. ISBN 0-12-402772-5.

[21] M. Liserre, A. Dell'Aquila and F. Blaabjerg, "Genetic Algorithm-Based Design of the Active Damping for an LCL-Filter Three-Phase Active Rectifier," *IEEE Transactions on Power Electronics,* vol. 19, no 1, pp. 76-86, Jan. 2004.

[22] M. Liserre, A. Dell'Aquila, and F. Blaabjerg, "Design and Control of an LCL-filter based Three-phase Active Rectifier," *Industry Applications Conference*, 2002. 37th IAS Annual Meeting, vol. 2, pp. 1181-1188, Oct. 2002.

[23] O. Anaya-Lara, N. Jenkins, J. Ekanayake, P. Cartwrite, and M. Hughes. *Wind energy* generation*: modelling and control*, john wiley: West Sussex, UK, 2009.

[24] N. Mohan, T. M. Undeland, and W. P. Robbins: *Power electronics: converter, drives and applications,* Wiley, 2002, 3rd edu.

[25] S. Song, S. Kim, and N. Hahm, "Implementation and control of grid connected AC-DC- AC power converter for variable speed wind energy conversion system," *18th Annual IEEE Applied Power Electronics Conference and Exposition*, vol. 1, pp. 154-158, May 2003.

[26] S. Hao, G. Hunter, V. Ramsden, and D, Patterson, "Control system design for a 20 kW wind turbine generator with a boost converter and battery bank load," *Power Electronics Specialists Conference, 2001. PESC. 2001 IEEE 32nd Annual,* vol.4, pp. 2203, Jun 2001.

[27] S. Wall and R. Jackson, "Fast controller design for practical power-factor correction systems," *Industrial Electronics, Control, and Instrumentation, 1993. Proceedings of the* IECON *'93, International Conference on*, pp. 1027, Nov 1993.

[28] C. W. Yang, H. Liang, and J. C. Jiang, "Modeling and simulation of AC-DC-AC converter system for MW-level direct-drive wind turbine grid interface," *IEEE Power Electronics Specialists Conference*, pp. 1-4, June 2006.

[29] F. D. Bianchi, H. D. Battista, and R. J. Mantz, *Wind Turbine Control System*. Springer, 2007. ISBN 1-8462-8492-9.

[30] X. Xiong and H. Liang, "Research on multiple boost converter based on MW-level wind energy conversion system," *Proceeding of the 8th International Conference on Electrical Machines and Systems*, pp.1046-1049, Feb. 2005.

[31] R. Datta and V. T. Ranganathan, "A method of tracking the peak power points for a variable speed wind energy conversion system," *IEEE Transactions on Energy Conversion*, vol. 18, no.1, pp. 163-168, Jan. 2003.

[32] N. Mohan, *Advanced electric drives*. MNPERE, 2001. ISBN -9715-2920-5.

[33] M. Liserre, A. Dell'Aquila, and F. Blaabjerg, "Design and control of a three-phase active rectifier under non-ideal operating conditions," *IEEE Transactions on Power Electronics*, pp.1181 – 1188, 2002.

[34] M. Liserre, F. Blaabjerg, and R. Teodorescu, "Grid impedance estimation via excitation of LCL-filter resonance*" IEEE Transactions on Industry Applications* vol 43, no 5, pp. 1401-1407, Sept/Oct. 2007.

[35] M. Adil. Al-Zamil, and D. A. Torrey, "A passive Series, Active Shunt filter for High Power Applications," *IEEE Transactions On Power Electronics*, Vol 16, No.1, January 2001.

[36] C. D. Schauder and S. A. Moran, *Multiple reference frame controller for active power filters and power line conditioners*, U.S. Patent 5309353, May 1994.

[37] X. Yuan, W. Merk, H. Stemmler, and J. Allmeling, "Stationary-Frame Generalized Integrators for Current Control of Active Power Filters with Zero Steady-State Error for Current Harmonics of Concern Uder Unbalanced and Distorted Operating Conditions," *IEEE Trans. On Ind. App*., vol. 38, no.2, pp. 523-532, Mar./Apr. 2002.

[38] N. Z. Daniel and D. G. Holmes, "Stationary Frame Current Regulation of PWM Inverters With Zero Steady-State Error," *IEEE Transactions on Power Electronics*, vol.18, no.3, pp. 1185-1190, May 2003.

[39] E. Twining and D. G. Holmes, "Grid current regulation of a three-phase voltage source inverter with an LCL input filter," *IEEE Trans. Power Electron*., vol.18, no. 3, pp. 888-895, May 2003.

[40] G. Yaleinkaya, M. H. J. Bollen, and P. A. Crossley, "Characterization of voltage sags in industrial distribution systems," *IEEE Transactions on Industry Applications*, vol. 34, no. 4, pp. 682, August 2002.

[41] J. F. Conroy and R. Watson, "Low-voltage ride-through of a full converter wind turbine with permanent generator," *IET Renew. Power Gener*, vol. 1, no. 3, pp 182-189, Sep. 2007.

[42] *Interconnection for wind energy (order no. 661 final rule, docket no. rm05-4-000),* Federal Energy Regulatory Commission (FERC), Tech. Rep., June, 2nd 2005.

[43] *On the Low Voltage Ride-Through (LVRT) provisions of the Order No. 661. Final Rule (joint report by the north american electric reliability council (nerc) and the* american *wind energy association (awea), docket no. rm05-4-000),* Federal Energy Regulatory Commission (FERC), Tech. Rep., September, 19th 2005.